Gain Studies of Dilute Nitride Semiconductor Materials

David J. Palmer

Ph.D. Thesis

School of Physics and Astronomy
Cardiff University

September 2006

UMI Number: U584895

All rights reserved

INFORMATION TO ALL USERS
The quality of this reproduction is dependent upon the quality of the copy submitted.

In the unlikely event that the author did not send a complete manuscript
and there are missing pages, these will be noted. Also, if material had to be removed,
a note will indicate the deletion.

UMI U584895
Published by ProQuest LLC 2013. Copyright in the Dissertation held by the Author.
Microform Edition © ProQuest LLC.
All rights reserved. This work is protected against
unauthorized copying under Title 17, United States Code.

ProQuest LLC
789 East Eisenhower Parkway
P.O. Box 1346
Ann Arbor, MI 48106-1346

Abstract

Due to the increased use of optical fibre communications, there is much interest in semiconductor lasers operating between 1.3 and 1.6μm and grown on GaAs substrates. One approach used to achieve this is the dilute nitride material, InGaAsN.

In this work, the segmented contact method was used to study dilute nitride quantum well laser active regions designed to operate around 1.3μm. The net modal absorption, net modal gain and spontaneous emission rate spectra were measured for samples with quantum well nitrogen contents of 0%, 0.5% and 0.8% and GaAs barriers. A sample with 0.5% quantum well nitrogen content but larger bandgap GaAsP barriers was also examined. By defining and measuring the inversion factor, the spontaneous emission rate spectra were calibrated and the overall internal efficiencies of the samples calculated.

The modal absorption and gain data provide the first experimental evidence for the matrix element reducing as nitrogen content increases. The measured maximum absorption predicts a matrix element relative to a nitrogen free quantum well of 0.58 and 0.67 for 0.5% and 0.8% nitrogen respectively. The measured overall internal efficiency was found to decrease dramatically with increasing nitrogen content, falling from approximately 15% to 5% between 0% and 0.8% nitrogen when measured at 300K.

Comparisons between samples with different quantum well barrier heights showed an increase in the measured maximum absorption of a factor 1.28 and an increase in the overall internal efficiency of approximately a factor 1.15 when the barrier height was increased. No barrier emission was observed in the spontaneous emission rate spectra measured from the top of these samples. However, the calculated occupation of the GaAsP barrier sample was less than 3% of the sample with GaAs barriers, suggesting that a reduction in leakage current could explain the improved efficiency.

Acknowledgments

To begin, I would like to thank my supervisors P. Blood and P. Smowton for their advice, support and guidance throughout my PhD studies. Thanks also to everyone in the optoelectronics group who have always been willing to help with problems and made my time at Cardiff enjoyable, particularly Iain, Helen, Lois and Gareth. Also at the School of Physics and Astronomy, I thank S. Baker for tirelessly supplying me with nitrogen, R. Tucker for his help and advice with all things electrical, J. Trivett and particularly G. Summers in the workshop for always being able to make what I wanted when I needed it. Finally, I thank my parents, my sister Siân, my wider family, and especially Lisa for their support throughout my studies and for keeping me generally sane with advice and consistently enjoyable times.

Contents

Chapter 1 Introduction **1**

1.1 Introduction to thesis and summary of work undertaken 1
1.2 Thesis Structure 2
1.3 References 2

Chapter 2 Background to Lasers and Dilute Nitride Material System **3**

2.1 Introduction 3
2.2 Background to Diode lasers 3
2.2.1 Principles of lasers 3
2.2.2 Dimensionality of active regions in diode lasers. 5
2.3 Theory of QW semiconductor lasers 7
2.3.1 Energy Bands and Effective Mass 7
2.3.2 Density of States for a Quantum Well 10
2.3.3 Occupation of States 13
2.3.4 Transitions between Bands 14
2.3.5 Matrix element and Transition rates. 15
2.3.6 Equation for Modal Gain 17
2.3.7 Equation for spontaneous emission 19
2.3.8 Non radiative and leakage processes 20
2.4 Dilute Nitride semiconductor material for emission at 1.3μm 21
2.4.1 Importance of emission at 1.3μm 21
2.4.2 Current material systems for 1.3μm emission 22
2.4.3 InGaAsN 23
2.5 References 27

Chapter 3 Experimental Method **29**

3.1 Introduction 29
3.2 Techniques available to study laser structures. 29
3.3 The Segmented Contact Method 30
3.3.1 Device Structure and Amplified Spontaneous Emission 30

3.3.2 Net Modal Gain and Spontaneous Emission 32
3.3.3 Net Modal Absorption 35
3.3.4 Calibration of the Spontaneous Emission and the Internal Quantum Efficiency. 36
3.4 Equipment Used for Segmented Contact method Experiments 39
3.5 Improvements Made to the Experimental Setup. 44
3.6 Confirmation that equipment is operating as required 51
3.7 Estimating errors in the experimental measurements 55
3.8 References 58
Chapter 4 The Effect of Nitrogen in the InGaAsN QW 59
4.1 Introduction 59
4.2 Details of Structures Measured 59
4.3 Requirements for a sample suitable for multisection measurements 61
4.4 Polarisation of emission in highly strained samples. 64
4.5 Effect of Nitrogen on Modal Absorption Spectra 65
4.5.1 Interpretation of Modal Absorption Results 69
4.5.2 Effect of Nitrogen on Modal Gain and Spontaneous Emission Spectra 72
4.5.3 Calibration of the Spontaneous Emission 75
4.5.4 Comparison of Samples at Different Temperatures 76
4.5.5 Comparison with alternative measurement techniques. 83
4.6 Summary. 84
4.7 References 85
Chapter 5 Effect of Barrier material on InGaAsN Quantum Well 87
5.1 Introduction 87
5.2 Samples studied in this work 87
5.3 Requirements of a Sample for Multisection Measurements. 89
5.4 Effect Of barrier height on modal absorption spectra 91
5.5 Interpretation of Absorption spectra 94
5.5.1 Predicted change in transition energy 94
5.5.2 Analysis of observed change in maximum absorption 98

5.6 Effect of Barrier Height on Modal Gain and Spontaneous Emission Spectra 100
5.7 Occupation of Barrier Layers 109
5.8 Spontaneous Emission collected from the top of samples 112
5.9 Summary 116
5.10 References 117
Chapter 6 Summary of Achievements and Future Work 119
6.1 Achievements 119
6.1.1 Effect of nitrogen 119
6.1.2 Effect of barriers 120
6.2 Conclusion 121
6.3 Future Work 122

Chapter 1 Introduction

1.1 Introduction to thesis and summary of work undertaken.

The work in this thesis examines the modal gain, modal absorption and spontaneous emission rate spectra of InGaAsN quantum well laser structures. To investigate the properties of the material, samples with different nitrogen concentration in the quantum well are compared. The effect of the bandgap of the barrier material is also investigated by the use of either GaAs or GaAsP barriers.

The InGaAsN material system has been proposed [1.1] as being suitable for laser devices emitting in the important telecoms windows of 1.3μm and 1.55μm. There is large interest in new material systems for emission at these wavelengths that can be grown on GaAs substrates. These include InGaAsN quantum wells and also InAs quantum dots. This interest is sparked by the need for devices capable of operation at elevated temperatures without requiring expensive cooling systems. The current InP based laser diodes do not fully achieve these requirements, because of the presence of high thermal leakage currents in these devices. InGaAsN promises growth on GaAs with high electron confinement and is therefore one of the most promising candidates for realising devices emitting at 1.3μm and operating efficiently at elevated temperatures.

This thesis aims to add to the knowledge of the optical properties of InGaAsN via experimental measurements and interpretation of these measurements. In total four different InGaAsN laser structures were studied. In three of the samples, the nitrogen concentration in the quantum well is different, being 0%, 0.5% or 0.8%. The fourth sample has a nitrogen content of 0.5% but the barrier material is GaAsP instead of GaAs. This increases the barrier height and therefore the confinement of carriers to the well. The measurement technique used is the segmented contact method. Using this technique, the modal absorption, modal gain and spontaneous emission rate spectra are measured for each sample at temperatures of 200, 250

and 300K. It is found that increasing nitrogen content decreases the maximum absorption by a factor 1.55 between 0% and 0.8%. The current density required for fixed gain increases with increasing nitrogen content by up to a factor 4. Using a wider bandgap barrier material increases the maximum absorption and reduces the current density required for fixed gain. By calibrating the spontaneous emission rate, the radiative current density and overall quantum efficiency are determined. The gain vs radiative current density relation is found to vary very little with nitrogen content or utilising different barrier material. The overall quantum efficiency is greatly reduced when nitrogen is added to the quantum well from 13-15% at 0% nitrogen to less than 5% with 0.8% nitrogen for data measured at 300K.

1.2 Thesis Structure

This thesis is split into three main sections. In chapter two, the background to semiconductor lasers and the dilute nitride material system is presented. In chapter three the details of the experimental methods used in this work are described. This chapter also describes the improvements made to an existing equipment system during this work. The results of the measurements are presented in chapters four and five. Chapter four presents results and discussion of the samples with different nitrogen content. Chapter five examines the effect of the barrier material on the optical properties of InGaAsN. Finally, chapter six provides conclusions and a summary of the achievements reached during this work. This chapter also includes discussion of any future work which would add to the insight gained from this thesis.

1.3 References

1.1 M. Kondow, T. Kitani, S. Nakatsuka, M. C. Larson, K. Nakahara, Y. Yazawa, M. Okai, *IEEE J. Sel Top Quantum Electron*, **3** (1997) 719

Chapter 2 Background to Lasers and Dilute Nitride Material System

2.1 Introduction

In this chapter the background of semiconductor lasers is discussed. This includes discussion of quantum well active regions for lasers, band structure and the derivation of equations governing gain and spontaneous emission in semiconductor lasers. The motivations behind this thesis are also discussed. An explanation of the reasons for interest in dilute nitride active regions is presented. This includes the limitations of current devices, as well as details of how InGaAsN could reduce these limitations.

2.2 Background to Diode lasers

In this section, the basic principles of a laser and the conditions under which laser action occurs are described. For the specific case of diode lasers the properties of the material are discussed, including different structures that can be used to create a diode laser and the band structure of semiconductors. The possible transitions between these bands are outlined. Finally the equations governing recombination, optical gain and spontaneous emission are derived. The discussions and derivations follow those used in [2.1,2.2,2.3].

2.2.1 Principles of lasers

A laser is a light source that has the property of a dominance of coherent emission. To make this situation possible, a laser is composed of a material capable of providing optical gain, sandwiched between two mirrors. As the optical field oscillates back and forth through the laser cavity, it experiences amplification due to the gain provided by the media between the mirrors. Laser action occurs when the gain experienced by the optical field matches the losses present in the laser

structure. The gain needed to reach this condition is the threshold gain (G_{th}) and is given by:

$$G_{th} = \alpha_i + \frac{1}{L}\ln\left(\frac{1}{R}\right)$$

Equation 2.1

The optical field experiences a loss due to scattering from imperfections in the optical cavity, given by α_i in the equation above and measured in units of reciprocal centimetres. There is an additional loss, due to light lost through transmission in the mirrors. This loss is calculated from the reflectivity of the mirrors, R, and converted to units of reciprocal length as shown in Equation 2.1. The loss of light through the mirrors is unavoidable, as without it no light would be emitted by the laser. However, limiting the emission from one or both mirrors is a useful way of reducing the gain needed to achieve laser action.

In a diode laser, semiconductor material provides the gain medium, in the simplest case, the mirrors are provided by the semiconductor - air interface produced by cleaved facets. In order to provide optical gain, the semiconductor material must be forced into a non-equilibrium state. This provides an excess of electrons in high energy states and an excess of holes in low energy states. This situation is known as population inversion and is the condition when the probability of an electron occupying a high energy state is higher than the probability of an electron occupying a low energy state. The details of this will be discussed in the next section. Light emission occurs under these conditions when an electron in a high energy state recombines with a hole in a low energy state, producing a photon with energy equal to the energy difference between the states. The non equilibrium condition of population inversion can be achieved by optical excitation or electrical injection. Devices operating with direct electrical injection will be studied in this thesis. An example of a laser chip designed for electrical injection is shown in Figure 2.1.

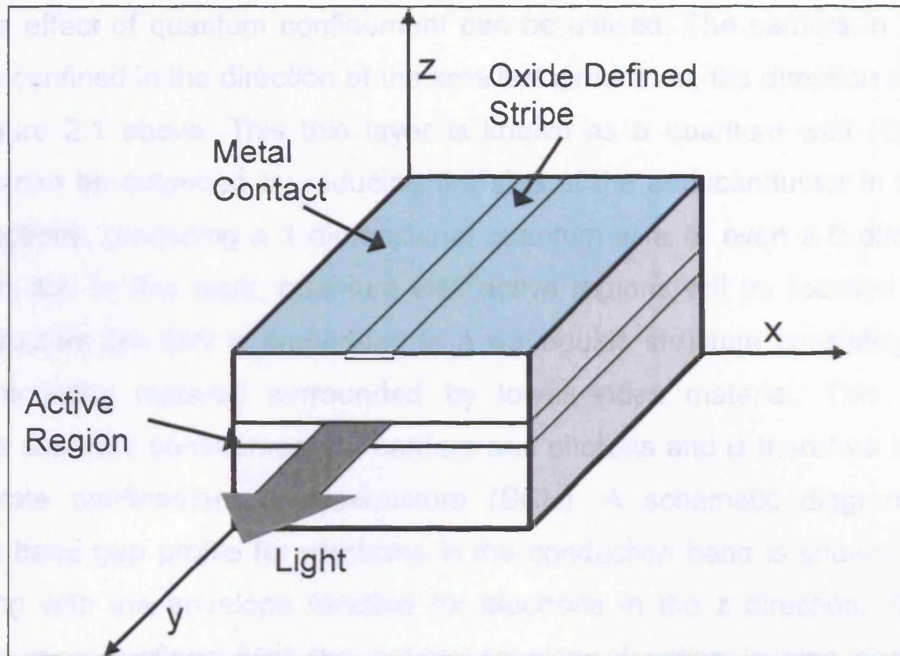

Figure 2.1 Schematic diagram of laser chip displaying the directions as used in this thesis.

In the above figure, the upper and lower surfaces of the chip have metal contacts to enable electrical injection. Current is confined in the x direction by the presence of a stripe defined by regions of oxide before the upper contact is applied. The central layers of the device are the active region of the laser and this is where the light is generated. In the above structure light is emitted in the y direction. The direction of growth of the sample is in the z direction.

2.2.2 Dimensionality of active regions in diode lasers.

The electrical injection of carriers into the active region is achieved by placing the active region between n and p doped semiconductor layers with a larger bandgap than the active region. This is known as a double heterostructure (DH). Electrons and holes are injected into the active region from the n and p sides respectively. In a DH laser, the active region that generates optical gain is a thick, bulk layer of semiconductor, typically 100-200nm in thickness.

As a further development of the DH, active regions with lower dimensionality have been explored. By reducing the thickness of the active region to around 10nm or

less, the effect of quantum confinement can be utilised. The carriers in the layer become confined in the direction of the smallest dimension, the direction of growth, z in Figure 2.1 above. This thin layer is known as a quantum well (QW). This process can be extended by reducing the size of the semiconductor in the other two directions, producing a 1 dimensional quantum wire or even a 0 dimensional quantum dot. In this work, quantum well active regions will be focused on. In a laser structure the QW is embedded in a waveguide structure consisting of high refractive index material surrounded by lower index material. This structure provides separate confinement for carriers and photons and is therefore known as a separate confinement heterostructure (SCH). A schematic diagram of the material band gap profile for electrons in the conduction band is shown in Figure 2.2 along with the envelope function for electrons in the z direction. Since this structure also confines light the optical envelope function is also shown. The advantage of confining electrons and photons separately is that each confinement structure may be optimised independently.

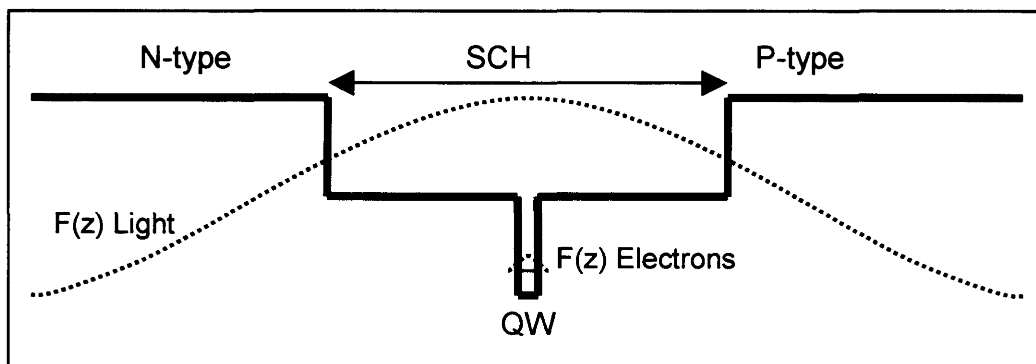

Figure 2.2 Schematic diagram of band gap profile for electrons in a SCH. The dashed lines show envelope functions for electrons and the optical field.

Utilising a QW active region provides several advantages over a bulk active region. These will be discussed in more detail later but include changes to the density of states and the ability to tune the wavelength of emission by changing the well width. The confinement of the carriers in the z direction causes the continuum of states that would appear in a bulk region to form separate subbands with discrete values of k_z. These subbands are spaced separately in energy and are labelled

with the quantum number, n with the n=1 subband being the subband lowest in energy. This subband is shown in Figure 2.2. The quantum confinement effect causes the n=1 subband to be spaced above the bottom of the well by an amount dependent on the well width. This allows further control over the photon energy of light emitted by a QW compared to bulk regions. Due to the QW layers being thin, they can also be grown to incorporate tensile or compressive strain, allowing further control over the band structure. The effects of strain are discussed in the next section.

2.3 Theory of QW semiconductor lasers

In this section, the quantities governing recombination in a QW laser active region are described. The equations that govern recombination, gain, absorption and spontaneous emission rate are derived. These equations show how quantities such as effective mass, matrix element and quasi Fermi levels influence quantities such as gain which can be measured in experiments. Therefore knowledge of the equations derived below is essential in gaining insight into material properties from experimental measurements.

2.3.1 Energy Bands and Effective Mass

In a material with a periodic lattice, the periodicity causes the energy levels present in an individual atom to form separate bands containing a continuum of energy levels. The two energetically highest bands are known as the valence band and conduction band. These two bands are separated in energy with the conduction band being higher in energy than the valence band. The two bands are separated by an energy gap, known as the band gap energy of the crystal, E_g. For a QW, the transition energy increases due to the confinement. As a consequence of this E_g is defined as the energy gap between the bottom of the conduction band and the top of the highest energy valence band.

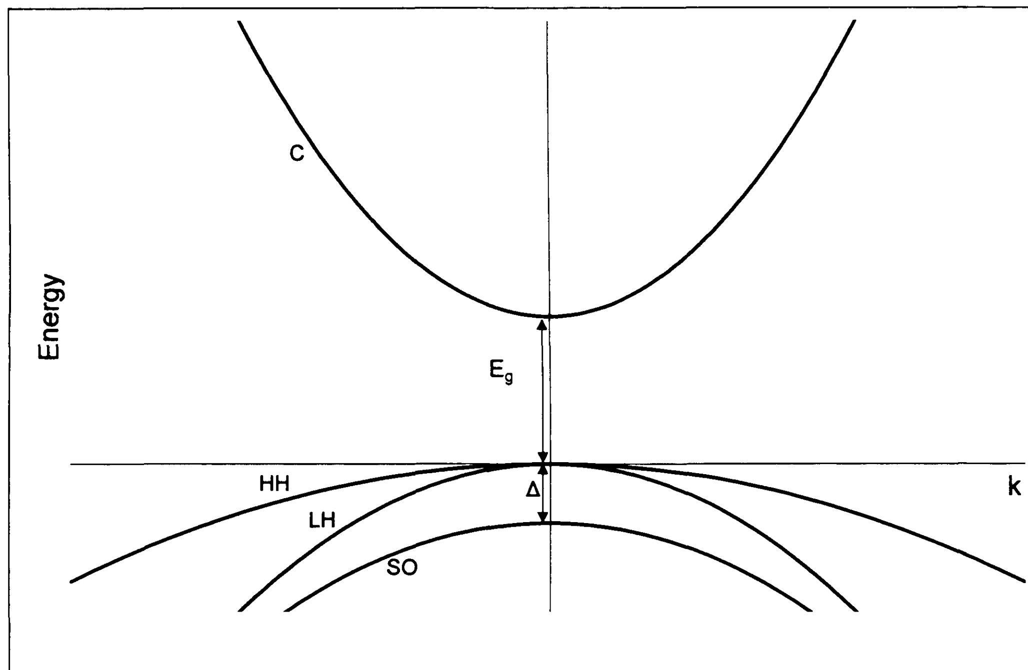

Figure 2.3 Example semiconductor band structure showing conduction band (C), heavy hole (HH), light hole (LH) and split off (SO) valence bands.

Figure 2.3 above shows a typical energy vs wavevector relation for the conduction and valence band in a semiconductor crystal. The conduction band consists of a single band. However, the valence band is split into three bands known as the heavy hole (HH), light hole (LH) and split off (SO) valence bands. The SO band is split from the HH and LH bands, being lower in energy by an amount Δ. At 0K the valence band of a semiconductor is fully occupied by electrons. At temperatures above 0K, or under some external excitation, electrons from the valence band populate the conduction band, leaving behind empty states or holes. The electrons and holes in each band may then recombine; it is this process that produces light. In order to satisfy conservation of momentum, transitions between the bands must take place vertically on the diagram above. The electron and hole must have the same value of k. This rule is known as k-selection.

At values of wavevector k, close to zero, it is often possible to approximate the band structure by a parabola. In this case, the carriers in the crystal can be described in the same way as free carriers, but using an effective mass given by:

$$m^* = \frac{\hbar^2}{d^2E/dk^2}$$

Equation 2.2

The effective mass describes the rate of change of the curvature of the band with changing k.

As mentioned briefly above, one of the advantages of a quantum well active region is the ability to incorporate strain into the well. This is achieved by constructing the well from a material with a lattice constant different to that of the barrier material. If the well material has a larger lattice constant, the well will be compressively strained. A well material with a smaller lattice constant will produce tensile strain. Strain affects the band structure of the quantum well. These effects are greatest in the valence band. Strain causes the HH and LH bands to shift and separate in energy relative to their unstrained position. In the case of compressive strain, the LH band moves to lower energy than the HH band. In the case of tensile strain, the opposite is true. An example valence band structure for a compressively strained well is shown in Figure 2.4. As an example, an InGaAs QW with 40% indium content grown on GaAs is compressively strained by 2.79% and the separation between HH and LH is 133meV [2.2].

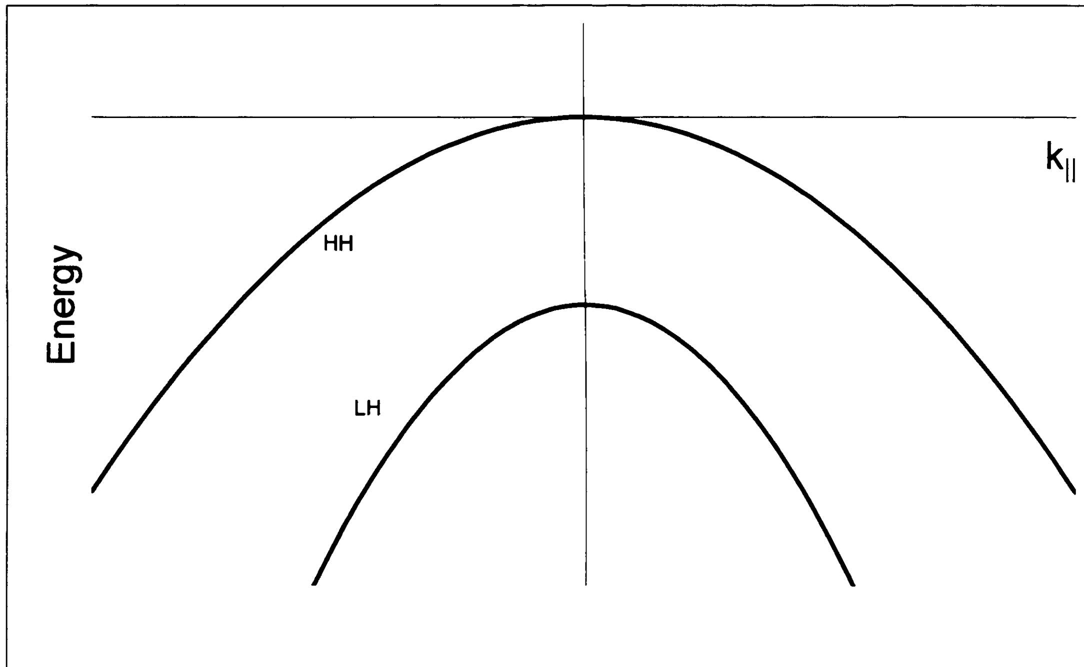

Figure 2.4 Valence band structure for compressively strained quantum well.

2.3.2 Density of States for a Quantum Well

Due to the confinement in the z direction, the density of states for a QW differs to that for a bulk material. This difference is one of the chief advantages a QW active region has over a bulk region. The density of states for bulk and a QW is shown in Figure 2.5.

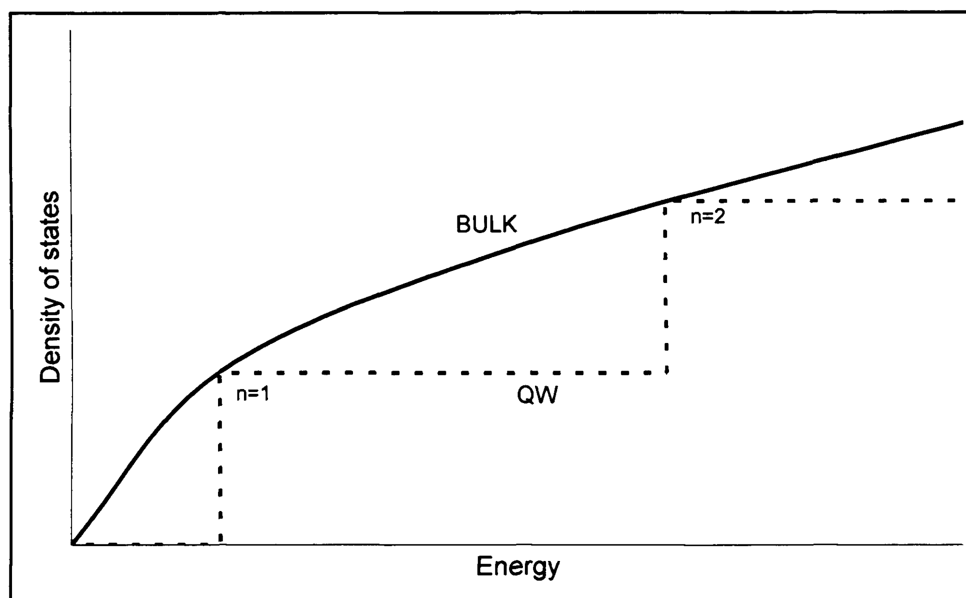

Figure 2.5 Density of states for bulk (solid line) and QW (dashed line) active regions.

As can be seen from the diagram, whilst the bulk density of states is a smooth line, the QW density of states is a series of steps corresponding to each confined subband. The consequence of this is that for a given energy of emission, the QW will require many fewer carriers to achieve threshold conditions, than a bulk region. This results in lower threshold currents for lasers utilising QW active regions.

In understanding the operation of a semiconductor laser it is important to know the form of the density of states function $\rho(E)$. This function describes the number of states per unit energy interval around an energy E. In a QW, carriers are confined to subbands each having a fixed k_Z. However, the carriers are still free to move in the x, y plane, producing a continuum of states associated with this plane. The calculation of density of states below is for a single subband in a QW. Due to the two dimensional nature of a QW, the density of states is a number of states per unit energy interval per unit area.

Cyclic boundary conditions dictate that the area of each state in k space is $(2\pi/L)^2$ [2.4]. The total number states in an interval between k and dk is given by:

$$N = \frac{L^2 kdk}{2\pi}$$

Equation 2.3

Dividing by the area of the sample gives the density of states per unit area per unit k:

$$\rho(k) = \frac{k}{2\pi} dk$$

Equation 2.4

As mentioned above, it is most desirable to know the density of states per unit energy interval, ρ(E). This is related to the density of states per unit k by:

$$\rho(k)dk = \rho(E)dE$$

Equation 2.5

Assuming parabolic bands, the E-k curve is described by:

$$E = \frac{\hbar^2 k^2}{2m^*}$$

Equation 2.6

From Equation 2.4, Equation 2.5 and Equation 2.6 and including a factor 2 to account for spin, the density of states per unit energy interval for a single subband is given by:

$$\rho(E) = \frac{m^*}{\pi\hbar^2}$$

Equation 2.7

Since the effective masses of the conduction and valence bands are not necessarily the same, it is necessary to define a density of states per unit energy interval for the conduction band $\rho_c(E)$ and for the valence band $\rho_v(E)$.

2.3.3 Occupation of States

The transition rate in a semiconductor is in part controlled by the number of states occupied by carriers, n(E). This can be calculated from the number of states available and the probability that the states are occupied.

$$n(E) = \rho(E) f(E)$$

Equation 2.8

If the carriers in the system are in thermal equilibrium, the occupation of states by carriers is described by a Fermi function with temperature, T and controlled by a Fermi level, E_f.

$$f(E) = \frac{1}{1 + \exp\left(\frac{E - E_f}{kT}\right)}$$

Equation 2.9

Separate Fermi functions are required for electrons in the conduction band and holes in the valence band, controlled by different Fermi levels, E_{fc} and E_{fv} respectively. However, if the system is in quasi thermal equilibrium, carriers in either band will have the same temperature, T. The Fermi function describing occupation of conduction band states by electrons is labelled as $f_c(E)$. The occupation of valence band states by electrons is labelled as $f_v(E)$

2.3.4 Transitions between Bands

There are three possible transitions between states in the conduction and valence bands that involve the generation or absorption of a photon. These are illustrated in Figure 2.6.

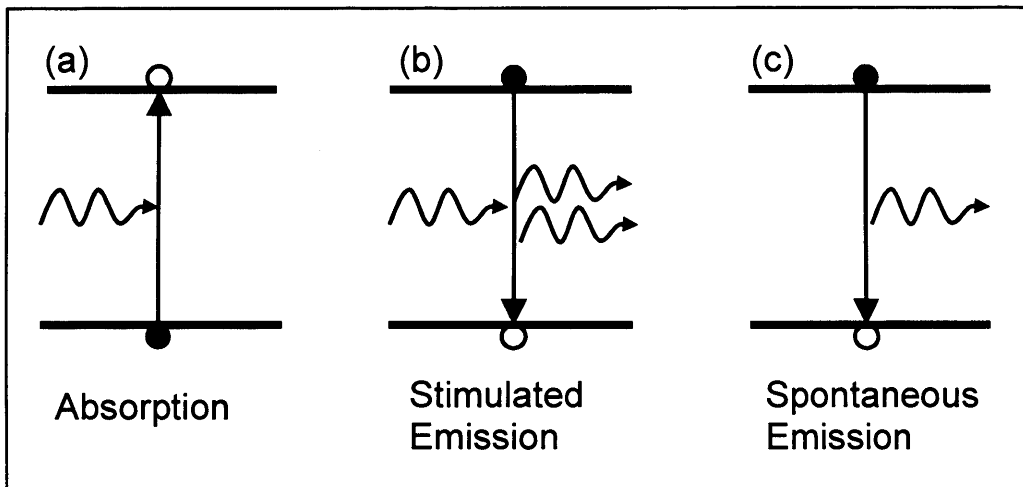

Figure 2.6 Transitions involving photons between two energy states. A solid circle indicates a state occupied by an electron. An open circle indicates a state not occupied by an electron.

The first two are opposites of each other, in the case of (a) an electron is in the valence band, with an unoccupied state in the conduction band. A photon with energy equal to the energy difference between the states is absorbed, exciting the electron from the valence band, into the empty state in the conduction band. This process is absorption. Figure 2.6(b) shows the opposite process, where a passing photon causes an electron in the conduction band to relax into an empty state in the valence band. This process of stimulated emission generates a second photon with the same energy and phase as the original, travelling in the same direction. It is this process that produces coherent emission from a diode laser. The third process is spontaneous emission. In this case, an electron in a conduction band state relaxes into a free valence band state, generating a photon. This process is random and photons are generated travelling in all directions.

2.3.5 Matrix element and Transition rates.

Transitions between states in a material are dictated by Fermi's golden rule. In the case of a discrete initial state (subscript i) and a continuum of final states (subscript f), the transition rate per unit area is given by:

$$R(\hbar\omega) = \frac{2\pi}{\hbar}\left|H'_{if}\right|^2 \rho(\hbar\omega)$$

Equation 2.10

where $\left|H'_{if}\right|^2$ is the matrix element. This determines the strength of the interaction between initial and final states. For a QW, the matrix element may be split into two components and written as:

$$\left|H'_{if}\right|^2 = \left(\frac{e}{2m_0}\right)^2 |M|^2 \left\{\int_V F_f^*(r)A(r)F_i(r)d^3r\right\}^2$$

Equation 2.11

The first component $|M|^2$ is due to the microscopic potential of the atomic lattice of the material that makes up the well. This is known as the momentum matrix element. The second term, in {}, is due to the macroscopic potential of the well. This is known as the overlap integral. The functions F(r) in the x and y directions are the plane wave solutions of Schrödinger's equation. For a QW potential,

$$F(r) = F(z)\frac{e^{-jk.r_{\parallel}}}{\sqrt{A}}$$

Equation 2.12

where $r_{\parallel}$ is a position vector in the x, y plane.

The overlap integral is only non - zero for transitions between plane wave solutions having the same value of k. This is the mathematical description of momentum conservation.

From Equation 2.11 and Equation 2.12, the transition rate can be written as

$$R(\hbar\omega) = \frac{2\pi}{\hbar}\left(\frac{e}{2m_0}\right)^2 |M|^2 \left\{\int F_f^*(z)A(z)F_i(z)dz\right\}^2 \rho_f(\hbar\omega)$$

Equation 2.13

Equation 2.13 gives the transition rate in a QW from a discrete initial state to a continuum of final states. However, in reality these transitions take place between the conduction and valence bands in a semiconductor. Therefore both initial and final states are part of a continuum. In this case, the density of states function appearing in Equation 2.13 must be the reduced density of states, $\rho_r(\hbar\omega)$. This function takes into account the continuum of states and also the rules of k-selection. The reduced density of states is given by:

$$\frac{1}{\rho_r} = \frac{1}{\rho_c} + \frac{1}{\rho_v}$$

Equation 2.14

Equation 2.13 also assumes the initial state is full and the final state is empty. To account for situations when this is not the case, the probability of the states being occupied must also be included. This gives an expression for downward transitions between conduction band and valence band:

$$R_{\downarrow}(\hbar\omega) = \frac{2\pi}{\hbar}\left(\frac{e}{2m_0}\right)^2 |M|^2 \left\{\int F_v^*(z)A(z)F_c(z)dz\right\}^2 \rho_r(\hbar\omega) f_c(1-f_v)$$

Equation 2.15

In the above equation, f_c and f_v are the probabilities that a state is occupied by an electron in the conduction and valence bands respectively. The upward transition rate is the same but with the suffixes on the occupation probabilities reversed. This gives a net downward transition rate of:

$$R_{net}(\hbar\omega) = \frac{2\pi}{\hbar}\left(\frac{e}{2m_0}\right)^2 |M|^2 \left\{\int F_v^*(z)A(z)F_c(z)dz\right\}^2 \rho_r(\hbar\omega)(f_c - f_v)$$

Equation 2.16

2.3.6 Equation for Modal Gain

The gain experienced by an optical mode is defined as the fractional increase in the total energy density in the mode. In terms of time this is given by:

$$G_t = \frac{1}{W_{tot}}\frac{dW_{tot}}{dt}$$

Equation 2.17

where G is the modal gain and W_{tot} is the total energy density in the mode.

Equation 2.17 gives a gain per unit length of

$$G = \frac{n_g}{c}\frac{1}{W_{tot}}\frac{dW_{tot}}{dt}$$

Equation 2.18

where (c/n_g) is the group velocity of the mode.

For a beam of width w, having travelled a length ΔL,

$$\frac{dW_{tot}}{dt} = (\hbar\omega)R_{net}w\Delta L$$

Equation 2.19

where ($\hbar\omega$) is the photon energy and R_{net} is the net downward transition rate.

For harmonically varying fields the local energy density is:

$$W(r) = \frac{1}{2} n n_g \varepsilon_0 \omega^2 |A(r)|^2$$

Equation 2.20

where A(r) is the vector potential and related to the electric field strength (ε) by $|\varepsilon|^2 = \omega^2 |A(r)|^2$ for time-harmonic fields and n is the refractive index. The total energy density in the mode is:

$$W_{tot} = \frac{1}{2} n n_g \varepsilon_0 \omega^2 \left(\int A^2(z) dz \right) w.\Delta L$$

Equation 2.21

Putting Equation 2.16 into Equation 2.19 and combining with Equation 2.18, and Equation 2.21 gives an expression for the modal gain of:

$$G(\hbar\omega) = \frac{4\pi\hbar}{nc\varepsilon_0(\hbar\omega)} \left(\frac{e}{2m_0} \right)^2 |M|^2 \left\{ \int F_v^*(z) A(z) F_c(z) dz \right\}^2 \rho_r(h\nu)(f_c - f_v) \frac{1}{\int A^2(z) dz}$$

Equation 2.22

Finally, the quantity A(z) in the term in {} varies very little over the range of the well width and can be treated as having a constant value, A_{well} This allows it to be removed from the integration. This gives the final equation for modal gain:

$$G(\hbar\omega) = \left[\frac{4\pi\hbar}{nc\varepsilon_0(\hbar\omega)} \left(\frac{e}{2m_0} \right)^2 |M|^2 \left\{ \int F_v^*(z) F_c(z) dz \right\}^2 \rho_r(h\nu)(f_c - f_v) \frac{1}{L_z} \right] \Gamma$$

Equation 2.23

In the above equation L_z is the quantum well width, the term in [ ] is referred to as the material gain and Γ is the optical confinement factor, defined as:

$$\Gamma = \frac{A_{well}^2 L_z}{\int A^2(z)dz}$$

Equation 2.24

2.3.7 Equation for spontaneous emission

Spontaneous emission is the same transition as stimulated emission, but occurs in the absence of an incoming photon. It can be shown that spontaneous emission is the stimulated emission due to the optical field from a single photon [2.1]. Thus the spontaneous emission rate into a single mode (R_{spon}^1) can be calculated by inserting the vector potential for a single photon into Equation 2.15. The vector potential for a single photon is given by:

$$|A|^2 = \frac{2(\hbar\omega)}{n^2\varepsilon_0\omega^2 V_{mode}}$$

Equation 2.25

To calculate the total spontaneous emission rate into all modes, the rate for a single mode is multiplied by the total number of available modes. The mode density per unit volume is given by

$$\rho_0(\hbar\omega) = \frac{n^2 n_g}{\pi(\hbar c)^3}(\hbar\omega)^2$$

Equation 2.26

This gives the total number of modes available when multiplied by the total volume (V_{box}). For in plane lasers, V_{mode} and V_{box} can be assumed to be the same. This gives the spontaneous emission rate per unit area per unit energy interval into all modes as:

$$R_{spon}(\hbar\omega) = \frac{4n}{\varepsilon_0 \pi c^3 \hbar^2}(\hbar\omega)\left(\frac{e}{2m_0}\right)^2 \left|\overline{M}\right|^2 \left\{\int F_v^*(z) F_c(z) dz\right\}^2 \rho_r(\hbar\omega) f_c(1-f_v)$$

Equation 2.27

where $\left|\overline{M}\right|^2$ is the average matrix element over all directions and polarisations. The average refractive index experienced by all modes has been taken to be the refractive index n.

2.3.8 Non radiative and leakage processes.

As well as the transitions producing or absorbing photons discussed in Section 2.3.4 there are other processes for recombination between electrons and holes. These are illustrated in Figure 2.7.

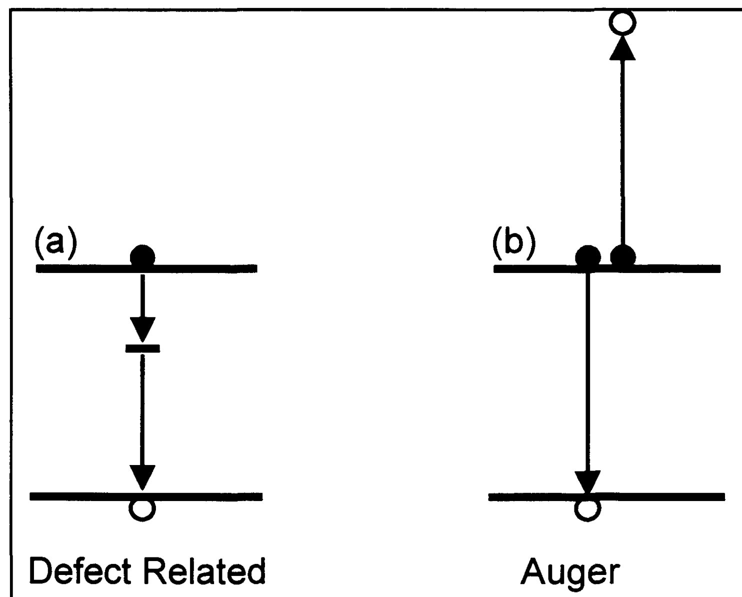

Figure 2.7 Non radiative transitions between initial and final energy states.

The first process is recombination due to defects in the crystal structure. These defects can produce states positioned in energy between the conduction and valence bands. The electron and hole may recombine via these states and the energy lost transferred to the crystal lattice. The second process is an example of

Auger recombination. In this case, an electron and hole recombine across the band gap but the energy lost is transferred to a second electron in the conduction band, exciting it to higher energy. In order to satisfy conservation of momentum, Auger transitions must occur diagonally on Figure 2.3.

As well as these two non radiative processes there is another method where by carriers may pass through the sample without contributing to light output. This occurs when the confinement of the well is small relative to kT. In these circumstances carriers may have enough energy to escape the confinement of the well and recombine elsewhere in the sample. This process is referred to as thermally activated leakage due to the fact that it is greatly increased at high temperatures.

In order to calculate the total current density passing through a laser sample the current densities due to all available processes must be summed:

$$J_{tot} = J_{rad} + J_{defect} + J_{Auger} + J_{leak}$$

Equation 2.28

2.4 Dilute Nitride semiconductor material for emission at 1.3μm

2.4.1 Importance of emission at 1.3μm

For high speed communication through optical fibres, it is vital to have lasers emitting light in wavelength ranges suitable for transmission through fibres. In standard silica fibre there are 3 wavelength windows for light transmission. The first of these is at 0.85μm. This window was very important, but as Figure 2.8 shows, for modern fibres the minima at 0.85μm is less pronounced. The other two wavelength windows which are of greater importance are at 1.3μm and 1.55μm

these correspond to two minima in the losses experienced when passing through an optical fibre. The loss curve for an optical fibre is shown in Figure 2.8.

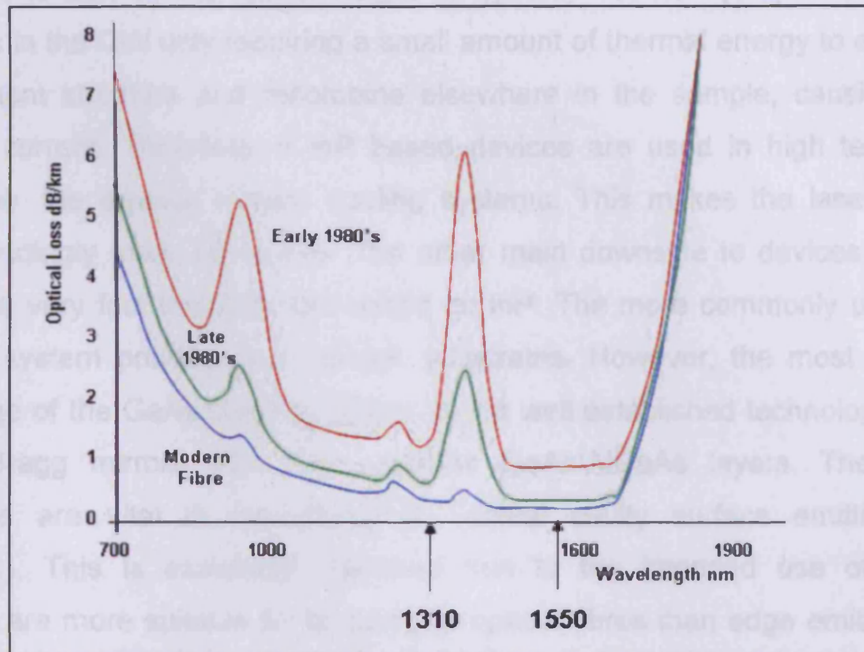

Figure 2.8 Loss curve for standard silica fibre taken from [2.5]

It is for this reason that there is so much interest in laser devices emitting at 1.3μm and 1.55μm. The window at 1.3μm also corresponds to the minima in dispersion through a fibre. This work is concerned with laser structures designed to emit at or around this 1.3μm wavelength window.

2.4.2 Current material systems for 1.3μm emission

Optical fibres are fast becoming the standard land based communication medium over extended distances such as across oceans. However, for short haul communication systems the use of optical communications is much less widespread. This is in part due to the expensive nature of lasers emitting at the required wavelengths. The material system most commonly used for 1.3μm emission is InP based. The lattice constant of InP allows growth of GaInPAs quantum wells for emission at 1.3μm. Whilst these structures provide light emission at the desired wavelength, they carry with them several undesirable characteristics.

One of these is poor performance of laser devices when operated at elevated temperatures. The confinement of the electrons in the conduction band in these structures is low, with a barrier height of typically 100meV [2.6]. This results in electrons in the QW only requiring a small amount of thermal energy to escape the confinement structure and recombine elsewhere in the sample, causing a high leakage current. Therefore, if InP based devices are used in high temperature conditions, the devices require cooling systems. This makes the laser package correspondingly more expensive. The other main downside to devices based on InP is the very fact that they are based on InP. The more commonly used GaAs material system provides for cheaper substrates. However, the most significant advantage of the GaAs material system is the well established technology used to create Bragg mirrors from high contrast GaAs/AlGaAs layers. These mirror structures are vital in manufacturing vertical cavity surface emitting lasers (VCSELs). This is especially important due to the intended use of emitters. VCSELs are more suitable for coupling to optical fibres than edge emitting lasers due to the symmetry of the output beam [2.7]. The InP material system does not provide the high contrast layers desirable for Bragg mirrors. The low contrast requires a large number of layers to grow Bragg mirrors, making VCSELs more complicated to grow.

2.4.3 InGaAsN

Several material structures have been put forward as solutions to the problems outlined above. These include the use of quantum dot active regions grown on GaAs substrates. The material system studied in this work is another candidate to provide solutions to the problems faced by the InP devices and enable growth on GaAs. This material system is InGaAsN. First proposed by Kondow et al in 1996 [2.8] this material involves the use of QW active regions incorporating a small percentage of nitrogen. The use of nitrogen is due to the unusual behaviour between lattice constant and bandgap energy. A plot of lattice constant vs bandgap energy for several common semiconductors is shown in Figure 2.9.

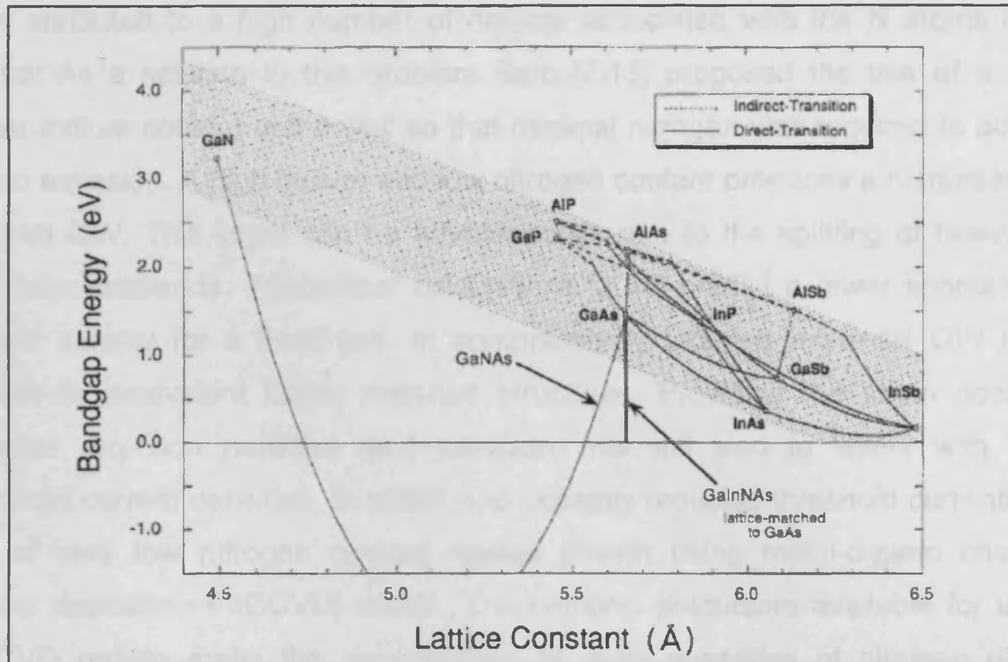

Figure 2.9 Bandgap energy vs lattice constant for some common material systems reproduced from [2.8]

The figure shows the interesting feature of dilute nitride compounds. This feature is that the bandgap decreases with decreasing lattice constant. For the other materials shown in the figure, the opposite is true. It is this feature of the dilute nitrides that enables their growth on GaAs. In the case of InGaAsN there is a range of compositions that can be grown lattice matched to GaAs which gives a range of available emission wavelengths. These are shown as the solid vertical line in Figure 2.9. The ability to be grown on GaAs allows the fabrication of high contrast Bragg mirrors as described above. When grown on GaAs, the confinement of the electrons in an InGaAsN QW is very good, approximately 350-450meV [2.8, 2.9]. This is significantly higher than for the InP based devices and should greatly reduce thermal leakage problems.

Early devices fabricated using molecular beam epitaxy (MBE) and grown lattice matched to GaAs showed good temperature stability as described by a high T_0 value [2.10,2.11,2.12]. However, the high temperature operation was accompanied by high threshold current densities. The high current densities needed for lasing

were attributed to a high number of defects associated with the N atoms in the crystal. As a solution to this problem Sato [2.13] proposed the use of a much higher indium content in the well so that minimal nitrogen was required to achieve 1.3μm emission. A high indium and low nitrogen content produces a compressively strained QW. This strain can be advantageous due to the splitting of heavy and light hole subbands. Theoretical calculations [2.14] predict a lower spontaneous current density for a fixed gain in compressively strained InGaAsN QW lasers relative to equivalent lattice matched structures. Providing the strain does not increase any non radiative recombination, this will lead to lasers with lower threshold current densities. In addition to possibly reducing threshold currents, the use of very low nitrogen content makes growth using metal-organo chemical vapour deposition (MOCVD) easier. The nitrogen precursors available for use in MOCVD growth make the incorporation of large quantities of nitrogen difficult [2.15]. MOCVD is the more attractive technology for the growth of VCSELs as it allows a faster growth of the relatively thick mirror layers compared to MBE. The use of high indium content highly strained InGaAsN wells together with more mature growth techniques has resulted in devices operating with much lower threshold current densities, but the reduction in threshold has produced an increased variation of threshold current density with temperature, illustrated by a decrease in the T_0 parameter [2.16,2.17].

Whilst the T_0 parameter is widely used, its significance must be interpreted with care. T_0 is calculated from the threshold current density (J_{th}) and its variation with temperature using:

$$\frac{1}{T_0} = \frac{1}{J_{th}} \frac{dJ_{th}}{dT}$$

Equation 2.29

This definition illustrates the problem with T_0. A high value is desirable, but this can be achieved by a device with a high threshold current density. This produces an artificial temperature stability which is simply due to a laser with a high threshold.

As a result, a high T_0 accompanied by a high threshold current density and a low threshold current density being accompanied by a low T_0 may not come as a surprise.

The effect that the amount of nitrogen in the QW has on the optical characteristics of the material is of great interest. There have been several experimental and theoretical studies on structures with varying indium and nitrogen concentrations. Experimental results show threshold currents increasing with nitrogen content. The reasons for this have been attributed to an increase in defect recombination [2.18] or thermal leakage of holes [2.9]. There is also the possibility of increased Auger recombination with increased nitrogen content. Despite the volume of ongoing research the relative importance of these processes is still uncertain. Theoretical models [2.9,2.21,2.22,2.23] have predicted a reduction in the matrix element with increasing nitrogen content and an increase in the conduction band effective mass. It is believed that the presence of nitrogen in the QW has little effect on the valence band effective mass [2.24]. The changes in matrix element and conduction band effective mass should bring about a reduction in the transition rate in a structure containing nitrogen relative to an equivalent nitrogen free structure for the same carrier density. As described by Equation 2.13, this reduction in transition rate would produce a reduced maximum absorption, a reduction in the maximum gain for a given quasi Fermi level separation and a reduction in radiative recombination as nitrogen content increases. Theoretical models also provide predictions of similar gain radiative current characteristics with or without the presence of nitrogen. However, there are very few experimental results confirming or illustrating these theoretical predictions.

This work aims to contribute to the understanding of the effect of nitrogen in InGaAsN QW laser structures. This understanding will be gained by experimental means. Of particular interest is the effect that changing the nitrogen concentration has on the optical properties of the material. To investigate these effects, the quantities measured in experiments must allow for theoretical interpretation so that the effect of changes in the material properties can be examined. Knowledge of the

relative importance of the different non-radiative recombination mechanisms is important in producing lasers with low threshold current densities. Once the recombination processes are understood, steps can be taken in the fabrication of laser samples to minimise the non radiative recombination rates. Studying the non-radiative recombination mechanisms in dilute nitride structures and how they vary with nitrogen content is the key aim in this thesis.

2.5 References

2.1 L. A. Coldren, S. W. Corzine, "Diode lasers and Photonic Integrated Circuits" Wiley, New York (1995)

2.2 P. Zory, "Quantum Well Lasers" Academic Press, San Diego (1993)

2.3 P. Blood, *IEEE J Quan Elec*, **36**, (2000) 354

2.4 J. R. Hook, H. E. Hall, "Solid State Physics – second edition", John Wiley and Sons, Chichester (1991)

2.5 A Keene, "Measurements of Optical Cables" www.trendcomms.com

2.6 M. Silver, E. P. O'Reilly, *IEEE J Quan Elec*, **31**, (1995) 1193

2.7 V. M. Ustinov and A. E. Zhukov, Semicond Sci Technol, **15**, (2000) R41

2.8 M. Kondow, T. Kitani, S. Nakatsuka, M. C. Larson, K. Nakahara, Y. Yazawa, M. Okai, *IEEE J. Sel Top Quantum Electron*, **3** (1997) 719

2.9 N. Tansu, L. J. Mawst, *Appl Phys Letts,* **82**, (2003) 1500

2.10 N. Tansu, L. J. Mawst, *IEEE Photonics Technol Lett*, **14** (2002) 1052

2.11 R. Fehse, S. Tomic, A. R. Adams, S. J. Sweeney, E. P. O'Reilly, H. Riechert, IEEE *J Sel Top Quantum Electron*, **8** (2002) 801

2.12 M. Kondow, T. Kitatani, K. Nakahara, T. Tanaka, *Jpn J Appl Phys*, **38** (1999) L1355

2.13 S. Sato, *Jpn J Appl Phys*, **39** (2000) 3403

2.14 W. W. Chow, E. D. Jones, N. A. Modine, A. A. Allerman, S. R. Kurtz, *Appl Phys Letts*, **75** (1999) 2891

2.15 N. Tansu, J. Y. Yeh, L. J. Mawst, *IEEE J. Select Topics Quantum Electron.*, **9** (2003) 1220

2.16 D. A. Livshits, A. Yu. Egorov, H. Riechert, *Electron Letts*, **36** (2000) 1381

2.17J. Wei, F. Xia, C. Li, S. R. Forrest, *IEEE Photonics Technol Lett* **14** (2002) 597

2.18 R. Fehse, S. Jin, S.J. Sweeney, A. R. Adams, E. P. O'Reilly, H. Riechert, S. Illek, A. Yu. Egorov, *Elec Letts*, **37** (2001) 1518

2.19 D. Alexandropoulos, M. J. Adams, *J. Phys.: Condens. Matter* **14** (2002) 3523

2.20 S. Tomić, E. P. O'Reilly, R. Fehse, S. J. Sweeney, A. R. Adams, A. D. Andreev, S. A. Choulis, T. J. C. Hosea, H. Riechert, *IEEE J. Select Topics Quantum Electron.*, **9** (2003) 1228

2.21 C. Skierbiszewski, P. Perlin, P. Wisniewski, W. Knap, T. Suski, W. Walukiewicz, W. Shan, K. M. Yu, J. W. Ager, E. E. Haller, J. F. Geisz, J. M. Olsen, *Appl Phys Letts*, **76** (2000) 2409

2.22 J. M. Ulloa, J. L. Sánchez-Rojas, Adrian Hierro, J. M. G. Tijero, E. Tournié, *IEEE J. Select Topics Quantum Electron.*, **9** (2003) 716

2.23 M. Hetterich, M. D. Dawson, A. Yu. Egorov, D. Bernklau, H. Riechert, *Appl Phys Letts*, **76** (2000) 1030

2.24 M. S. Wartak, P. Weetman, *J. Appl Phys*, **98** (2005) 113705

Chapter 3 Experimental Method

3.1 Introduction

In this chapter the experimental method used to measure net modal gain, loss and spontaneous emission spectra is described. The technique is known as the segmented contact method. Details of the test structure required, data that is measured and the equations necessary to analyse this data are presented. The process of calibrating the spontaneous emission and hence calculating the radiative current density and overall internal quantum efficiency is explained. Following this is a description of the equipment used for data collection and the improvements made to this data collection system during this project. Finally there is a section discussing checks made on the experimental equipment to ensure it is used in the best way and produces reliable results. This includes comparisons between measurement systems and the treatment of errors in the experiments.

3.2 Techniques available to study laser structures.

There are several different experimental techniques which may be employed to study the InGaAsN material system. Each of these techniques has its advantages and disadvantages.

The most commonly used method to study laser samples is to measure the threshold current density of lasers with different cavity lengths. This method has the advantage of being relatively straightforward to carry out. Whilst it is a useful way to compare different laser structures, it can only provide limited information on the optical properties of the material being studied.

Another measurement technique is the Hakki-Paoli method [3.1]. In these experiments the modal gain spectra of a laser structure can be measured. However, to achieve this, a measurement system capable of very high resolution is

required. In addition, the modal gain spectra can only be measured until the threshold gain of the laser.

An extension of the first method described above involves the measurement of the spontaneous emission from a top contact window as well as threshold current densities for lasers of different lengths. By using mathematical fits to this data, the spontaneous emission may then be calibrated and the recombination mechanisms investigated. This method relies heavily on assumed mathematical relationships and because the spontaneous emission is measured from the top of the device only TE polarised light may be studied.

3.3 The Segmented Contact Method

The experimental method chosen for this work is known as the segmented contact method. The details of the method are described in the following sections. This technique has several advantages over those described above. It allows measurement of gain and spontaneous emission rate spectra from the end of a device. This allows the study of both TE and TM polarised light. In addition, the method allows the measurement of modal absorption spectra. This is a significant advantage as it allows comparison between theory and experiment without requiring knowledge of the injection level in the structure.

3.3.1 Device Structure and Amplified Spontaneous Emission

In this method, single pass amplified spontaneous emission (ASE) spectra are measured as a function of pumped length. This technique is a variation of the method introduced by Shanklee and Leheny [3.2] where optical pumping was used to excite the sample. Their method was extended to allow electrical injection first by Oster [3.3], and then by Thomson [3.4]. This work uses the method set out in [3.4]. The ASE spectra are collected from a test structure processed from laser diode material. This structure consists of several independently contacted sections of material on the same semiconductor chip. The chip is divided into sections along the optical waveguide. In this arrangement, the light from one section is coupled

into the adjoining sections, allowing different lengths to be pumped electrically. Electrical isolation between the sections is achieved by etching 4μm wide channels into the GaAs cap layer and the metal contacts. A schematic of the test structure is shown in Figure 3.1.

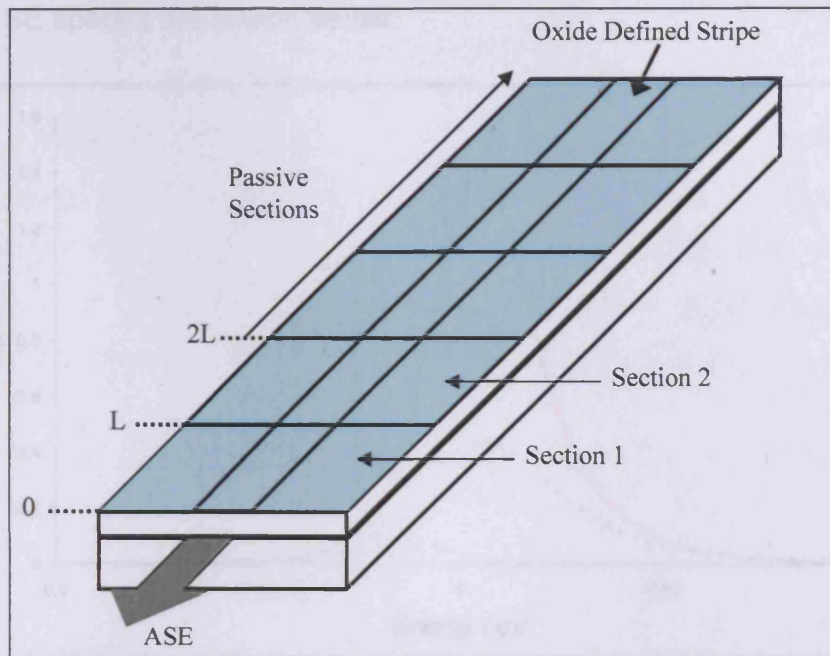

Figure 3.1 Segmented contact test structure where current can be injected through the central oxide isolated stripe.

To allow analytical solutions for the equations for net modal absorption, net modal gain and spontaneous emission rate, the length of each section is the same, and of length L as shown in the diagram. ASE spectra are collected from the end of the device and only from driving the front two sections, labelled section 1 and section 2. The remaining sections form a passive absorbing region which inhibits round trip amplification. This is necessary to ensure a single pass measurement. In this work all the devices studied had a standard oxide stripe current confinement structure with a nominal stripe width of 50μm and the section length L was 300μm. With the two independent contacts, there are three possible ASE spectra that can be measured. If the front section alone, section 1, is pumped to a certain current density, an ASE from length L is measured ($I_{ASE}^{meas}(1)$). By then pumping only section

2 to the same current density, an ASE from length L is also measured ($I_{ASE}^{meas}(2)$) but with the light having passed through the front section and undergone absorption. Pumping sections 1 and 2 together, at the same current density as section one and two alone were pumped, gives an ASE signal from length 2L ($I_{ASE}^{meas}(1,2)$). Examples of these ASE spectra are shown below.

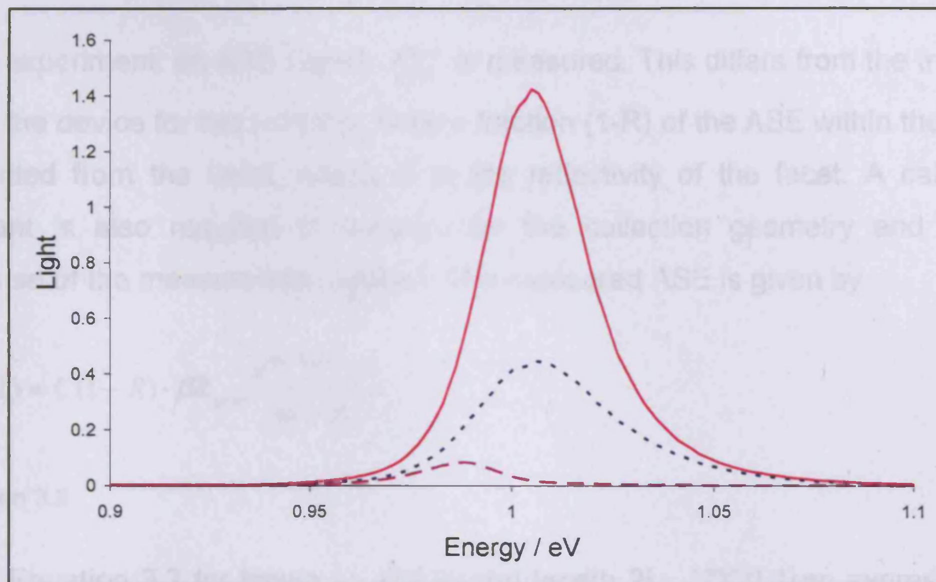

Figure 3.2 Example ASE showing spectra produced when driving sections 1 and 2 (solid line), section 1 (small dashes) and section 2 (large dashes). The spectra are for an InGaAsN QW with 0.5% nitrogen measured at 200K.

These three ASE spectra allow calculation of modal absorption, modal gain and spontaneous emission spectra.

3.3.2 Net Modal Gain and Spontaneous Emission

In this analysis, the emitting material is treated as being homogenous and consisting of individual light emitting centres that can be characterised by a total spontaneous emission spectrum R_{spon}. The analysis follows that shown in [3.5]. For a spontaneous emission rate (R_{spon}) the ASE with a specific polarisation emitted into the waveguide from a length L, is:

$$I_{ASE}(L) = \beta R_{spon} \frac{e^{(G-\alpha_i)L} - 1}{G - \alpha_i}$$

Equation 3.1

where β is the fraction of spontaneous emission coupled to the waveguide and G is the modal gain and α_i is the internal optical mode loss.

In the experiment, an ASE signal, I_{ASE}^{meas} is measured. This differs from the true ASE within the device for two reasons. Only a fraction (1-R) of the ASE within the device is emitted from the facet, where R is the reflectivity of the facet. A calibration constant is also required to account for the collection geometry and system response of the measurement system. The measured ASE is given by

$$I_{ASE}^{meas}(L) = C(1-R) \cdot \beta R_{spon} \frac{e^{(G-\alpha_i)L} - 1}{G - \alpha_i}$$

Equation 3.2

Using Equation 3.2 for length L, $I_{ASE}^{meas}(1)$ and length 2L, $I_{ASE}^{meas}(1,2)$ an expression for the net modal gain (G-α_i) can be determined

$$G - \alpha_i = \frac{1}{L} \ln\left(\frac{I_{ASE}^{meas}(1,2)}{I_{ASE}^{meas}(1)} - 1 \right)$$

Equation 3.3

This equation allows the net modal gain spectrum to be calculated in real units of cm^{-1}. Examples of net modal gain spectra appear in Figure 3.3. The different net modal gain curves correspond to a range of drive current densities, with the peak gain increasing as the current density is increased. At low photon energies, the gain spectra for different current densities all tend to the same value. These photon energies are below the band edge of the material and as such experience no gain or absorption. The loss experienced by photons at these energies is identified as

the internal optical loss, α_i enabling the modal gain to be calculated from Equation 3.3. The point at which the gain spectra cut a line equal to the value of negative α_i at high energy is identified as the transparency point. This is the point where the gain and absorption from the material are equal. If the system is in thermal equilibrium, this point in energy is the experimentally determined quasi Fermi level separation. The dashed line on this plot is an example of a net modal absorption spectrum. The process for measuring this is discussed below.

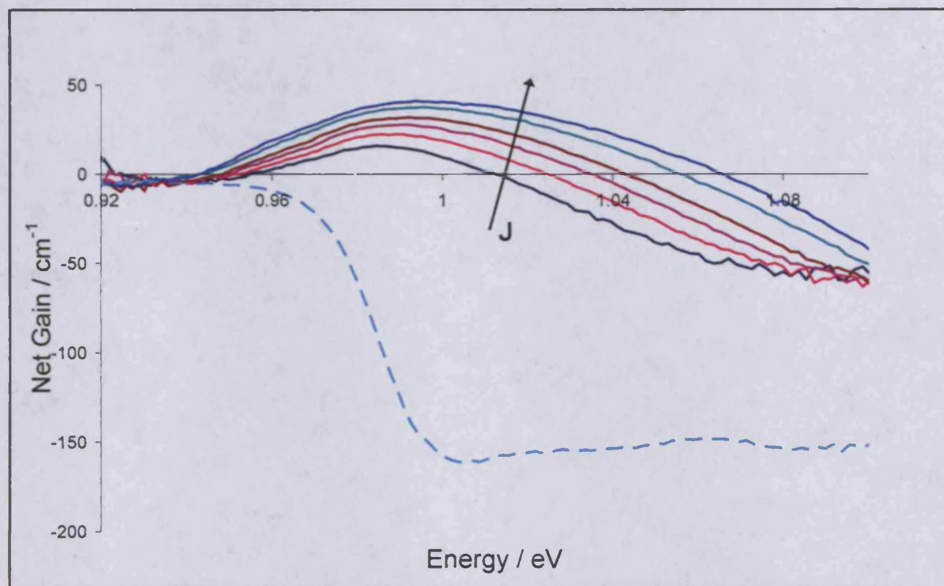

Figure 3.3 Example gain (solid lines) and loss (dashed line) spectra for an InGaAsN QW at 300K.

Using Equation 3.2 for the same lengths and corresponding measured ASE signals used to calculate net modal gain, the measured spontaneous emission rate is given by:

$$I_{Spon}^{meas} = \frac{1}{L}\ln\left(\frac{I_{ASE}^{meas}(1,2)}{I_{ASE}^{meas}(1)} - 1\right)\frac{I_{ASE}^{meas}(1)^2}{I_{ASE}^{meas}(1,2) - 2I_{ASE}^{meas}(1)}$$

Equation 3.4

Examples of spontaneous emission rate spectra are shown in Figure 3.4. As with the net modal gain spectra the different curves correspond to different drive current

densities, with there being more spontaneous emission at higher current densities. It is important to note that whilst the modal gain spectra are calculated in real units of cm^{-1}, the spontaneous emission rate spectra come out of the calculation in the arbitrary units of the experimental setup.

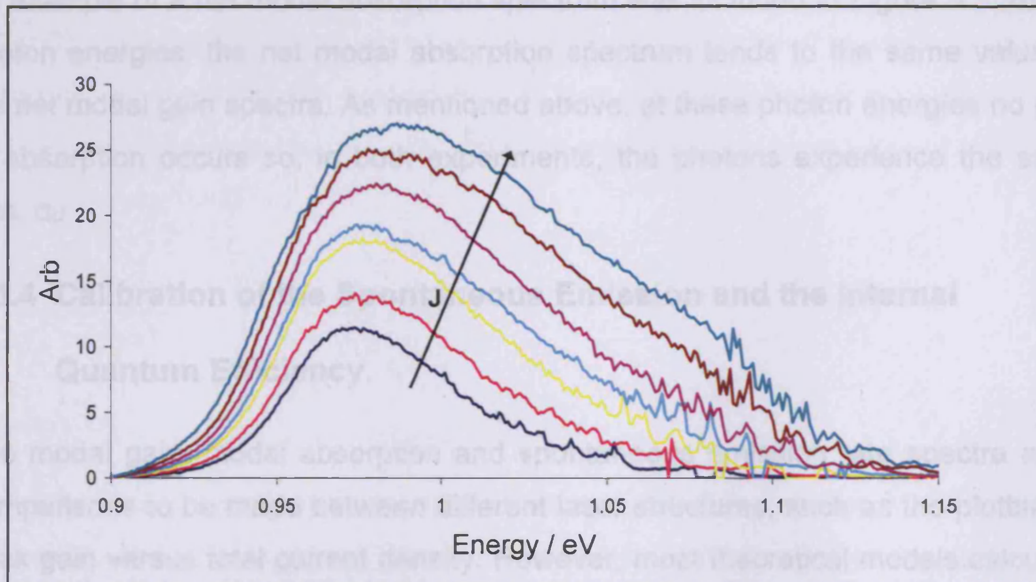

Figure 3.4 Example spontaneous emission spectra for an InGaAsN QW at 300K

3.3.3 Net Modal Absorption

When the ASE from section 2 is measured, it has passed through section 1 and undergone absorption. With identical sections and assuming 100% coupling between the sections, the light entering the waveguide at section 2 and experiencing this absorption is identical to that measured when section 1 alone is pumped. The ASE detected from section 2 is then given by:

$$I_{ASE}^{meas}(2) = I_{ASE}^{meas}(1)e^{-(A+\alpha_i)L}$$

Equation 3.5

where A is the modal absorption. This equation can be rearranged to give an expression for the net modal absorption.

$$A + \alpha_i = \frac{1}{L}\ln\left(\frac{I_{ASE}^{meas}(2)}{I_{ASE}^{meas}(1)}\right)$$

Equation 3.6

An example of a net modal absorption spectrum was included in Figure 3.3. At low photon energies, the net modal absorption spectrum tends to the same value as the net modal gain spectra. As mentioned above, at these photon energies no gain or absorption occurs so, in both experiments, the photons experience the same loss, α_i.

3.3.4 Calibration of the Spontaneous Emission and the Internal Quantum Efficiency.

The modal gain, modal absorption and spontaneous emission rate spectra allow comparisons to be made between different laser structures, such as the plotting of peak gain versus total current density. However, most theoretical models calculate peak gain versus radiative current density. It is therefore this quantity that is required for comparisons to be made between theory and experiment. The radiative current density is also needed to identify the recombination mechanisms responsible for current flow through a laser structure. The radiative current density is equal to the area under the spontaneous emission rate spectra multiplied by the electronic charge, given by:

$$J_{rad} = e \cdot \int R_{Spon} dh\nu$$

Equation 3.7

At first this appears straight forward to calculate. However, as mentioned previously the spontaneous emission rate spectra measured in the experiment are in arbitrary units. In Equation 3.7, the spontaneous emission rate is that within the device, in real units. The true spontaneous emission rate is related to the measured spontaneous emission rate (I_{spon}) by

$$R_{Spon} = \frac{1}{\beta C(1-R)} \cdot I_{spon}$$

Equation 3.8

Therefore to calculate the true spontaneous emission rate spectra the constant βC(1-R) must be evaluated. One way to achieve this calibration is by examining the inversion factor for the system. For a conventional quantum well, of width L_z and with confinement factor Γ, the ratio of modal gain to spontaneous emission rate is given by: [3.5]

$$\frac{G}{R_{spon}} = \frac{3\hbar^3 c^2 \pi^2}{n^2 (\hbar\omega)^2} \left(\frac{\Gamma}{L_z}\right) \left(\frac{f_1 - f_2}{f_1(1-f_2)}\right)$$

Equation 3.9

This equation is true for a single polarisation and with the spontaneous emission in real units. The factors f_1 and f_2 are the occupation probabilities of the upper and lower states respectively. Using these, the population inversion factor can be defined.

$$P_f = \frac{f_1 - f_2}{f_1(1-f_2)}$$

Equation 3.10

From this equation it can be seen that when the system is fully inverted ($f_1 = 1$ and $f_2 = 0$). The inversion factor is equal to one. However, the inversion factor will also equal one when either $f_1 = 1$ or $f_2 = 0$. Using this and the calibration constant C' (=βC(1-R)) to transform into the arbitrary units of the experiment relates the inversion factor to the experimentally measured modal gain and spontaneous emission rate by:

$$P_f = C'\frac{n^2(\hbar\omega)^2}{3\hbar^3c^2\pi^2}\left(\frac{L_z}{\Gamma}\right)\left(\frac{G}{I_{spon}}\right)$$

Equation 3.11

From the experimental data, the ratio of modal gain to measured spontaneous emission rate can be plotted and this is shown in Figure 3.5.

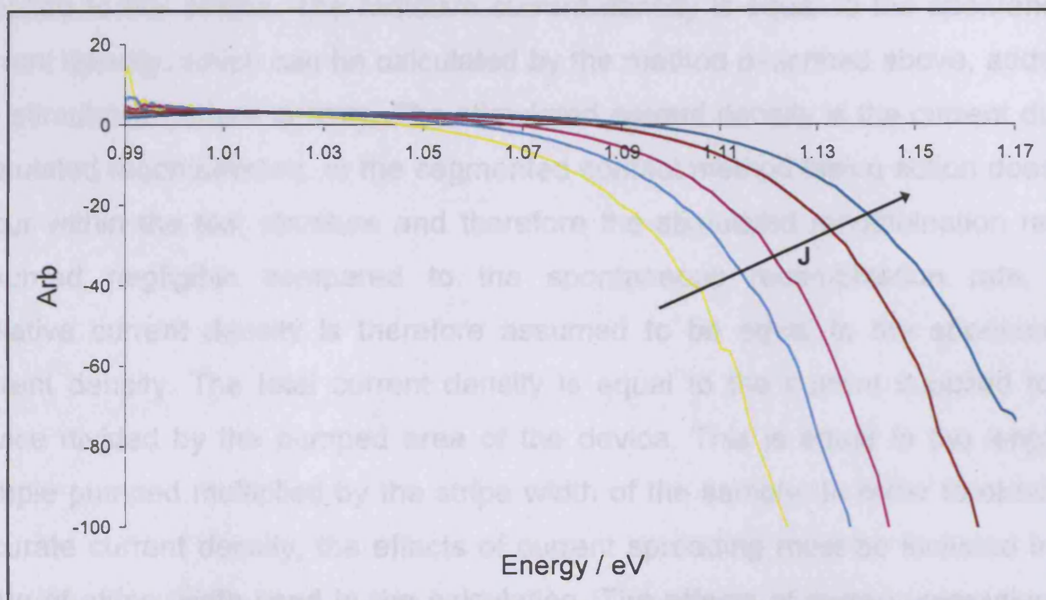

Figure 3.5 Example gain/measured spontaneous emission spectra for a InGaAs QW at 250K.

At low photon energy and high injection levels the system should be highly inverted, corresponding to P_f equal to 1. A region fitting these criteria can be identified within the plot of Figure 3.5, from approximately 0.99 to 1.03eV. Over this range the curves are approximately flat and of the same value, regardless of the current density the device is being driven at. By reading this value from the graph, the calibration constant can be calculated from Equation 3.11. The spontaneous emission can then be translated into real units by multiplying the spectra by this constant. Integrating these calibrated curves and multiplying by the electronic charge then produces the spontaneous current density by Equation 3.7.

The overall internal quantum efficiency is defined as:

$$\eta_i = \frac{J_{rad}}{J_{total}}$$

Equation 3.12

where J_{rad} is the radiative current density and J_{total} is the total drive current density supplied to the device. The radiative current density is equal to the spontaneous current density, which can be calculated by the method described above, added to the stimulated current density. The stimulated current density is the current due to stimulated recombination. In the segmented contact method lasing action does not occur within the test structure and therefore the stimulated recombination rate is assumed negligible compared to the spontaneous recombination rate. The radiative current density is therefore assumed to be equal to the spontaneous current density. The total current density is equal to the current supplied to the device divided by the pumped area of the device. This is equal to the length of sample pumped multiplied by the stripe width of the sample. In order to obtain an accurate current density, the effects of current spreading must be included in the value of stripe width used in the calculation. The effects of current spreading are discussed in Section 4.3.

It is important to understand that this is an overall efficiency, not a differential efficiency. The overall internal quantum efficiency is a fundamental efficiency equal to the number of photons that recombine radiatively within the sample compared to the number of electrons supplied to the sample.

3.4 Equipment Used for Segmented Contact method Experiments

The equipment used for these experiments consists of a number of optical components fixed to an optical bench and a system of electronics used to drive the device and record the light emission. This is shown in Figure 3.6. The measurement system is developed from that used by S Osborne [3.6]

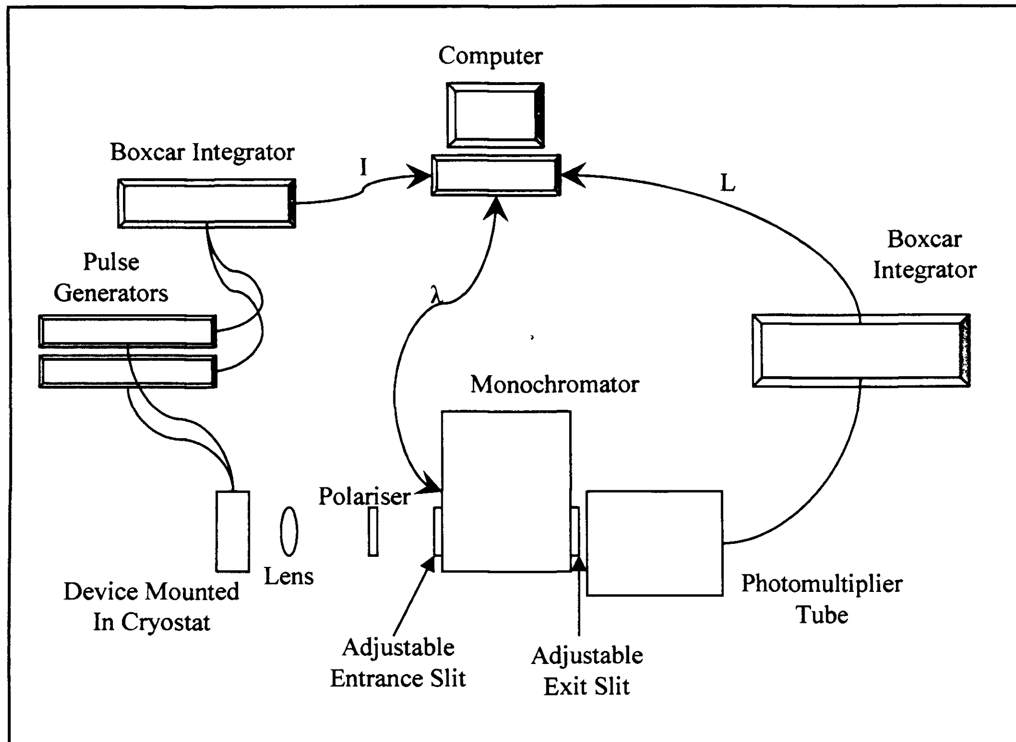

Figure 3.6 Equipment used for segmented contact experiments

The optical arrangement consists of the device, mounted in an Oxford Instruments Heliostat^{N} cryostat and a lens to focus light emitted from the device onto the entrance slit of a Bentham H300E monochromator. Before light enters the monochromator it passes through a polariser to allow measurement of TE or TM polarised light from the device. The light then enters the monochromator where a narrow wavelength band is selected before entering the photomultiplier tube (PMT) where it is detected. The PMT is a Hamamatsu R5509-42 and is inside a Products for Research cooled chamber where it is maintained at a constant temperature of -80°C, using liquid nitrogen. The voltage across the PMT is -1750V, provided by a Hamamatsu high voltage supply. The device is mounted within a cryostat to allow measurements to be made with the device at different temperatures. The cryostat is capable of producing temperatures as low as 77K using liquid nitrogen as the coolant. The device can also be heated to 400K using a heater mounted within the cryostat. According to the Oxford Instruments calibration of the cryostat it maintains temperatures at ±0.5K.

The two independently-contacted sections of the multi-segment sample are driven via two pulse generators (PG) whose outputs are connected to the device. Two PGs are necessary because the two ASE signals required for the experiment are measured nearly simultaneously. There is not sufficient time between the measurements to switch the supply of one PG between the sections. As these experiments are carried out pulsed, one pulse can be delivered to section 1, followed by a short delay before a second pulse is delivered to section 2, in the case of a loss measurement. For this work, the pulse length was 500ns with the delay between pulses approximately 2µs. The delay between pulses is larger than the pulse width to ensure the PG output has time to settle to zero between pulses. The pulse sequence is shown in Figure 3.7 below. The black lines represent the current pulse output from each PG, as would be viewed on a cathode ray oscilloscope (CRO). For clarity, the pulse driving section 2 has been shifted upwards relative to that driving section 1. The red and blue lines correspond to the boxcar integrator gates used to measure current and light respectively. These are discussed later in this section. This sequence of pulses is repeated at a repetition rate of 1 kHz to avoid heating effects.

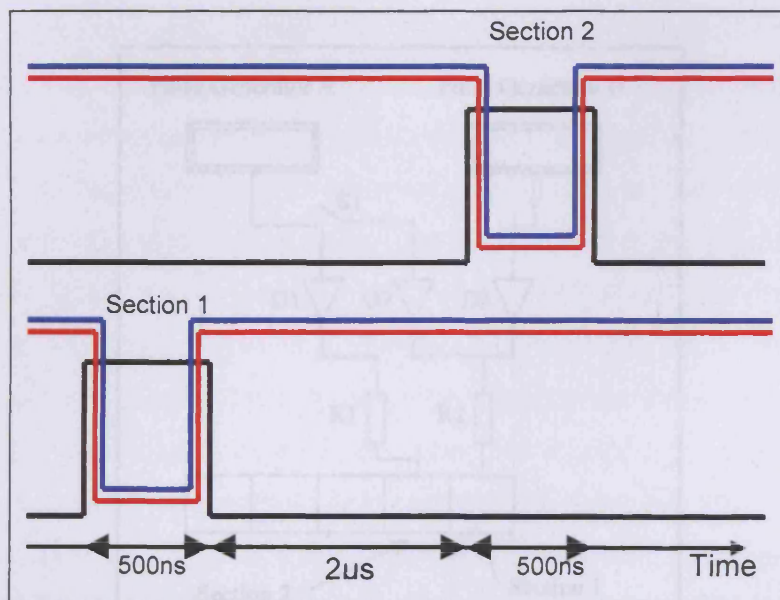

Figure 3.7 Pulse sequence used to drive device during a loss measurement shown in black. The red and blue lines show the gate positions of the boxcars used to measure current and light respectively.

The PGs are equipped with current transformers to sense and allow measurement of the output current. These circuits provide a pulsed voltage output where nominally an output of 1V corresponds to a current flow of 2A when connected to a 50Ω input impedance. This relationship allows the currents to be measured by displaying the outputs on a CRO and using the cursor facility to measure the voltage. However, in these experiments the pulsed current sensing output of each PG is fed into one channel of a two-channel boxcar integrator. Each channel of the boxcar has its gate positioned so that one channel measures current from PG A and the other current from PG B as shown in red in Figure 3.7. The boxcar integrator reads the voltage input to it within the location of the gate. It then compares this voltage to the average signal over all time and provides a DC output voltage. These are then collected by a computer equipped with an analogue to digital converter (ADC) card. The detail of the computer measurement is explained later in this chapter.

To ensure the PGs driving the device only supply current to the section they are required to, the outputs are connected to the device via the circuit shown in Figure 3.8

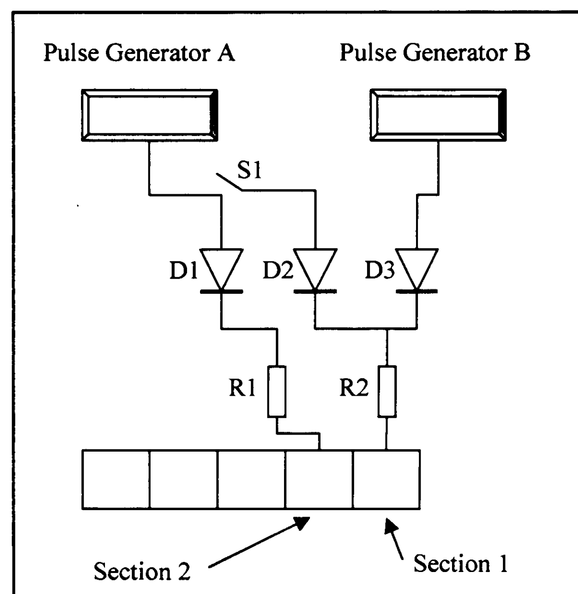

Figure 3.8 Circuit used to drive multi section device

The resistors R1 and R2 are 50Ω and are present in the circuit to reduce the effect of any difference in the I-V characteristic of the individual sections. Diode D3 prevents current from PG A flowing to ground through the output of PG B rather than flowing through section 1. Diode D2 has the same effect but when the pulse is output from PG B. Diode D1 is not required to prevent current flowing incorrectly but is included so that the circuit branches going to section 1 and section 2 are the same. Switch S1 controls whether current from PG A flows only to section 2, for a loss measurement, or to both section 1 and section 2, for a gain experiment. When driving sections 1 and 2 together, the current flows through an area of sample that is twice the area of section 1 or 2 alone. As a result, when measuring gain, the current from PG A must be double that of PG B. This is so that the current densities in the device sections are the same.

In addition to the electronics required to supply current to the device sections, there is a system for recording the two signals output by the PMT. The signal output by the PMT is a current. To be measured by a boxcar integrator and then a computer, this current must be converted to a voltage. This was achieved by passing the current through an impedance of 50Ω and measuring the voltage across this impedance. The impedance could have been either an adjustable resistor within the PMT itself that could be set to different values including open circuit and 50Ω, or the 50Ω input impedance of the pulse amplifier needed to increase the signal levels. The input impedance of the amplifier was chosen as, with the PMT resistor set to open circuit, there was a factor two increase in the voltage input to the amplifier. This factor two results from the current effectively passing through an impedance of 25Ω when the PMT resistor and amplifier input impedance are combined in parallel. Using the amplifier input impedance alone, the current flows through 50Ω so for the same current flow, twice the voltage is measured. The pulse amplifier is needed because the peak current flow from the PMT was typically 0.1mA. This corresponds to a voltage of 5mV. The pulse amplifier provides an amplification of a factor 100. This gave an output voltage of 0.5V, which is below the boxcars' maximum allowable input voltage of 1V. The PMT has an absolute

maximum limit for peak current of 2mA before it is irreversibly damaged. Using an amplification of factor 100 and adhering to the maximum input to the boxcar integrator of 1V ensured the current was never allowed to get within a factor 10 of this limit. The output from the amplifier was then split and fed into a boxcar where the gates were positioned as in the current measurement mentioned above. That is, with the gate for one channel positioned to measure light from section 1 and the other to measure light from section 2, in the case of a loss experiment. The boxcar outputs were then fed to the computer's ADC card.

The computer also contains an IEEE interface card so that it can communicate with the monochromator. The IEEE interface controls two stepper motors within the monochromator. One of these rotates the diffraction grating, adjusting the wavelength directed to the exit slit. The second motor rotates a filter wheel within the monochromator. Initially this feature was not utilised. Communication between computer and monochromator allows the computer to control the entire experiment. To begin, the diffraction grating within the monochromator is set to a start wavelength. The computer then collects and stores the voltage signals output from the boxcar channels connected to the PMT output. These signals are averaged repeatedly by the computer to reduce noise. Once the signals for the start wavelength have been collected, the computer moves the diffraction grating so that a different wavelength of light is incident on the PMT. This process is repeated to build up a complete spectrum until the desired stop wavelength is reached. The start and stop wavelengths, as well as the step size are set within the computer program by the user before the experiment begins. The computer program responsible for this was originally written by K Griffiths, [3.7] with modifications by S Osborne and C Dunscombe before the extensive additions and improvements made during this work.

3.5 Improvements Made to the Experimental Setup.

Whilst the equipment described above worked effectively, several modifications and improvements were completed at the start of this project. The most significant

being further automation of the system so that the experiment may be left to run unaided for extended periods of time. This requires that the currents be set by the computer and not the user. To achieve this, the PGs are controlled by digital outputs available on the ADC card. The computer can then step up or down the output of the PG. To set the current the PG output is increased by a single step and then the current measured. This sequence is repeated until the current is set to the required value. Using the computer to set the currents not only allows the equipment to run automatically but also enables a more accurate calibration of the current sensing circuits within the PGs. The nominal 2V equals 1A can be checked by setting a current using a calibrated current transformer. This is then measured by the computer. Repeating this for several currents, a calibration factor can be measured and stored in the computer. Having a separate calibration measured for each PG ensures that any differences in calibration are taken into account so the currents set will always be correct relative to each other. This is particularly important for the segmented contact method as the equations used to calculate loss, gain and spontaneous emission require that the current density in each section is identical. As well as offering this advantage, the computer also provides a more repeatable way of setting the currents.

The automation was further improved by allowing the computer to measure zero values for the light signals. To achieve this, a filter wheel containing a blanking plate was used. This is controlled by the computer software so that it is closed for the first and last points of the spectrum being measured. A straight line between these two points is then calculated and subtracted from the measured light signals. A separate zero is read for each boxcar channel. These zeroes remove any offsets within the electrical equipment as well as correcting for any drift that may occur. Initially, this automation distorted the results, causing the spectra to either become negative, or never reach a value of zero. After analysing these effects, it was established that the system was not being given enough time to settle to its true zero value. This was producing artificial zeroes, causing the results to be distorted. To cure this, the system is paused by the computer before each zero point is read,

allowing it to settle. As the accuracy of the zero points is especially important, the computer averages the zero points a factor of 10 times more than for the other data points. With the current setting and zeroing automated, the system is capable of running without the presence of the user. When starting the computer program, a list of currents is entered which the computer then sets, records the associated spectra and moves on to the next current. The currents can be set in any order so as to remove the possibility of patterns being introduced to the data set artificially.

In addition to the complete automation of the measurement system, other areas were also improved. To ensure accurate readings, the boxcar integrator used to measure light was swapped to four channels versus the two used previously. Two of the channels have their gates positioned to be after the two pulse sequence. They measure the output of the PMT when no light is incident on it. Subtracting one of these channel's outputs from each channel reading a light signal provides a further zero measurement for each data point. This subtraction takes place within the boxcar in real time, so no further connections to the computers ADC card are required.

The position of the optical components was optimised so that the light collected, from the guided modes in the device, by the PMT was maximised. These optimisations included moving the lens used to focus the device light onto the entrance slit further from the monochromator. This provides a tighter cone of light, maximising the amount of light incident on the detector. This is due to the relatively small dimensions of the PMT. Together with this the mount between monochromator and PMT cooler was redesigned to position the PMT as close as possible to the monochromator exit slit. A distance between lens and entrance slit of 275mm was found to be the optimum with the PMT in its revised position. Whilst these changes improve signal levels they could adversely affect the results by reducing the resolution the system is capable of. With a narrower cone of light entering the monochromator, fewer lines of the diffraction grating are illuminated. This reduces the resolution the grating is capable of. With the revised position of the lens the width of grating illuminated was 23.3mm. This gives a resolution limit

of 0.1nm. For the 300E, Bentham states a maximum resolution of 1.5nm. This number is much greater than that calculated with the grating only partially illuminated so the position of the lens should have little effect on the results due to the grating not being fully illuminated.

The resolution limit of the system is also affected by the width of the monochromator's entrance and exit slits. Wider slits are advantageous as they allow more light to be collected by the PMT. However, they must not be so wide as to change the result because of a change in resolution. The effect was investigated by measuring several net modal gain spectra with slit widths between 20 and 150μm. The results of this appear in Figure 3.9.

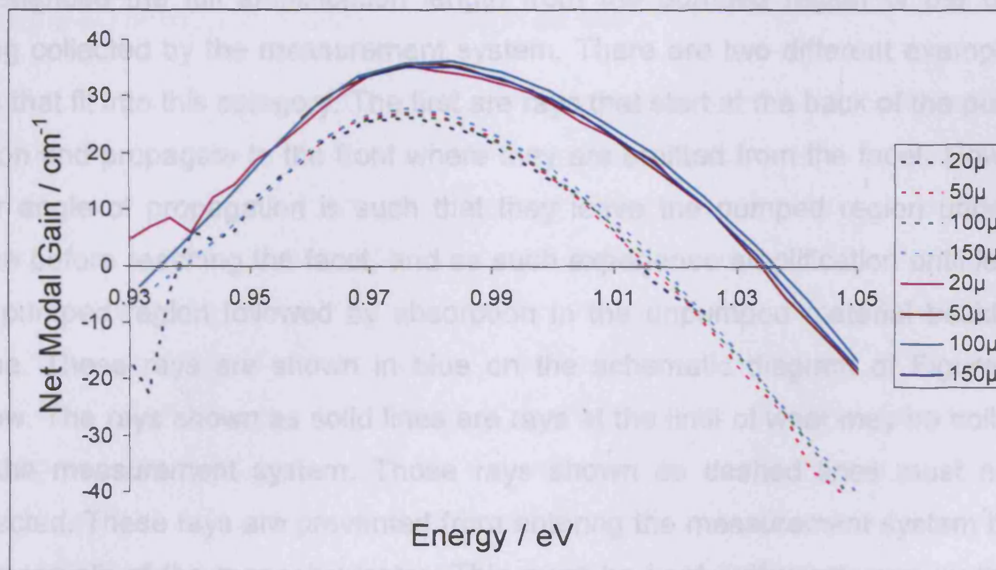

Figure 3.9 Net modal gain spectra for a range of slit widths and drive current densities of 1111 (dashed lines) and 1667Acm^{-2} (solid lines).

As can be seen from the figure, increasing the slit width from 20 to 150μm has no effect on the shape of the modal gain spectra. This implies that at 150μm or lower the slit width is not the limiting factor in determining the resolution of the system. This agrees with the resolution calculated from the dispersion of the monochromator's diffraction grating. The linear dispersion stated by Bentham is 5.4nm(mm)$^{-1}$ when using a 600lines(mm)$^{-1}$ grating. With slits 150μm wide, this

gives a resolution limit of 0.8nm. This is below the limit of 1.5nm quoted in the monochromator manual. All these results mean that the experiment will work accurately with slit widths up to 150μm and in theory larger. However, these wider slit widths are of no practical use because with the samples measured in this work the signal levels would become larger than the 1volt maximum input to the boxcar integrator.

The input optics, together with the monochromator's entrance slit also play another, important role. For the measurement of gain, loss and spontaneous emission to be accurate, the light which the system collects from the device must only include light from guided modes. This is to prevent rays of light that have not experienced the full amplification length from the pumped region of the device being collected by the measurement system. There are two different examples of rays that fit into this category. The first are rays that start at the back of the pumped region and propagate to the front where they are emitted from the facet. However, their angle of propagation is such that they leave the pumped region under the stripe before reaching the facet, and as such experience amplification until leaving the pumped region followed by absorption in the unpumped material beside the stripe. These rays are shown in blue on the schematic diagram of Figure 3.10 below. The rays shown as solid lines are rays at the limit of what may be collected by the measurement system. Those rays shown as dashed lines must not be collected. These rays are prevented from entering the measurement system by the entrance slit of the monochromator. This must be kept sufficiently narrow to only permit the collection of light from within the width of the stripe. With the optics positioned as they are, the magnification provided by the lens is 8.8. This lens images the stripe onto the entrance slit. Therefore the widest entrance slit that can be used for a 50micron stripe geometry sample is 440μm. This is much wider than any of the slit widths used to check the resolution of the system in Figure 3.9 above and as such this does not present any problem to the measurements when a slit width of 150μm or less is used.

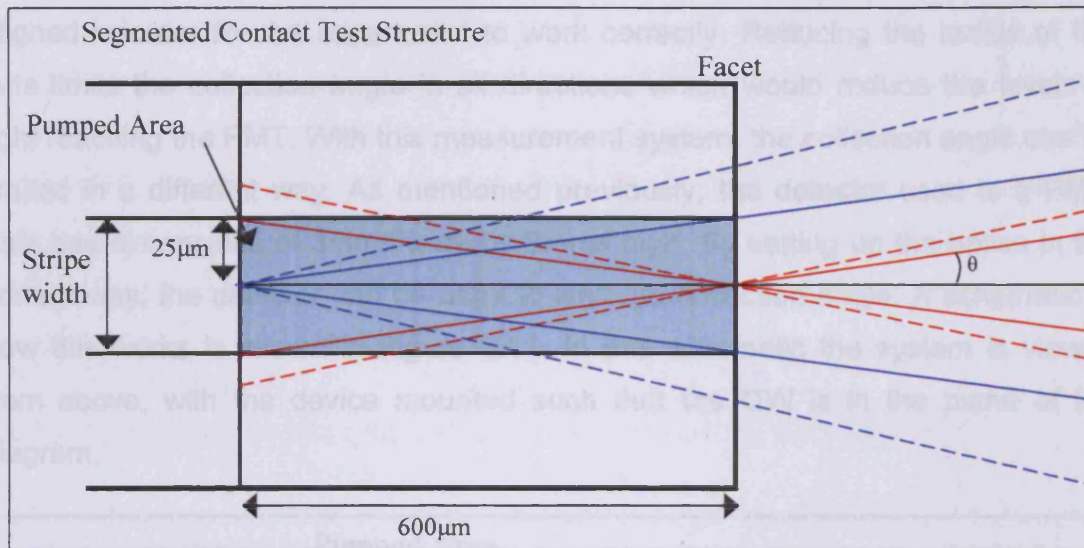

Figure 3.10 light rays emitted from test structure that should (solid lines) and should not (dashed lines) be collected by the measurement system

The second category of ray that must not be collected are shown in red in Figure 3.10 above. They are emitted from the facet of the device within the width of the pumped stripe, but also have not experienced the full amplification length. The entrance slit of the monochromator does not prevent these rays from entering the monochromator. To prevent them from changing the results of the experiment, the angle from which light from the device is collected must be limited. That is it must be limited to θ degrees or less in the diagram above. This fact was first investigated for optical pumping by Cross and Oldham [3.9] and in detail for electrically injected samples by Lutti [3.10]. This angle is smallest when pumping sections 1 and 2 together. As such, the limiting angle must be calculated for a length of 600µm for the samples measured in this work. With half the stripe width equal to 25µm, this gives an angle within the device of 2.4^0. Taking into account the refraction experienced by the light as it passes from semiconductor to air, gives θ equal to 7.8^0. For clarity, the diagram above does not show the refraction of the light rays leaving the facet. The collection angle can be limited by reducing the aperture of the lens shown in Figure 3.11. This can be achieved by using a smaller radius lens, or by introducing a slit between the test structure and the lens. However, using a slit introduces another component which must be precisely

aligned in order for the experiment to work correctly. Reducing the radius of the lens limits the collection angle in all directions which would reduce the levels of light reaching the PMT. With this measurement system, the collection angle can be limited in a different way. As mentioned previously, the detector used is a PMT. This has dimensions of 3mms wide by 8mms high. By setting up the optics in the correct way, the detector can be used to limit the collection angle. A schematic of how this works is shown in Figure 3.11. In this schematic the system is viewed from above, with the device mounted such that the QW is in the plane of the diagram.

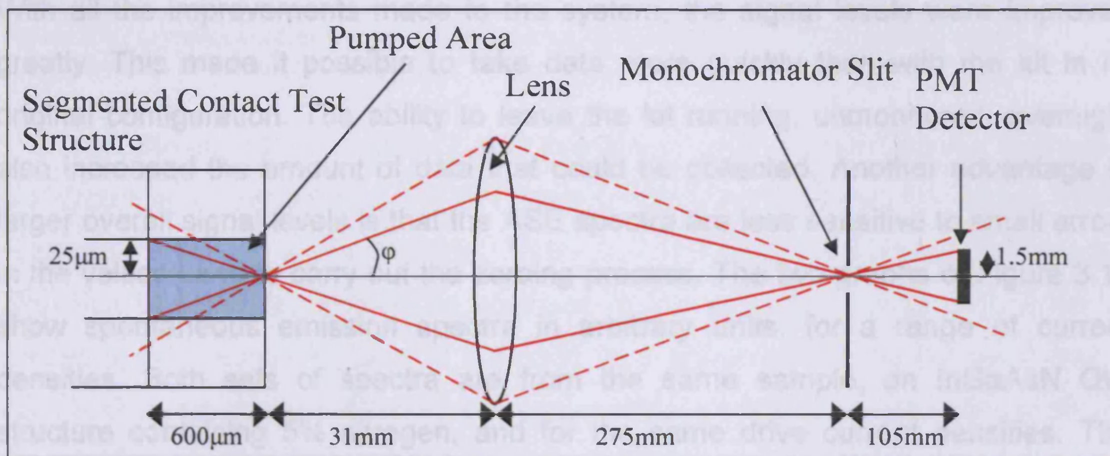

Figure 3.11 schematic diagram showing geometry of light measurement and how collection angle is limited

As in Figure 3.10 example light rays that can be collected are shown in solid red whilst example rays that must not be collected are illustrated by dashed red lines. Again, the refraction experienced by the rays as they exit the facet has been omitted from the diagram for clarity. The monochromator is shown in the diagram as a single slit, because aside from splitting the light into separate wavelength bands, it does not affect the light rays. As the solid red lines show, the small detector size has the effect of reducing the radius of the lens. With a detector height of 1.5mm and the distances between detector, monochromator and lens shown above the lens radius is effectively reduced to 3.9mm in the horizontal plane. With the lens positioned 31mm from the device, the angle from which light is

collected, φ is 7.2^0. This falls below the limit of 7.8^0 calculated above. Therefore the detector limits the collection angle of the system without introducing any extra components. In addition, with the dimensions shown above, the vertical collection angle is 18.7^0 providing much greater signal levels than if a smaller aperture lens were used. It is important to note that the limits set on the collection of light do not apply in the vertical direction. This is because the light is guided by the device structure in the plane 90^0 to the QW plane.

3.6 Confirmation that equipment is operating as required

With all the improvements made to the system, the signal levels were improved greatly. This made it possible to take data more quickly than with the kit in its original configuration. The ability to leave the kit running, unmonitored, overnight also increased the amount of data that could be collected. Another advantage of larger overall signal levels is that the ASE spectra are less sensitive to small errors in the values used to carry out the zeroing process. The two graphs of Figure 3.12 show spontaneous emission spectra in arbitrary units, for a range of current densities. Both sets of spectra are from the same sample, an InGaAsN QW structure containing 5% nitrogen, and for the same drive current densities. The graph to the left shows data collected with the equipment in its original configuration, but with the computer controlling the zeroing of the ASE spectra. The graph to the right shows spectra collected after the improvements made to the optical arrangement, current setting and zero measurement were completed.

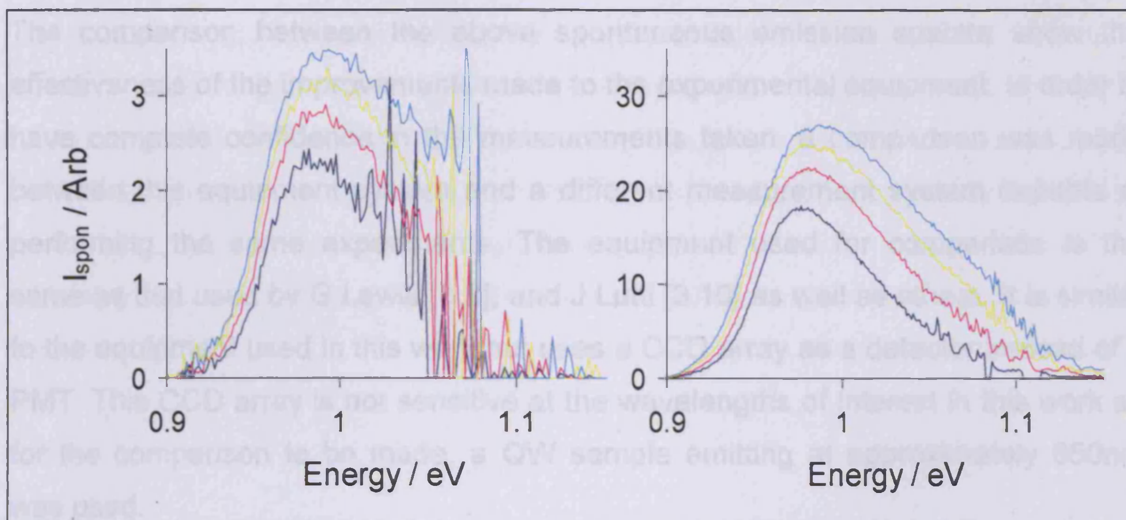

Figure 3.12 uncalibrated spontaneous emission spectra measured before and after improvements to kit were completed

The first difference to note about these two plots is that the right hand y axis scale is a factor of ten larger than the left hand scale. This illustrates the improvement achieved in terms of signal strength. These two sets of spectra clearly illustrate the reduction in noise levels that the changes to the equipment produced. There is noticeably less scatter present in the right hand graph versus the left hand graph, even taking into account the different scales. The left hand plot also clearly shows the problems associated with the ASE spectra being inaccurately zeroed, or the currents being set inaccurately. At high photon energy, the spontaneous emission spectra show large spikes and then an abrupt drop to zero, at a lower energy than may be expected. This effect is produced by the ASE spectra measured from section 1 having a larger value at a given photon energy than that measured from sections 1 and 2 together. This could be caused by the zeroing of the ASE signals being incorrect or by the current density in section 1 being higher relative to that in sections 1 and 2. The spectra in the right hand graph do not display these effects. The changes made to the way the zeroes are measured as well as having the computer set the currents have solved these problems. However, the spectra are still noticeably noisier at high photon energy, showing how sensitive the values in this region are to small errors or fluctuations in the measured ASE signals.

The comparison between the above spontaneous emission spectra show the effectiveness of the improvements made to the experimental equipment. In order to have complete confidence in the measurements taken, a comparison was made between this equipment system and a different measurement system capable of performing the same experiments. The equipment used for comparison is the same as that used by G Lewis [3.8], and J Lutti [3.10] as well as others. It is similar to the equipment used in this work but uses a CCD array as a detector instead of a PMT. This CCD array is not sensitive at the wavelengths of interest in this work so for the comparison to be made, a QW sample emitting at approximately 650nm was used.

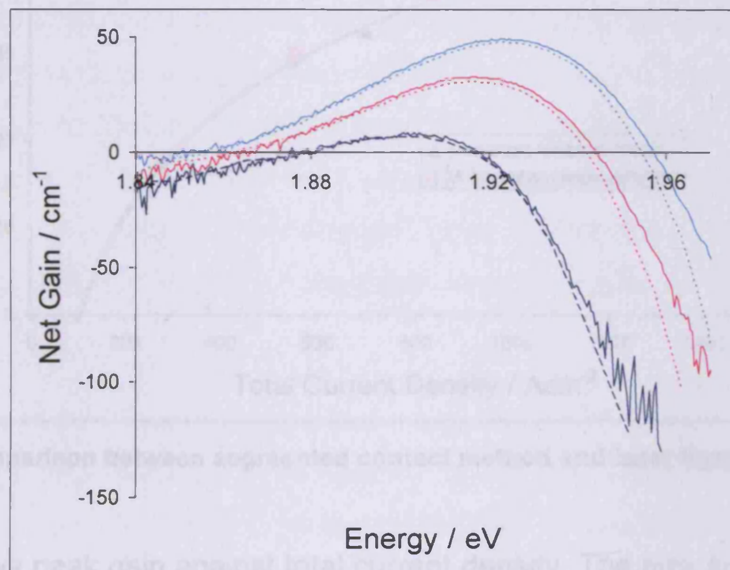

Figure 3.13 Comparison of data collected with equipment used for this work and CCD kit. The dashed lines are data measured with the equipment used in this work, the solid lines are data collected with the CCD kit.

The dashed lines in Figure 3.13 are net gain spectra measured at three different current densities, with the equipment system used for this work. The solid lines are spectra at the same three current densities measured with the assistance of G Lewis on the CCD based system. The figure clearly shows good agreement between both sets of equipment and therefore shows the equipment used for this work is working correctly.

The above comparison shows that the equipment and experimental method used is working correctly when compared to an experiment of the same type using a different set of measuring equipment. To further check the operation of the equipment used in this work and to check the technique as a whole is working correctly, a second comparison was made. This takes data obtained using the segmented contact method and compares it with laser threshold current density measurements.

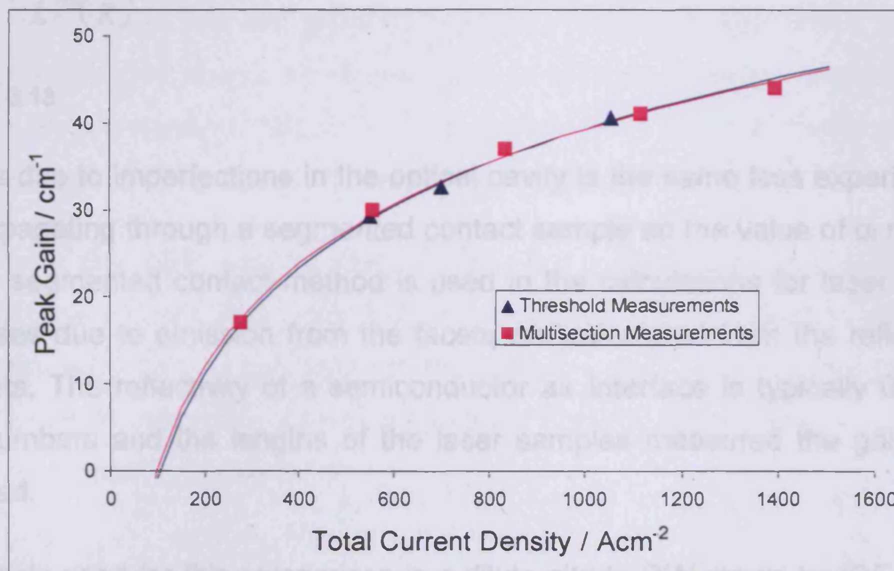

Figure 3.14 comparison between segmented contact method and laser threshold measurements

This plot shows peak gain against total current density. The pink squares in Figure 3.14 are points taken from data collected with the segmented contact method and the blue triangles are laser threshold data. In both cases, the total current density was calculated by dividing the current driving the sample by the pumped area of the sample. This is discussed previously for the segmented contact test structure. For a laser sample the area used in the calculation is the stripe width multiplied by the length of the laser sample. The different current densities shown in Figure 3.14 are measured by changing the drive current in the segmented contact experiment and by using different length lasers in the case of threshold measurements. For the segmented contact work, the values of peak gain plotted above are the peak

values of the net gain spectra for each current density, with the value of α_i added to these peak values. This is discussed further in Chapter 4. Calculating peak gain values from laser measurements is more complicated. In a laser, at threshold, the gain matches the losses. Thus, the peak gain for a laser sample is the gain at threshold. The threshold gain for a laser can be calculated from Equation 2.1, repeated here for convenience.

$$G_{th} = \alpha_i + \frac{1}{L}\ln\left(\frac{1}{R}\right)$$

Equation 3.13

The loss due to imperfections in the optical cavity is the same loss experienced by light propagating through a segmented contact sample so the value of α_i measured with the segmented contact method is used in the calculations for laser samples. The losses due to emission from the facets are calculated from the reflectivity of the facets. The reflectivity of a semiconductor air interface is typically 0.3. Using these numbers and the lengths of the laser samples measured the gain can be calculated.

The sample used for this comparison is a dilute nitride QW grown by IQE. It is one of the samples measured by M Al-Ghamdi during his Mphil studies. The laser threshold data shown in Figure 3.14 was measured by M Al-Ghamdi and is taken from his thesis [3.11].

The figure shows excellent agreement between the two measurement techniques, providing real confidence in data collected using the segmented contact method and the equipment system described above.

3.7 Estimating errors in the experimental measurements

The estimation of errors is very important in any experimental measurement. Knowledge of the errors involved shows the accuracy and precision of an experiment. The treatment of errors in this work is especially important because

the technique is complex and it would be easy to over interpret the measurements. The data produced using the segmented contact method can also be compared to theory. To do this, knowledge of the errors associated with the experiment is vital. Without this, it is impossible to say whether experiment agrees with theory.

In this work, a thorough error analysis is carried out on all the data collected. This begins with estimating the error associated with each point in an ASE spectrum. For the ASE data in this work, the most significant source of error is that due to variation in the start and end zero data points. There are also errors associated with each ASE point due to small inaccuracies in current setting and noise in the electrical system used to collect the light signals. The effect of these errors was estimated to be an error bar of ±1% on each point in an ASE spectrum.

The error in the ASE spectra due to the zero value used was estimated by calculating the difference in start and end zero points for a selection of the ASE data measured. The average variation between the start and end zero points was used as the error estimate in zeroing the data. The variation in start and end zero points is illustrated in Figure 3.15.

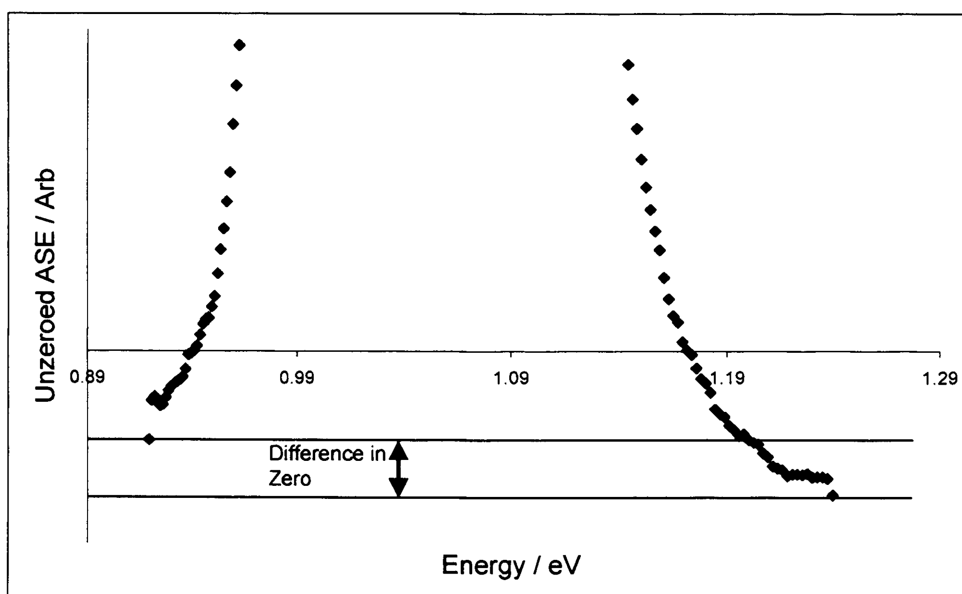

Figure 3.15 Example of difference in start and end zero points for ASE data (symbols) from and InGaAs QW at 300K.

To give the error bar for each data point in an ASE spectrum, the errors in current and zero were combined using Equation 3.14. If a quantity y is calculated from quantities a and b, then the error in y can be calculated from the errors in a and b using [3.12]:

$$E^2(y) = \left\{\frac{\partial y}{\partial a}\right\}^2 E^2(a) + \left\{\frac{\partial y}{\partial b}\right\}^2 E^2(b) + \cdots$$

Equation 3.14

It is also necessary to plot error bars on loss, net modal gain, spontaneous emission and inversion factor spectra. To do this, the errors in each ASE signal, and any other associated error must be combined using Equation 3.14. The equation was applied to calculate the errors in net modal gain and spontaneous emission spectra from the errors in ASE signals $I_{ASE}(1)$ and $I_{ASE}(1,2)$. Similarly, the error in loss spectra was calculated by combining errors in $I_{ASE}(1)$ and $I_{ASE}(2)$. To calculate the error in the inversion factor plots, the errors in net modal gain and spontaneous emission are combined, the estimated error in the value of α_i is also included. This is necessary because to calculate the inversion factor from the experimental data, the value of α_i determined from net modal absorption and gain spectra must be added to the net modal gain spectra before dividing by the measured spontaneous spectra. Therefore any error introduced in the choice of α_i will contribute to the error in inversion factor, so this must be included in the error analysis. The error combinations are carried out on each point of each spectrum. Treating the errors in this way produces error bars that clearly show which regions of the spectra should be used for further analysis. Regions that should be treated with care are also made clear by the relatively large error associated with them. All of the error bars shown on ASE, net modal gain, spontaneous emission rate, net modal absorption and inversion factor spectra in the following chapters were calculated in this way.

3.8 References

3.1 B. W. Hakki, T. L. Paoli, *J Appl Phys*, **70** (1975) 1299

3.2 K L Shaklee and R F Leheny, Appl Phys Letts, **46** (1971) 475

3.3 A Oster, G Herbert and H Wenzel, Electronics Letters, **33** (1997) 864

3.4 J D Thomson, H D Summers, P J Hulyer, P M Smowton and P Blood, Appl Phys Letts **75** (1999) 2527

3.5 P. Blood, G. M. Lewis, P. M. Smowton, H. Summers, J. Thomson, J. Lutti, *IEEE J. Select Topics Quantum Electron.*, **9** (2003) 1275

3.6 S. Osborne, PhD, (2004), Cardiff University

3.7 K. Griffiths, M. Phil (1992) University of Wales, Cardiff

3.8 G. M. Lewis, PhD (2002), University of Wales, Cardiff

3.9 P. S. Cross, W. G. Oldham, *IEEE J Quan Elec*, **11**, (1975) 190

3.10 J Lutti, PhD, (2005), Cardiff University

3.11 M Al-Ghamdi, Mphil (2005), Cardiff University

3.12 First year lab notebook, Cardifff University

Chapter 4 The Effect of Nitrogen in the InGaAsN QW

4.1 Introduction

In this chapter, the effect of increasing nitrogen in the InGaAsN QW is investigated. To examine the effects of increasing nitrogen, the net modal absorption, net modal gain and spontaneous emission rate spectra were measured for three samples with QW nitrogen compositions of 0, 0.5 and 0.8%. The spectra were measured using the segmented contact method. Each sample's spectra were measured at temperatures of 300K, 250K and 200K. Conclusions are drawn by comparing the measured spectra for the three samples at each temperature. Comparisons are also made between characteristics for the different samples' peak modal gain as a function of total and radiative current density. Finally the overall quantum efficiency is computed and compared for each sample and temperature.

4.2 Details of Structures Measured

In this section of work, the effect of introducing nitrogen to the InGaAsN QW was examined. Measurements were carried out for a range of current densities and temperatures, on three different laser structure samples. All three structures consisted of a single QW, with the only difference between the three samples being the composition of the QW. A schematic diagram of the structure is shown in Figure 4.1. The structures were grown by low pressure Metal-organic Chemical Vapour Deposition (MOCVD) at the University of Madison, Wisconsin and details of growth are given in [4.1]

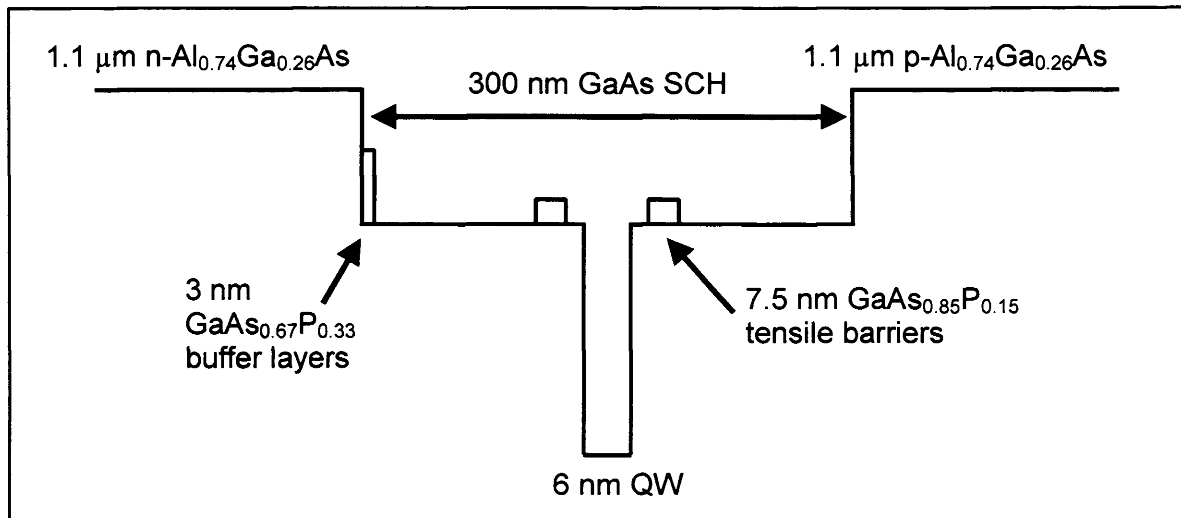

Figure 4.1 Schematic diagram of the band gap of the structures studied to examine the effect of nitrogen on the InGaAsN QW.

The design of these samples follows the technique of Sato et al [4.2]. This utilises a very high indium content in the quantum well so that a very small concentration of nitrogen is required to extend the emission wavelength to the 1.3μm region. For all three samples the indium content is 40%. The nitrogen content is different in each sample and is 0%, 0.5% or 0.8%. The QW is embedded in a 300nm separate confinement heterostructure (SCH). Because of the very high indium concentration, the QWs are highly compressively strained. The compressive strain in each sample was calculated to be 2.79%, 2.69% and 2.64% for the samples containing 0%, 0.5% and 0.8% nitrogen respectively [4.3]. Because the calculated strain in each of these structures is so similar, it is not expected that the different strains will have any significantly different effect on the optical properties of the samples. To allow high quality crystal growth with the highly strained QW, 7.5nm GaAsP tensile strained barrier layers are needed. These are positioned on either side of the QW with a 10nm GaAs spacer layer between the barrier and well. There is an additional GaAsP buffer layer grown on top of the GaAs waveguide to provide a good quality interface between the waveguide and n type AlGaAs. No post - growth annealing was used in these samples. Laser devices processed from these wafers were measured by Tansu et al in [4.1,4.3,4.4]. These wafers were

processed into multisection samples at Cardiff University by P Hulyer and cleaved into individual chips by J Thomson and I Pope. The devices were mounted onto standard 3 pin TO5 headers allowing independent contacts to section 1, section 2 and ground. Facilitating current supply to section 1 and section 2 as described in section 3.4.

4.3 Requirements for a sample suitable for multisection measurements

Whilst mounting the samples on headers was the only step needed to measure them, there are several characteristics of each sample that must meet certain criteria before measurement with the segmented contact method. To ensure electrical isolation between the sections of the samples, the resistance between section 1 and section 2 was measured. The resistances measured in this work ranged from 90 to 300Ω. These resistances are much higher than the resistance associated with the diode of the device in forward bias. The current–voltage characteristics (I-Vs) of section 1 and section 2 were also measured. This was done to make sure the current density in each section was equal when driving section1 and 2 together. If the I-Vs are significantly different, different currents will flow through section 1 and section 2. This is due to the pulse generator supplying a constant voltage. An example I-V from one of the samples measured is shown in Figure 4.2. As discussed in section 3.4 the device sections are not connected directly to the pulse generator outputs, but via the circuit of Figure 3.8. The inclusion of 50Ω resistors in series with section 1 and section 2 reduces the effect of any difference in the I-V characteristics. Figure 4.2 also shows the effect of measuring the I-V including the circuit of Figure 3.8. This shows the importance of including the circuit in the measurement of I-Vs. Devices may be rejected as being unsuitable for measurement when in fact they will provide accurate results. For this work devices whose I-Vs differed by greater than 1% with the current drive circuit included were not used in the experiments.

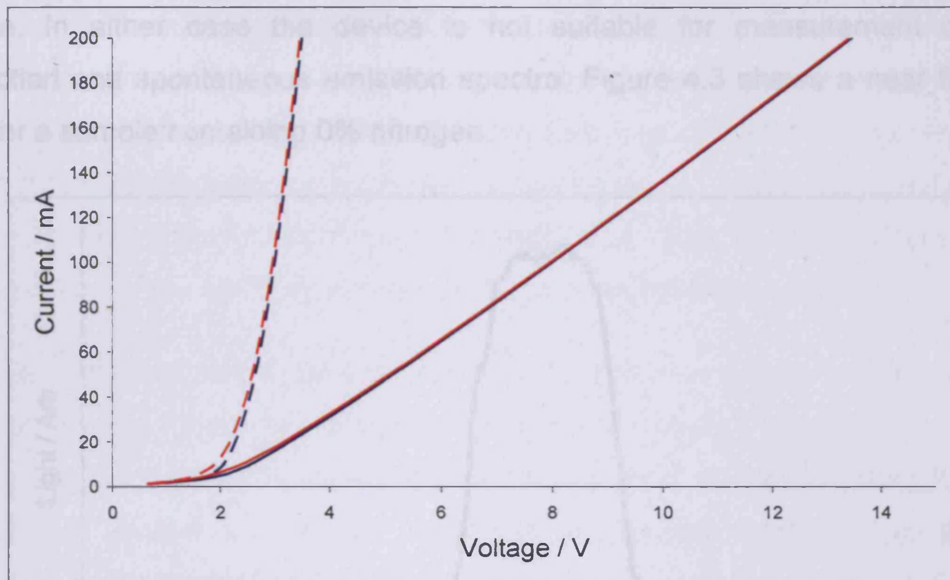

Figure 4.2 I-V characteristic for sample with 0.8% nitrogen measured for section 1 (red lines) and section 2 (blue lines) with (solid lines) and without (dashed lines) the inclusion of 50Ω resistors.

As can be seen in Figure 4.2, there is a small difference in the I-V characteristics for sections 1 and 2. This becomes much smaller when the effect of the 50Ω resistors in the drive circuit is included in the I-V measurement. With the 50 Ω resistors included, the difference between plots is reduced. There is a difference greater than 1% at low currents, below approximately 20mA. However, this is not a problem because the lowest current used in the experiment for the sample above was 40mA.

In addition to the electrical characteristics required of a sample as described above, the optical properties must be examined. To ensure an accurate experiment, the near field produced by a sample must be the same when driving section 1, section 2 or both together. The near fields were measured for each device and compared when driving section 1, section 2 and both together. The overall shape of the near field is also important, a smooth curve is desirable, as it implies the device is behaving uniformly across the width of the stripe. Any peaks or dips in the near field could indicate non - uniformity in the behaviour of the device across the stripe width. This could also indicate damage to the facet of the

sample. In either case the device is not suitable for measurement of gain, absorption and spontaneous emission spectra. Figure 4.3 shows a near field line scan for a sample containing 0% nitrogen.

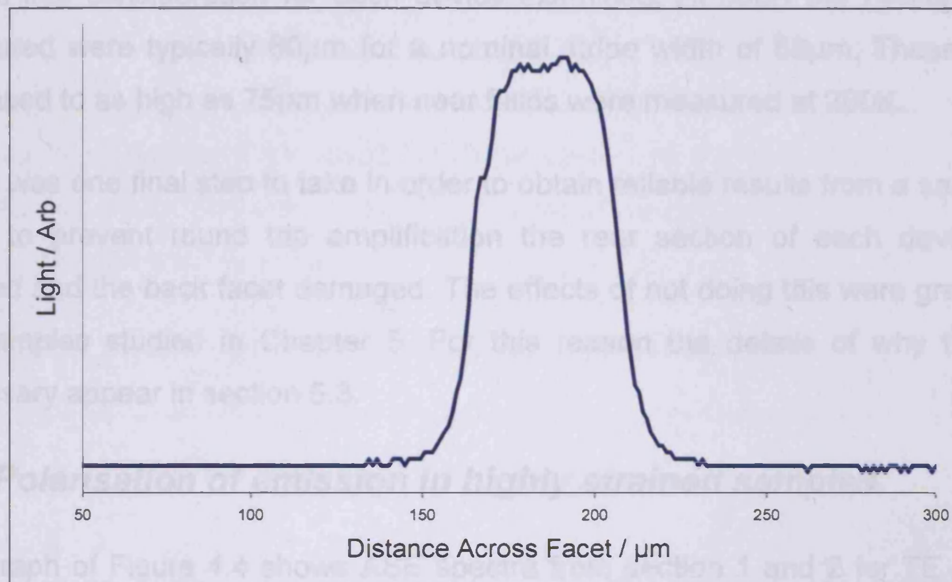

Figure 4.3 Near field line scan for device with 0% nitrogen when driving sections 1 and 2.

The near fields were measured using an InGaAs photodiode array camera sensitive at the wavelengths emitted by these samples. The near field was imaged onto the camera using a microscope objective lens. By imaging the end of the device, using an external light source and measuring the width of the chip itself in pixels, the x-axis of Figure 4.3 was calibrated. This was possible because the devices used in this work were all cleaved to be 300μm wide. This calibration was done separately for each sample measured to remove any changes introduced by different collection geometries. This measurement made it possible to estimate the effect of current spreading within each device. As mentioned in section 3.3.4 any current spreading effects must be taken into consideration. If they are not, the area of sample used to calculate the total current density supplied to the device will be incorrect. This would make comparisons between different samples impossible to do accurately and cause the measured internal quantum efficiency to be incorrectly calculated. In this work, the width of stripe being pumped was taken to be the full

width at half maximum (FWHM) value of the near field line scans measured for each device. This was the value used to calculate total current density. Using this method provided a mathematical and repeatable way of taking current spreading effects into consideration for each device examined. At 300K the FWHM values measured were typically 60μm for a nominal stripe width of 50μm. These values increased to as high as 75μm when near fields were measured at 200K.

There was one final step to take in order to obtain reliable results from a sample. In order to prevent round trip amplification the rear section of each device was earthed and the back facet damaged. The effects of not doing this were greatest in the samples studied in Chapter 5. For this reason the details of why this was necessary appear in section 5.3.

4.4 Polarisation of emission in highly strained samples.

The graph of Figure 4.4 shows ASE spectra from section 1 and 2 for TE and TM polarisations. For comparison, the TM spectrum has been multiplied by a factor 25.

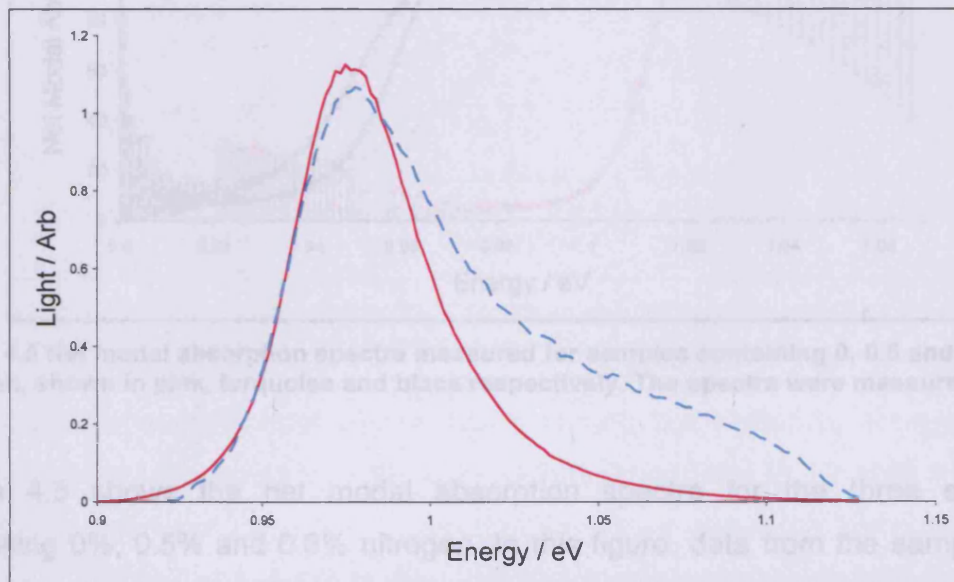

Figure 4.4 TE (solid lines) and TM (dashed lines) ASE spectra for device with 0.5% nitrogen measured at 300K. The TM Spectrum has been multiplied by 25.

Taking the factor 25 into account, the TM emission is significantly smaller than the TE emission at the same current density. The peak in the TM data below 1eV is due to emission in the TE polarisation that has not been fully blocked by the polariser used in the experiment. When orientated to measure TM light emission, the polariser in the optical path blocks >98% of the light emitted in the TE polarisation. It must be concluded that emission into the TM polarisation in these samples is negligible. This result confirms what was expected due to the high compressive strain present in the QW. All results presented in this work are for light polarised in the TE_y plane.

4.5 Effect of Nitrogen on Modal Absorption Spectra

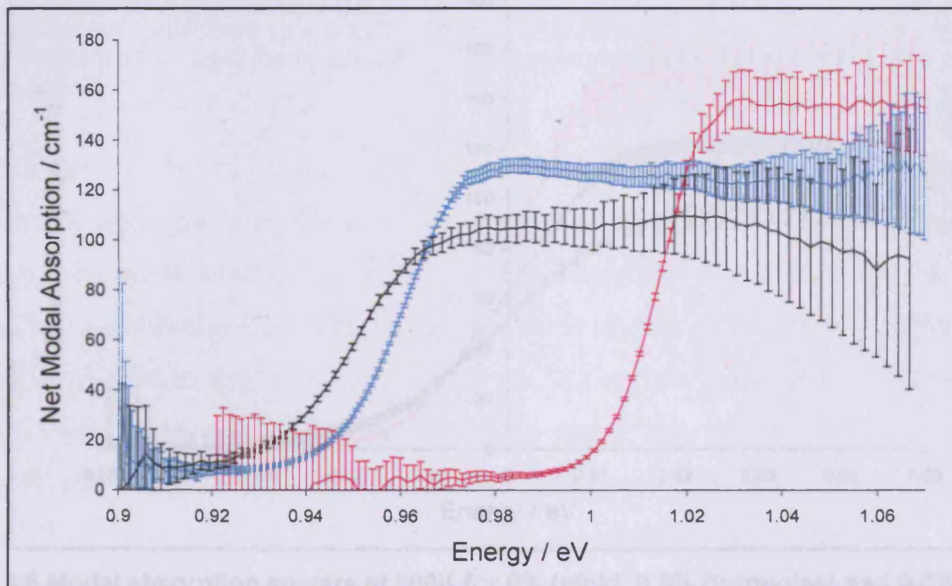

Figure 4.5 Net modal absorption spectra measured for samples containing 0, 0.5 and 0.8% nitrogen, shown in pink, turquoise and black respectively. The spectra were measured at 300K

Figure 4.5 shows the net modal absorption spectra for the three samples containing 0%, 0.5% and 0.8% nitrogen. In this figure, data from the sample with 0% nitrogen is shown in pink, data from the sample with 0.5% nitrogen is shown in turquoise and the data in black is from the sample with 0.8% nitrogen. This same colour scheme will be used throughout this chapter. From these plots and the net modal gain spectra shown later, α_i was determined to be $7\pm2cm^{-1}$ for all three

samples. This value was measured from the regions at low energy where the net modal absorption (and net modal gain) curves tend to the same constant value. The results are in agreement with the value of $6cm^{-1}$ obtained by Tansu et al [4.4] from external differential efficiency versus inverse cavity length laser data. No change in α_i was observed when the temperature of the samples was reduced to 250 or 200K. The inclusion of nitrogen in the InGaAs QW shifts the measured modal absorption spectra to lower photon energy. To examine the spectra more closely, the spectra were shifted in energy by the half height energy of the modal absorption spectra, after α_i had been subtracted from the data. These values of energy correspond to the bandgap for each sample.

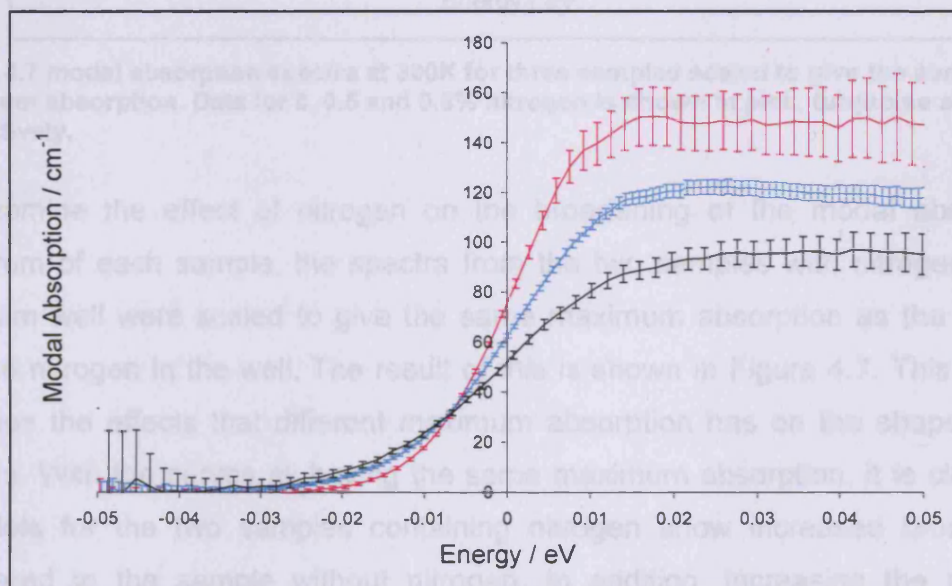

Figure 4.6 Modal absorption spectra at 300K for 0% (pink), 0.5% (turquoise) and 0.8% (black) nitrogen content in the QW, shifted by bandgap energy of each sample.

In Figure 4.6, the data from Figure 4.5 is shown, but shifted in energy by the bandgap energy measured from the original data. In addition to the shift, the mode loss, α_i has been subtracted. The colour of each data set is the same as that in Figure 4.5. Whilst it was visible in the original plot, this graph clearly shows that the inclusion of nitrogen in the QW affects the maximum absorption measured from each sample. Increasing the nitrogen concentration reduces the maximum absorption.

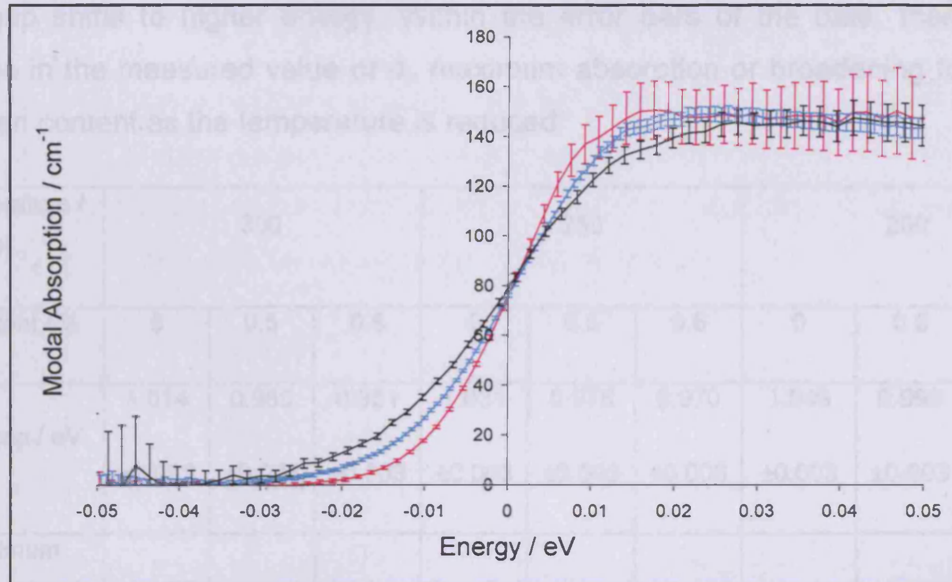

Figure 4.7 modal absorption spectra at 300K for three samples scaled to give the same maximum absorption. Data for 0, 0.5 and 0.8% nitrogen is shown in pink, turquoise and black respectively.

To examine the effect of nitrogen on the broadening of the modal absorption spectrum of each sample, the spectra from the two samples with nitrogen in the quantum well were scaled to give the same maximum absorption as the sample with no nitrogen in the well. The result of this is shown in Figure 4.7. This scaling removes the effects that different maximum absorption has on the shape of the spectra. With the curves all having the same maximum absorption, it is clear that the plots for the two samples containing nitrogen show increased broadening compared to the sample without nitrogen. In addition, increasing the nitrogen concentration from 0.5% to 0.8%, leads to a further increase in spectral broadening. The spectral broadening was estimated by measuring the energy shift between one quarter and three quarters of the maximum absorption. The values of broadening for all samples and temperatures appear in Table 4.1. The table also shows the measured values of the bandgap energy and maximum absorption for the three samples at temperatures of 300, 250 and 200K. For the two samples containing nitrogen, the table also includes the scaling factor the absorption spectra must be multiplied by to produce the same maximum absorption as the sample without nitrogen. As the temperature of the sample is reduced, the

bandgap shifts to higher energy. Within the error bars of the data, there is no change in the measured value of α_i, maximum absorption or broadening for given nitrogen content as the temperature is reduced.

Temperature / K	300			250			200		
N content / %	0	0.5	0.8	0	0.5	0.8	0	0.5	0.8
Bandgap / eV	1.014 ±0.003	0.960 ±0.003	0.951 ±0.003	1.031 ±0.003	0.978 ±0.003	0.970 ±0.003	1.049 ±0.003	0.999 ±0.003	0.986 ±0.003
Maximum Absorption / cm^{-1}	150±5	125±5	97±5	150±5	127±5	103±5	140±10	123±5	98±5
Broadening / meV	10±1	13±1	18±1	10±1	12±1	16±1	10±1	13±1	16±1
Scaling to match Peak Absorption Of 0% N		1.23	1.55		1.2	1.45		1.1	1.4

Table 4.1 Quantities measured from modal absorption spectra for samples with 0, 0.5 and 0.8% nitrogen and temperatures of 300, 250 and 200K.

The only quantity that appears to vary as the temperature is reduced is the maximum absorption for the sample with 0% nitrogen at 200K. Despite this apparent discrepancy, the value of 150cm^{-1} measured at 300K and 250K falls within the error bars on the modal absorption spectra measured at 200K for the sample with 0% nitrogen. The error bars in this plot are substantially larger than for the other temperatures, indicating that signal levels may have been too low during this measurement.

4.5.1 Interpretation of Modal Absorption Results

The absorption produced by a quantum well for a single pair of subbands is given by Equation 2.22 from section 2.3.6. In the case of an absorption measurement the occupation of conduction band states (f_c) is 0 and the occupation of valence band states (f_v) is 1. This gives an equation for modal absorption:

$$A(\hbar\omega) = -G(\hbar\omega) = \frac{4\pi\hbar}{nc\varepsilon_0(\hbar\omega)}\left(\frac{e}{2m_0}\right)^2 |M|^2 \left\{\int F_v^*(z)F_c(z)dz\right\}^2 \rho_r(h\nu)\frac{\Gamma}{L_z}$$

Equation 4.1

For the three samples studied here, the well width is constant and the confinement factor is 1.7% [4.3].

It has been reported in the literature [4.5,4.6] that increasing the nitrogen concentration in the InGaAsN QW reduces the matrix element, $|M|^2$ in the above equation. This reduction would bring about the reduction in maximum absorption observed in Figure 4.6. However, increasing nitrogen in the QW has also been reported to increase the conduction band effective mass and reduce the valence band effective mass [4.6,4.7,4.8,4.9]. The increase in conduction band effective mass is much greater than the reduction in valence band mass [4.10,4.11], sufficiently so that the reduction in valence band effective mass has almost no effect on the reduced mass used to calculate the reduced density of states in Equation 4.1 above. Therefore, an increase in the conduction band effective mass leads to an increase in the reduced density of states. Assuming the overlap integral to be the same for all three samples, the matrix element must decrease with increasing nitrogen content faster than the increasing conduction band effective mass increases the reduced density of states.

To better understand the effect on absorption due to changes in matrix element and effective mass, some values presented in the literature are compared to the observed changes in peak absorption. Two comparisons were made between

theory and experiment. In the first case, predicted values of effective masses from the literature were used with the experimental results to predict the change in matrix element when nitrogen is added to the InGaAs QW. The references and effective mass numbers used appear in Table 4.2. The second method calculates the predicted maximum absorption from literature values for effective masses and matrix element for an InGaAs QW. This was not possible for InGaAsN due to the lack of data available for the variation of matrix element with nitrogen content. This calculation is then compared with the experimentally measured maximum absorption. In all cases, the overlap integral was assumed to be equal to one.

Reference	QW composition	$m_c(m_0)$	$m_v(m_0)$
[4.12]	$In_{0.43}Ga_{0.57}As$	0.047	0.457
[4.12]	$In_{0.43}Ga_{0.57}As_{0.9938}N_{0.0062}$	0.069	0.457
[4.8] and [4.11]	$In_{0.35}Ga_{0.65}As$	0.053	0.1
[4.8] and [4.11]	$In_{0.35}Ga_{0.65}As_{0.995}N_{0.005}$	0.072	0.1

Table 4.2 Quantities taken from references and used to predict change in matrix element.

The reduced density of states can be calculated from the effective masses given in Table 4.2 above. Comparing this with the experimentally measured reduction in absorption allows calculation of the change in matrix element needed to explain the experimental results. The calculated change in reduced density of states from the literature and the change in absorption observed in experiment are presented in Table 4.3.

Effective mass numbers from reference	Calculated ρ_r relative to 0% N	Experimental A_{max} for 0.5% relative to 0% N	Predicted $\|M\|^2$ relative to InGaAs
[4.12]	1.41	0.81	0.58
[4.8] and [4.11]	1.22	0.81	0.67

Table 4.3 Calculated increase in reduced density of states, observed reduction in maximum absorption and predicted change in matrix element.

The effective masses in the literature and the experimentally observed maximum absorption values predict that in an InGaAsN QW with approximately 0.5% nitrogen, the matrix element is reduced to a factor 0.67 or less of the value in an equivalent QW with 0% nitrogen,

To calculate the maximum absorption, the matrix element must be known. Table 4.1 of [4.13] gives the relationship between the magnitude of the matrix element and the indium fraction (x) in InGaAs to be:

$$\frac{2|M|^2}{m_0} = 28.8 - 6.6x$$

Equation 4.2

Unfortunately, a similar equation is not yet known for InGaAsN. Using Equation 4.2 and the values of the effective masses it is possible to calculate the peak absorption for an InGaAs QW. For a conduction band effective mass interpolated from [4.13] and a valence band mass from [4.11] the absorption for an $In_{0.40}Ga_{0.60}As$ QW was calculated to be $164cm^{-1}$. This is in reasonable agreement with the value measured in the experiment of $150\pm5cm^{-1}$.

4.5.2 Effect of Nitrogen on Modal Gain and Spontaneous Emission Spectra

The modal gain spectra for the three samples measured at 300K are shown in Figure 4.8. In this plot, the modal gain spectra have been shifted by the bandgap energies measured from the modal absorption spectra. This allows for easier comparison between the spectra to examine any changes in shape produced by the inclusion of nitrogen in the QW. As in the previous figures, data in pink is the sample with 0% nitrogen, data in turquoise is the sample with 0.5% nitrogen and the data in black is the 0.8% sample.

Shifting the data for the InGaAs sample by the bandgap energy does not appear to align it with data for the other two samples. This observation can be explained by the increase in broadening seen as nitrogen content increases, as was observed for the absorption spectra. As the broadening of the gain spectra increases, the peak gain moves to higher photon energy. For the data in Figure 4.8 the difference in peak gain between the samples is approximately 10meV. This value can be accounted for by the increase in broadening and errors associated with the bandgaps shown in Table 4.1. The increased broadening is particularly apparent in the highest peak gain spectra for the sample containing 0.8% nitrogen. However, in this case, the increased broadening of the gain spectra is due to population of a second confined state as well as the increased broadening seen in the absorption spectra. The presence of this second state is more apparent in the spontaneous emission spectra of Figure 4.9.

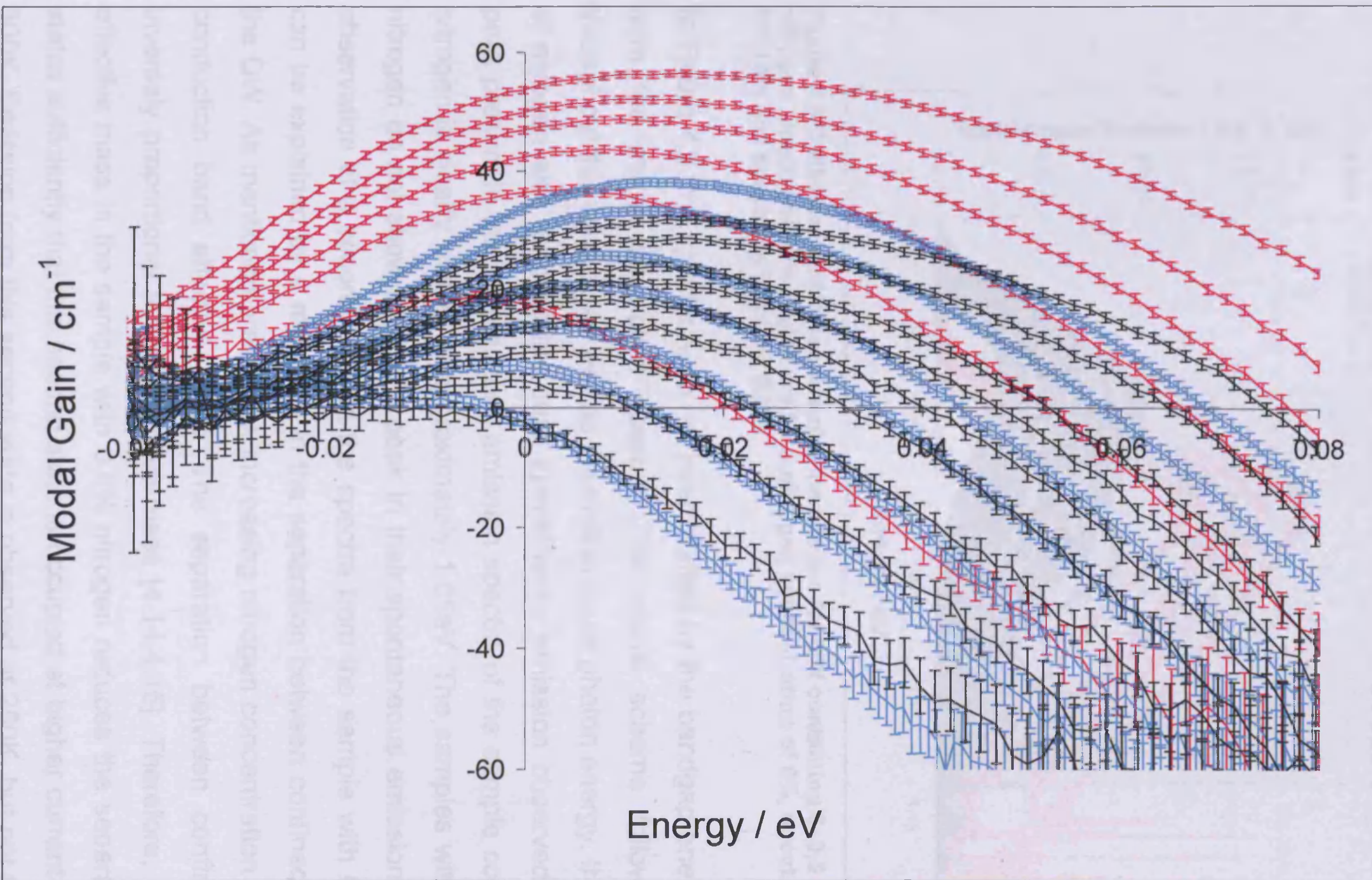

Figure 4.8 Modal gain spectra for samples containing 0, 0.5 and 0.8% nitrogen in the QW at 300K. The data for each sample has been shifted by the bandgap energy determined from the absorption spectra for that sample. Spectra shown in pink are for a nitrogen concentration of 0%, spectra in turquoise for 0.5% and spectra in black for 0.8%. The figure is shown full page to aid the viewer.

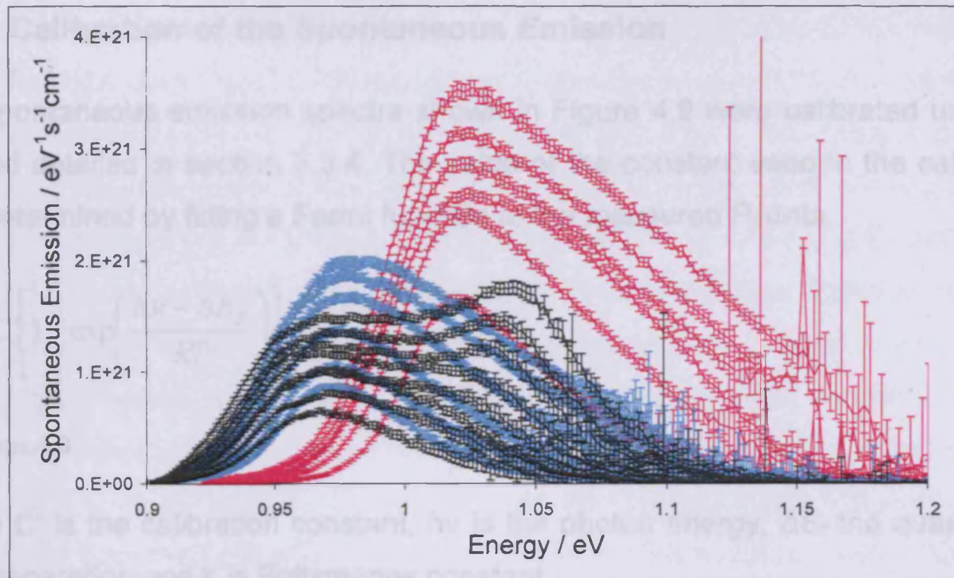

Figure 4.9 Calibrated spontaneous emission spectra for QW containing 0, 0.5 and 0.8% nitrogen. Spectra shown in pink are for a nitrogen concentration of 0%, spectra in turquoise for 0.5% and spectra in black for 0.8%.

In Figure 4.9, the spectra have not been shifted by the bandgap energy measured from the modal absorption spectra. The colour scheme follows that used throughout this section. As well as the shift to lower photon energy, the introduction of nitrogen also reduces the peak spontaneous emission observed. The second peak present in the spontaneous emission spectra of the sample containing 0.8% nitrogen is clearly visible, at approximately 1.05eV. The samples with 0.5 and 0% nitrogen do not show a second peak in their spontaneous emission spectra. The observation of a second peak in the spectra from the sample with 0.8% nitrogen can be explained by a reduction in the separation between confined states within the QW. As mentioned previously, increasing nitrogen concentration increases the conduction band effective mass. The separation between confined states is inversely proportional to the effective mass [4.14,4.15]. Therefore, the increased effective mass in the sample with 0.8% nitrogen reduces the separation between states sufficiently that this second state is occupied at higher current densities and 300K. Emission from this second state is observed at 250K, but not at 200K at the current densities used for these experiments.

4.5.3 Calibration of the Spontaneous Emission

The spontaneous emission spectra shown in Figure 4.9 were calibrated using the method detailed in section 3.3.4. The value of the constant used in the calibration was determined by fitting a Fermi function to the measured P_f data.

$$P_f = C'\left[1 - \exp\left(\frac{h\nu - \Delta E_f}{kT}\right)\right]$$

Equation 4.3

where C' is the calibration constant, hv is the photon energy, ΔE_f the quasi Fermi level separation and k is Boltzmanns constant.

Examples of these curve fittings are shown in Figure 4.10.

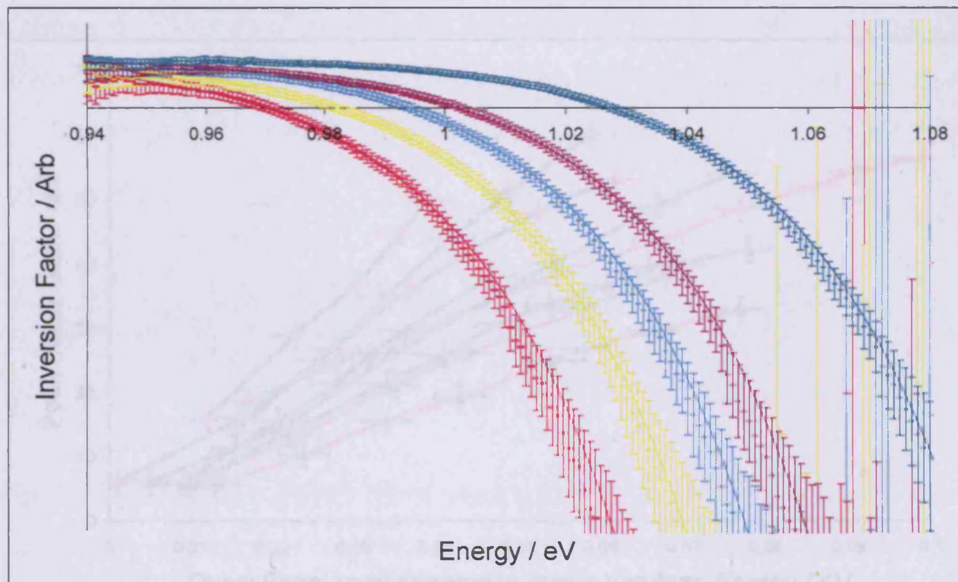

Figure 4.10 Fits to measured inversion factor data for sample with 0.5% nitrogen at 300K. Data in pink is for low current density, data in dark green is for high current density.

The symbols and error bars represent the experimental data and the lines are fits to the data. This plot clearly illustrates the importance of the error analysis carried out in this work. Without error bars on the data points, it would be impossible to determine the region of data to fit and to judge how well data is described by the

fitted function. As the diagram shows, the measured data is well described by a Fermi function. The fitted functions shown in the figure all require the same value for the calibration constant. The only other quantity that was adjustable in the fitting procedure was the quasi Fermi level separation. This was only allowed to vary within the range of the error bars. The fact that data measured at different current densities could be fitted using the same calibration constant indicates that the assumption that either f_c equal to one or f_v equal to zero is valid. However, the largest peak gains measured in this work are not as high as the maximum absorption measured from the samples so the system is not fully inverted (f_c equal to one and f_v equal to zero). For all samples and temperatures measured in this work it was possible to fit a Fermi function to the experimental inversion factor data and hence obtain the calibration factors, C'.

4.5.4 Comparison of Samples at Different Temperatures

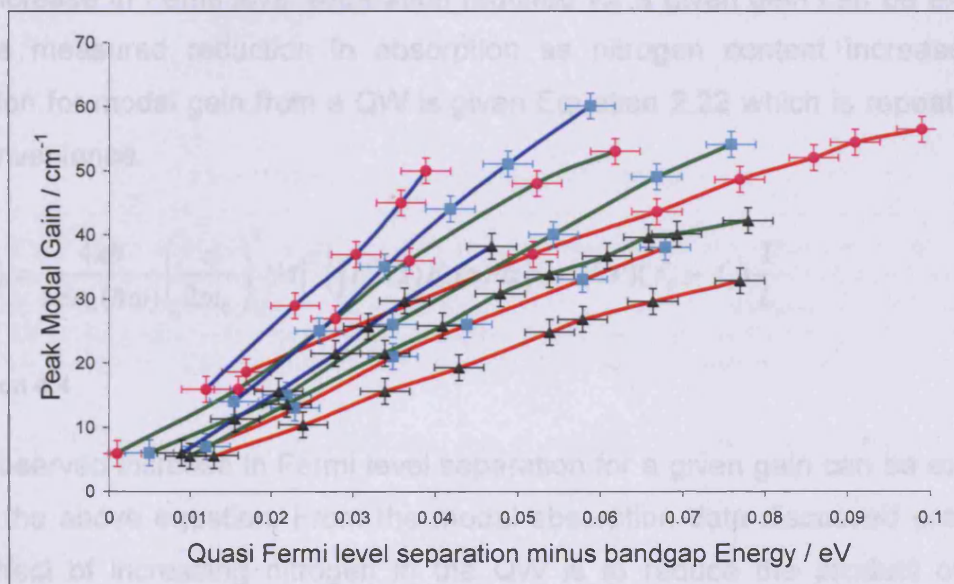

Figure 4.11 Peak modal gain vs quasi Fermi level separation for the three samples and temperatures of 300 (red lines), 250 (green lines) and 200K (blue lines). Pink symbols show data with a QW nitrogen content of 0%, turqoise symbols for 0.5% and black symbols for 0.8%.

Figure 4.11 shows the peak of the modal gain spectrum plotted against the quasi Fermi level separation, as determined by the fitting procedure detailed above. The

x axis plots the quasi Fermi level relative to the bandgap energy determined from the modal absorption data. Subtracting the bandgap measured from the modal absorption spectra allows for comparisons to be made at similar injection levels between the samples with different nitrogen content and measurements carried out at different temperatures. This plot introduces the colour scheme that will be used in graphs from now on. The colour of the symbols and error bars follows the same key as previous figures. That is, pink for the sample with 0% nitrogen, turquoise for the sample with 0.5% nitrogen and black for the sample with 0.8% nitrogen. The colour of the lines connecting the data points shows which temperature the data was collected at. A red line shows the data was collected at 300K, green at 250K and a blue line shows 200K. As the nitrogen content in the QW is increased, the quasi Fermi level separation relative to the bandgap energy required to reach a fixed gain increases also. This is true at 300, 250 and 200K.

The increase in Fermi level separation required for a given gain can be explained by the measured reduction in absorption as nitrogen content increases. The equation for modal gain from a QW is given Equation 2.22 which is repeated here for convenience.

$$G(\hbar\omega) = \frac{4\pi\hbar}{nc\varepsilon_0(\hbar\omega)}\left(\frac{e}{2m_0}\right)^2 |M|^2 \left\{\int F_v^*(z)F_c(z)dz\right\}^2 \rho_r(h\nu)(f_c - f_v)\frac{\Gamma}{L_z}$$

Equation 4.4

The observed increase in Fermi level separation for a given gain can be explained using the above equation. From the modal absorption data discussed previously, the effect of increasing nitrogen in the QW is to reduce the product of matrix element and reduced density of states. This then requires that to achieve the same modal gain, the quantity $(f_c - f_v)$ in Equation 4.4 must be greater in the nitrogen containing structures than the InGaAs QW. That is, the population inversion must be larger, giving f_c greater than f_v. For a system described by Fermi – Dirac

statistics, this occurs when the quasi Fermi level separation in the structure is increased, in agreement with the results of Figure 4.11.

In Figure 4.12 the values of peak modal gain shown in Figure 4.11 for the two samples containing nitrogen were multiplied by the scaling factors shown in the final row of Table 4.1. This procedure removes the changes observed in matrix element and reduced density of states from the analysis.

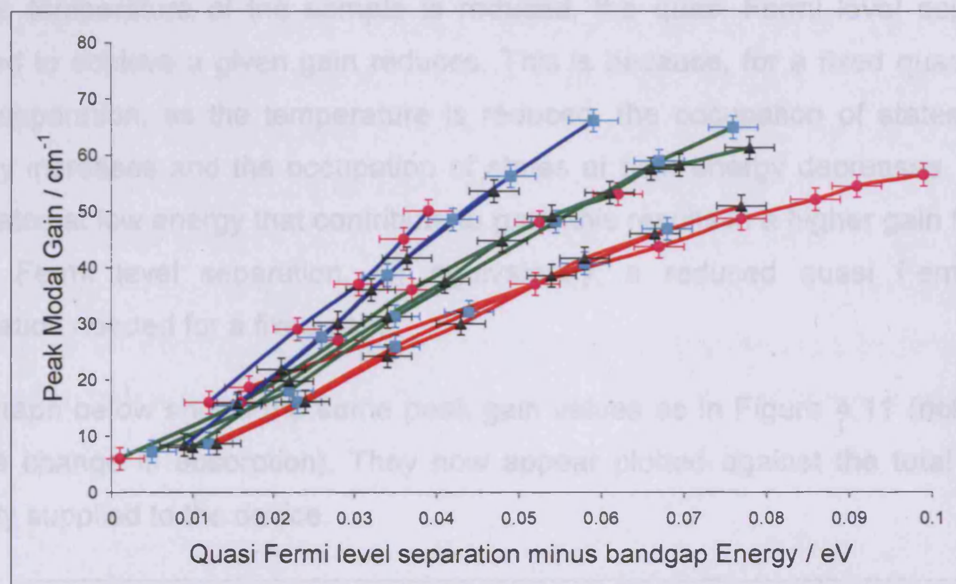

Figure 4.12 Peak modal gain vs quasi Fermi level separation for the three samples and temperatures of 300 (red lines), 250 (green lines) and 200K (blue lines). Pink symbols show data with a QW nitrogen content of 0%, turqoise symbols for 0.5% and black symbols for 0.8%. The peak modal gain values for the samples with 0.5% and 0.8% nitrogen have been scaled by the the fractional change in absorption relative to the sample with 0% nitrogen.

The results of Figure 4.12 indicate that the changes in matrix element and reduced density of states are the dominant factors in the need for increased quasi Fermi level separation to achieve fixed gain in the samples containing nitrogen. When these effects are taken in consideration, as in Figure 4.12, the quasi Fermi level separation needed to achieve a given gain is the same in all samples at a fixed temperature. Therefore the increased broadening seen in the modal absorption spectra has a very small effect on the modal gain spectra. The highest increase in the half width of the broadening is 4meV. This is of the same order as the error bars associated with the x axis of Figure 4.12 so precise conclusions of the effect

of broadening in these samples cannot be drawn. However, at 300K and low values of gain there does appear to be a difference between the curves for the samples with and without nitrogen. Likewise at 200K, the quasi Fermi level separation needed for fixed gain is reduced in the InGaAs sample. These observations can be explained by the increase in broadening seen in the structures containing nitrogen.

As the temperature of the sample is reduced, the quasi Fermi level separation needed to achieve a given gain reduces. This is because, for a fixed quasi Fermi level separation, as the temperature is reduced, the occupation of states at low energy increases and the occupation of states at high energy decreases. As it is the states at low energy that contribute to gain, this results in a higher gain for fixed quasi Fermi level separation. Or equivalently, a reduced quasi Fermi level separation needed for a fixed gain.

The graph below shows the same peak gain values as in Figure 4.11 (not scaled by the change in absorption). They now appear plotted against the total current density supplied to the device.

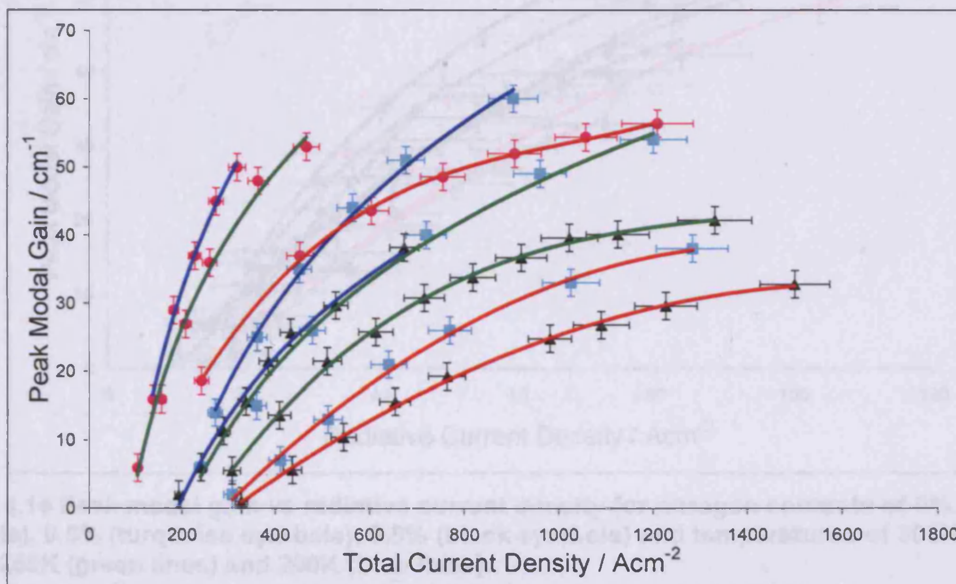

Figure 4.13 Peak modal gain vs total current density for 0 (pink symbols), 0.5 (turquoise symbols), 0.8% (black symbols) nitrogen content and temperatures of 300 (red lines), 250 (green lines) and 200K (blue lines). The lines are fits to the data to guide the eye.

The lines in Figure 4.13 are fits to the data and serve as guides to the eye. As the temperature is decreased, the current density required to achieve a given gain is reduced. This is true for all the devices. At a fixed temperature, the current density required to achieve a given gain is increased considerably in the samples containing nitrogen. At 300K the current density required for a given gain increases by a factor 2.5 at low values of gain and 3 at high values of gain when the nitrogen content goes from 0% to 0.5%. Looking at the shapes of the gain current curves, it would appear this factor would increase further at higher values of gain than those measured in these experiments. This indicates an increase in non radiative recombination of approximately a factor 3. Anton et al [4.16] carried out carrier lifetime measurements on these samples and concluded that there is an increase in monomolecular recombination of approximately a factor 4 between the samples with 0% and 0.5% nitrogen. Increasing the nitrogen content further to 0.8% in Figure 4.13 above produces an additional increase in the required current density of approximately a factor 1.3 at high gains, but a very small difference at low gains.

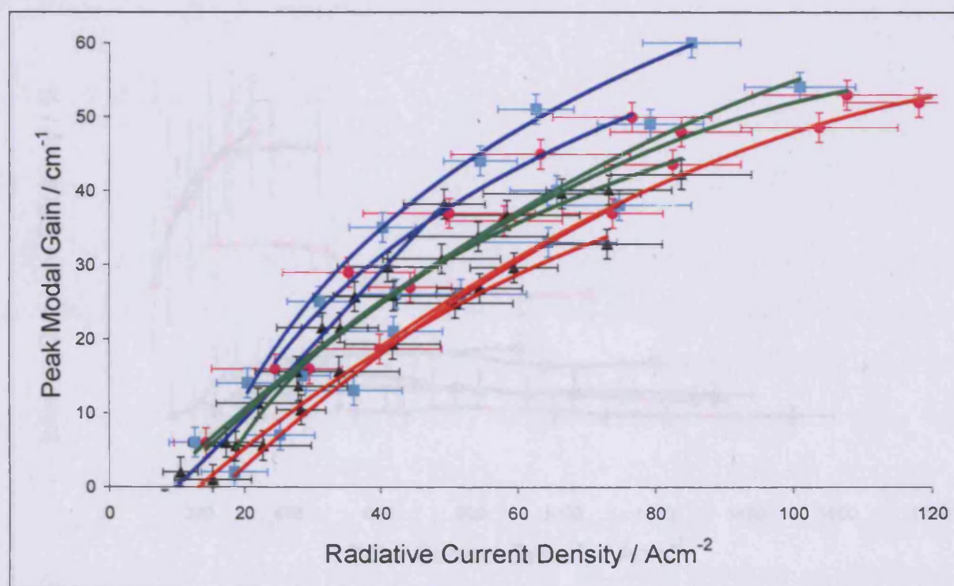

Figure 4.14 Peak modal gain vs radiative current density for nitrogen contents of 0% (pink symbols), 0.5% (turquoise symbols), 0.8% (black symbols) and temperatures of 300K (red lines), 250K (green lines) and 200K (blue lines).

Figure 4.14 plots the peak modal gain against the radiative current density calculated from the calibrated spontaneous emission rate spectra. The colour scheme remains the same as that used previously. The lines are fits through the data and serve as guides to the eye. The colour of the symbols and error bars denotes the nitrogen concentration: pink for 0%, turquoise for 0.5% and black for 0.8%. As in Figure 4.13, as the temperature is reduced, the radiative current density appears to be reduced also. However, the error bars show that this conclusion cannot be made with complete confidence. Within the experimental error it is possible that there is no change in radiative current density vs peak modal gain as temperature is reduced. Within the experimental error, the introduction of nitrogen into the QW has no effect on the radiative current density required to achieve a given gain. This is true at temperatures of 300, 250 and 200K and agrees with figure 4(b) of Tomic et al [4.6] which shows calculations carried out for an InGaAsN QW containing 36% indium and 2% nitrogen and the same QW without nitrogen.

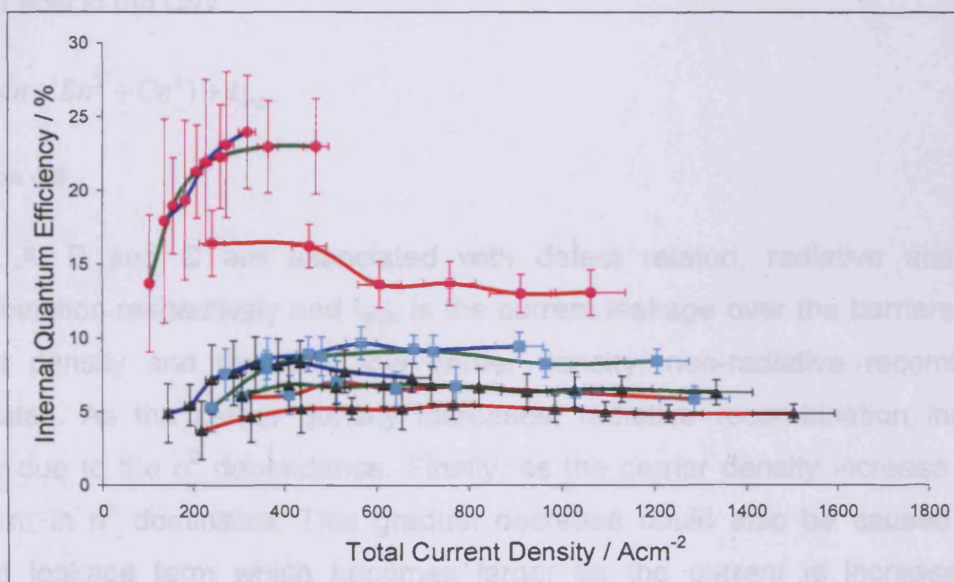

Figure 4.15 Calculated internal quantum efficiency as a function of total drive current density for samples with 0% (pink symbols), 0.5% (turquoise symbols) and 0.8% (black symbols) nitrogen in the QW at temperatures of 300K (red lines), 250K (green lines) and 200K (blue lines).

Figure 4.15 shows the calculated internal quantum efficiency, defined as radiative current density divided by total current density, plotted as a function of total current density. The colour scheme used is once again the same as that used throughout this section. The measured internal quantum efficiency is greatly reduced in the samples containing nitrogen. This reduction is approximately a factor 3 at 300K and increases to a factor 4-5 at 250 or 200K. The measured reduction in efficiency shows that the introduction of nitrogen into the InGaAsN QW must strongly increase the non radiative recombination processes present in the structure. The efficiencies plotted in Figure 4.15 show similar behaviour as total current density is increased. At low current density there is a strong increase in efficiency as the current density is increased. As the current density is increased further, the measured efficiency reaches a maximum before levelling out or possibly following a gradual reduction as the current density is increased further. This behaviour can be explained using the commonly used dependences of defect related, radiative and auger recombination on the carrier density (n) and how they contribute to current flow in the QW.

$$I = e(An + Bn^2 + Cn^3) + I_{leak}$$

Equation 4.5

where A, B and C are associated with defect related, radiative and Auger recombination respectively and I_{leak} is the current leakage over the barriers. At low current density and therefore low carrier density, non-radiative recombination dominates. As the carrier density increases, radiative recombination increases rapidly due to the n^2 dependence. Finally, as the carrier density increase further, the term in n^3 dominates. This gradual decrease could also be caused by the current leakage term which becomes larger as the current is increased. The presence of current leakage will be investigated further in Chapter 5. The three phases discussed above produce the increase, peak and then gradual reduction in efficiency observed in Figure 4.15. The only curve not displaying this behaviour is that measured for the sample with 0% nitrogen at 300K (pink symbols, red line).

This line does not disagree with the trend described above, it appears that the current densities used in the measurement of this sample at this temperature all fall above the peak in measured internal quantum efficiency. Therefore only the second part of the trend described above is observed in this data. That is a gradual reduction in efficiency as current density is increased.

4.5.5 Comparison with alternative measurement techniques.

In Figure 4.16 below, the peak modal gain vs total current density data shown previously in Figure 4.13 is compared to data measured by Schterengas et al [4.17] using the Hakki Paoli method. This comparison is made with data measured at 300K.

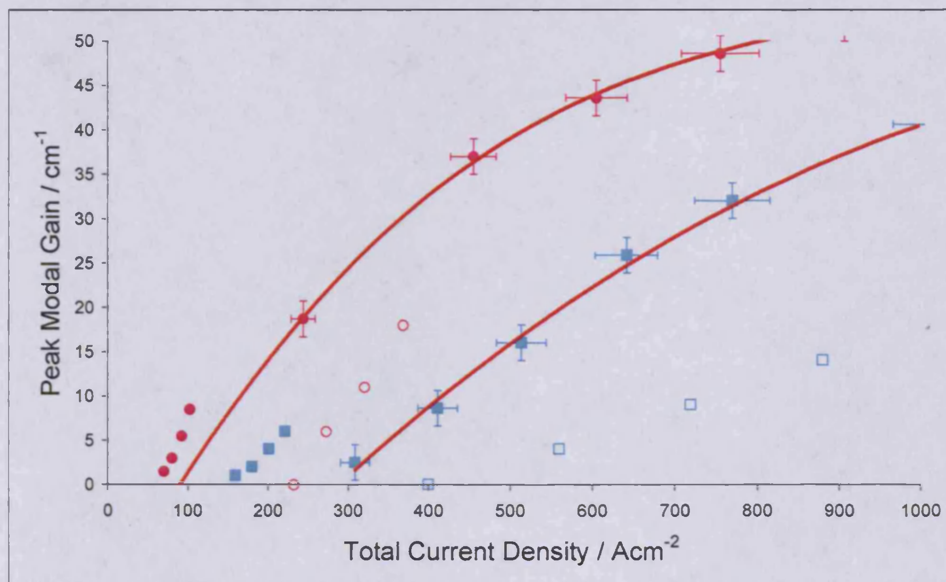

Figure 4.16 Comparison between data measured in this work and [4.17] for nitrogen contents of 0 (pink) and 0.5% (turquoise). The points with error bars are data from this work. Closed symbols are for broad area devices and open symbols for ridge devices, both taken from [4.17]

The plot shows that good agreement is not found between the different sets of data. The Schterengas et al data shown by solid symbols was measured on samples with a nominal stripe width of 100µm compared to the nominal 50µm used in this work. For a given gain, a lower current density is required for the wider stripe

structures. The data shown as open symbols were measured on ridge structure samples. This data requires higher current density for fixed gain than the 50μm data measured in this work. The differences between the data measured on different width samples can most probably be attributed to current spreading effects. As has been discussed previously the effects of current spreading must be taken into account when comparing sample's total current densities. In addition, in the wide stripe devices, the gain may be higher in the centre than at the edges of the stripe. During the testing of the equipment used in this work, excellent agreement was obtained between segmented contact method measurements and laser threshold data. (see Figure 3.14) These data were measured on samples with the same stripe width. It is concluded that in order to compare different measurement techniques accurately, the same stripe width samples must be used for the comparisons.

4.6 Summary.

In this chapter, the segmented contact method has been used to measure the modal gain, absorption and spontaneous emission in real units from three InGaAsN QW samples. The QWs consisted of 40% indium and 0%, 0.5% or 0.8% nitrogen. The measurements were carried out with the samples at temperatures of 300K, 250K and 200K. It was found that increasing the nitrogen content of the QW led to a reduction in the maximum absorption and an increase in the broadening of the absorption and gain spectra. From the reduction in maximum absorption and reported values of effective masses, it was deduced that the matrix element decreases by a factor 0.58 between 0 and 0.5% nitrogen. When increasing the nitrogen content from 0 to 0.8% a reduction of a factor 0.67 was required to fit the experimental data. This conclusion was supported by the need for a higher quasi Fermi level separation to achieve a given gain as the nitrogen content increased. The total current density needed to achieve a given gain was also increased in the samples containing nitrogen. This increase was a factor 3 in the sample with 0.5% nitrogen and a factor 4 in the sample with 0.8% nitrogen. The calibrated

spontaneous emission spectra were then used to calculate the radiative current density and internal quantum efficiency. In contrast to the quasi Fermi level separation and total current density, the radiative current density required for a given gain did not increase as the nitrogen content increased in the QW. This result is very positive for future devices, if the non radiative recombination can be reduced in the InGaAsN samples; it should be possible to make lasers with threshold current densities comparable to an equivalent InGaAs structure. Finally the internal quantum efficiency was found to be approximately a factor three lower in the InGaAsN samples at 300K. The efficiency was found to be dominated by defect related recombination at low current densities, as the current density increases, radiative recombination becomes more significant before the possible onset of strong Auger recombination or thermal leakage current.

4.7 References

4.1 N. Tansu, J. Y. Yeh, L.J. Mawst, *Appl Phys Letts*, **82** (2003) 4038

4.2 S. Sato, *Jpn J Appl Phys*, **39** (2000) 3403

4.3 J. Y. Yeh, N. Tansu, L. J. Mawst, *IEEE Photon. Technol. Lett.*, **16** (2004) 741

4.4 N. Tansu, L. J. Mawst, *IEEE Photon. Technol. Lett.*, **14** (2002) 444

4.5 D. Alexandropoulos, M. J. Adams, *J. Phys.: Condens. Matter* **14** (2002) 3523

4.6 S. Tomić, E. P. O'Reilly, R. Fehse, S. J. Sweeney, A. R. Adams, A. D. Andreev, S. A. Choulis, T. J. C. Hosea, H. Riechert, *IEEE J. Select Topics Quantum Electron.*, **9** (2003) 1228

4.7 C. Skierbiszewski, P. Perlin, P. Wisniewski, W. Knap, T. Suski, W. Walukiewicz, W. Shan, K. M. Yu, J. W. Ager, E. E. Haller, J. F. Geisz, J. M. Olsen, *Appl Phys Letts*, **76** (2000) 2409

4.8 J. M. Ulloa, J. L. Sánchez-Rojas, Adrian Hierro, J. M. G. Tijero, E. Tournié, *IEEE J. Select Topics Quantum Electron.*, **9** (2003) 716

4.9 Z. Pan, L. H. Li, Y. W. Lin, B. Q. Sun, D. S. Jiang, W. K. Ge, *Appl Phys Letts* **78** (2001) 2217

4.10 A. Lindsay, E. P. O'Reilly, *Solid State Commun.*, **112** (1999) 443

4.11 M. S. Wartak, P. Weetman, *J. Appl Phys*, **98** (2005) 113705

4.12 N. Tansu, L.J. Mawst, *Appl Phys Letts*, **82** (2003) 1500

4.13 L. A. Coldren, S. W. Corzine, "Diode lasers and Photonic Integrated Circuits" Wiley, New York (1995)

4.14 J. R. Hook, H. E. Hall, "Solid State Physics – second edition", John Wiley and Sons, Chichester (1991)

4.15 J. Wilson, J. Hawkes, "Optoelectronics: an introduction – third edition", Prentice Hall, Hemel Hempstead (1998)

4.16 O. Anton, C. S. Menoni, J. Y. Yeh, L. J. Mawst, J. M. Pikal, N. Tansu, *IEEE Photon. Technol. Lett.*, **17** (2005) 953

4.17 L. Schterngas, G. L. Belenky, J. Y. Yeh, L. J. Mawst, *IEEE J. Select Topics Quantum Electron.*, **11** (2005) 1063.

Chapter 5 Effect of Barrier material on InGaAsN Quantum Well

5.1 Introduction

In this chapter the importance of thermally activated leakage from the InGaAsN QW is investigated. Comparisons are made between two samples with the same $In_{0.4}Ga_{0.6}As_{0.995}N_{0.005}$ QW but different materials adjacent to the quantum well. One sample has GaAs adjacent to the well, the other GaAsP. The GaAsP material has a wider bandgap than GaAs, creating a deeper well for both electrons and holes. Modal absorption, modal gain and spontaneous emission spectra were measured for both samples using the segmented contact method at temperatures of 300, 250 and 200K. The spontaneous emission spectra were calibrated and the radiative current density and internal efficiency calculated. Comparisons are made between the measured spectra and the peak modal gain vs current density curves. To observe any possible emission from the barrier material the spontaneous emission spectra were also measured from the top of the two samples.

5.2 Samples studied in this work

In this section of work, the effect of the QW barrier height on gain and recombination properties is investigated. It is reported that increasing nitrogen content in the InGaAsN QW increases the well depth in the conduction band [5.1,5.2]. The deep well provides strong confinement of electrons in InGaAsN. However, the effect of increasing nitrogen content on the valence band well depth is not so well understood. Several groups report that increasing the nitrogen content has negligible effect on the valance band confinement. [5.2,5.3] Other reports suggest that the valence band well depth decreases with increasing nitrogen content [5.1,5.5]. Whatever the effect of nitrogen on the valence band barrier height, the holes in InGaAsN are much more weakly confined than the electrons, typically 99-130meV compared to 350-450meV [5.1,5.4,5.6]. This could

lead to the leakage of holes being an important mechanism in explaining the low internal quantum efficiencies measured in Chapter 4. To investigate the effects of carrier leakage, two single QW samples are studied here. Figure 5.1 shows a schematic of the QW region for these two samples. The figure shows only the QW region so that the differences between the samples can be displayed. The remaining structural details such as waveguide core and cladding are the same as those shown in Figure 4.1.

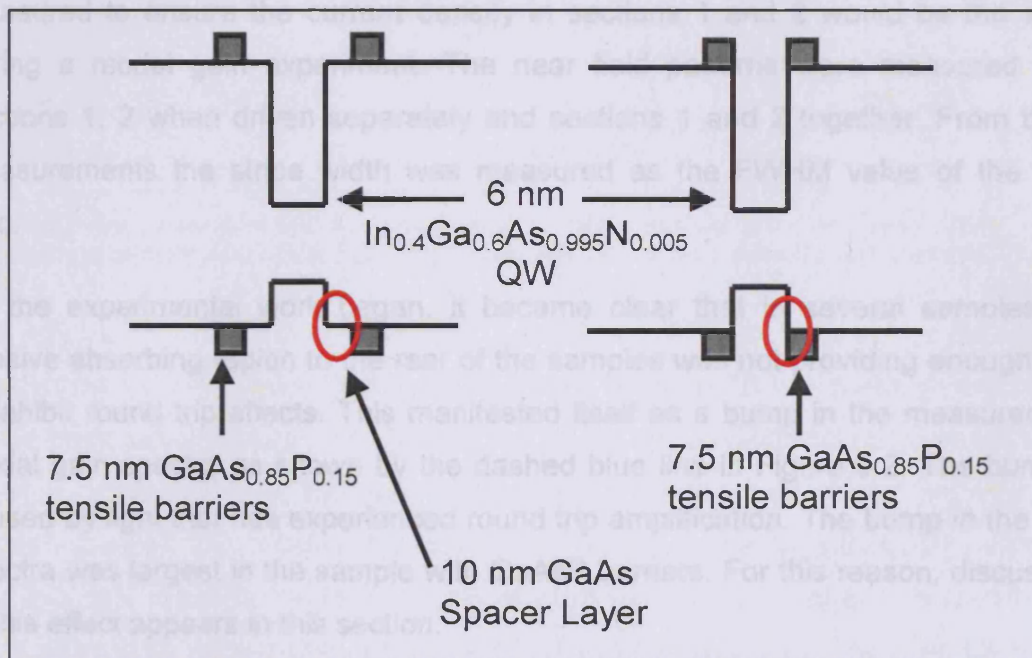

Figure 5.1 Schematic diagram of QW region of sample with GaAs spacer layer and sample with GaAsP direct barriers.

The structure shown on the left of Figure 5.1 is the sample studied in chapter 4 with a nitrogen content of 0.5% in the QW. The second sample studied here has nominally the same QW nitrogen concentration, but the GaAsP tensile barriers are directly next to the well. In the other sample there is a 10nm GaAs spacer layer. This difference between the samples is highlighted in red on the diagram. In this section of work, the samples shall be referred to by the barrier material directly next to the well. The sample studied in Chapter 4 will be referred to as the GaAs barrier sample, and the new sample introduced here will be known as the GaAsP barrier sample. Aside from the different material adjacent to the QW, the two

samples are identical, comprising a single 6nm QW embedded in a 300nm GaAs SCH with AlGaAs cladding layers. Further details of the samples and measurements on lasers are given in [5.7].

5.3 Requirements of a Sample for Multisection Measurements.

The samples used in this chapter underwent the same tests before being measured as the samples in Chapter 4. The samples' I-V characteristics were measured to ensure the current density in sections 1 and 2 would be the same during a modal gain experiment. The near field patterns were measured from sections 1, 2 when driven separately and sections 1 and 2 together. From these measurements the stripe width was measured as the FWHM value of the near field.

As the experimental work began, it became clear that in several samples the passive absorbing region to the rear of the samples was not providing enough loss to inhibit round trip effects. This manifested itself as a bump in the measured net modal gain spectra as shown by the dashed blue line in Figure 5.2. The bump is caused by light that has experienced round trip amplification. The bump in the gain spectra was largest in the sample with GaAsP barriers. For this reason, discussion of this effect appears in this section.

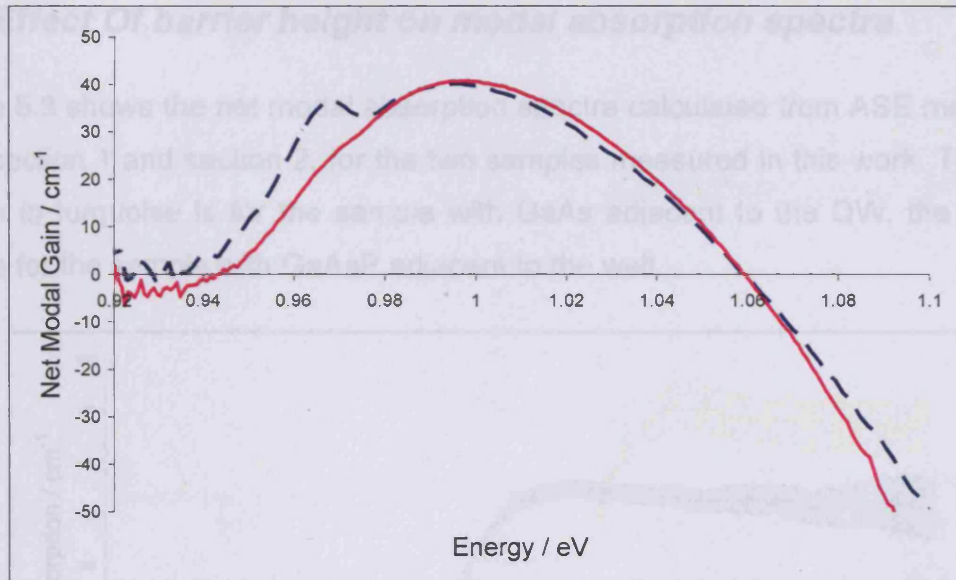

Figure 5.2 Net modal gain spectra before (dashed blue line) and after (solid pink line) damaging rear facet and grounding of rear section. For sample with GaAsP barriers.

The effects of round trip amplification had to be removed before any reasonable data could be acquired. This was important because the technique required a single pass measurement. To remove the round trip amplification the losses in the passive region had to be increased. This was achieved by damaging the rear facet of each sample. This produced a rear mirror with very low reflectivity. By doing this any light that reached the rear facet was scattered and no longer reflected by the facet, down the waveguide and back into the front sections. The rear section of each device was also grounded. This grounding prevented any carriers created by absorption in the rear section of the device recombining radiatively. The carriers are swept out of the device to ground before having time to recombine. A net modal gain spectrum measured after the steps taken to avoid round trip effects is shown as the solid pink line in Figure 5.2. All samples studied in this thesis (including those in Chapter 4) had the rear facet damaged and rear section earthed before measurements presented were taken.

5.4 Effect Of barrier height on modal absorption spectra

Figure 5.3 shows the net modal absorption spectra calculated from ASE measured from section 1 and section 2, for the two samples measured in this work. The data shown in turquoise is for the sample with GaAs adjacent to the QW, the data in gold is for the sample with GaAsP adjacent to the well.

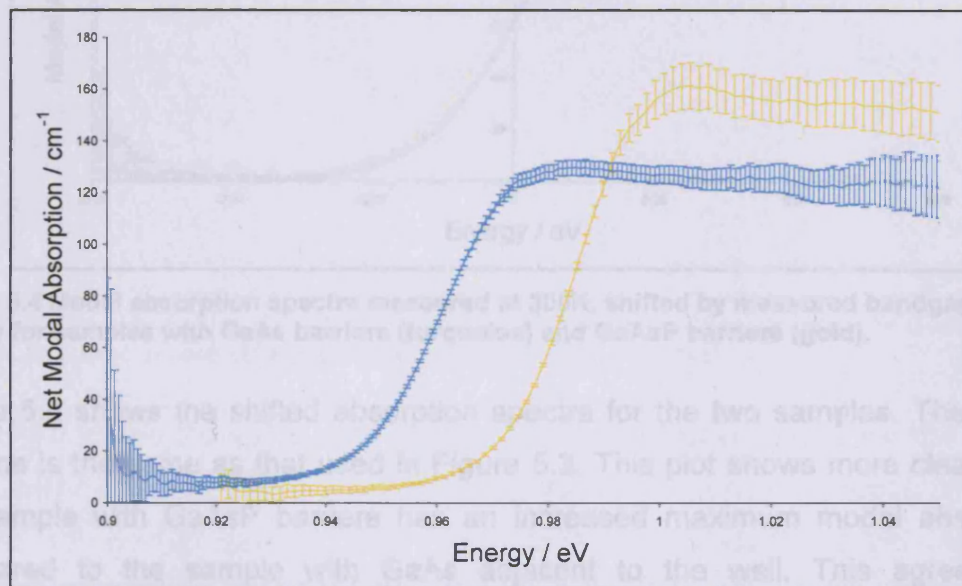

Figure 5.3 Net modal absorption spectra for sample with GaAs barriers (turquoise) and GaAsP barriers (gold). Measured at 300K.

The net modal absorption spectrum for the sample with GaAsP barriers shows a shift to higher photon energy relative to the sample with GaAs barriers. The internal optical loss was measured to be the same in both samples and equal to $7\pm2cm^{-1}$. The bandgap energies of the samples were measured in the same way as in section 4.5. The internal optical loss was subtracted and the modal absorption spectra shifted by the bandgap energy to allow easier comparison of the spectra.

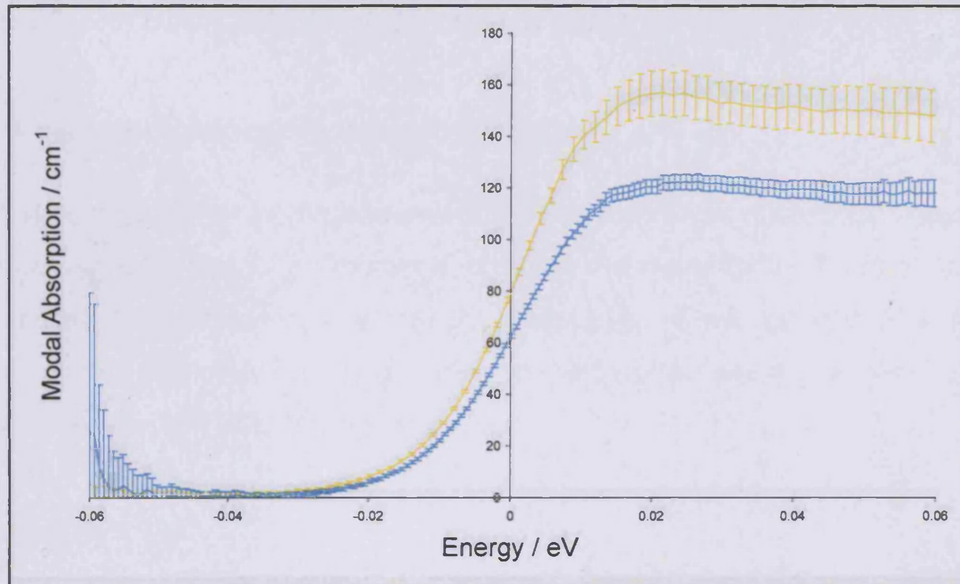

Figure 5.4 Modal absorption spectra measured at 300K, shifted by measured bandgap energy for samples with GaAs barriers (turquoise) and GaAsP barriers (gold).

Figure 5.4 shows the shifted absorption spectra for the two samples. The colour scheme is the same as that used in Figure 5.3. This plot shows more clearly that the sample with GaAsP barriers has an increased maximum modal absorption compared to the sample with GaAs adjacent to the well. This agrees with calculations made by Hader et al on structures with different barrier heights [5.8]. The increase observed in this work is equal to a factor of 1.28.

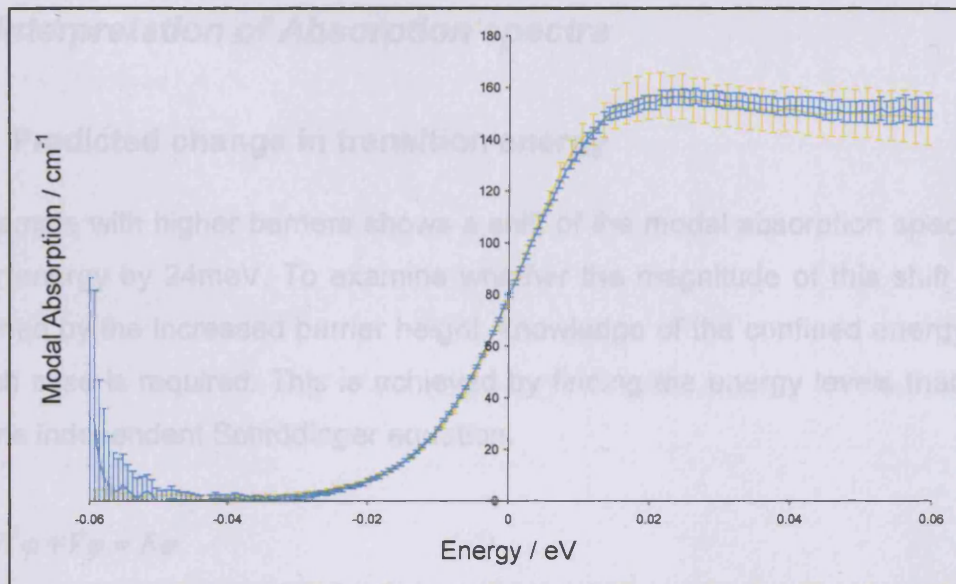

Figure 5.5 Modal absorption spectra for samples with GaAs (turquoise) and GaAsP (gold) barriers measured at 300K and shifted by the bandgap energy. The sample with GaAs barriers has been scaled to match the sample with GaAsP barriers.

Figure 5.5 shows the same data as Figure 5.4, but the spectrum for the sample with GaAs barriers has been scaled by a factor 1.28 to match the spectrum for the sample with GaAsP barriers. From this plot it is concluded that the change in material adjacent to the QW has little effect on the broadening of the modal absorption spectra. The maximum absorption of each sample remains the same for temperatures of 250 and 200K. However, at lower temperatures, the sample with GaAs barriers appears to show an increase in broadening relative to the GaAsP barrier sample. However, this effect is small and within the error bars of ±1meV associated with the broadening.

5.5 Interpretation of Absorption spectra

5.5.1 Predicted change in transition energy

The sample with higher barriers shows a shift of the modal absorption spectrum to higher energy by 24meV. To examine whether the magnitude of this shift can be explained by the increased barrier height, knowledge of the confined energy levels in each case is required. This is achieved by finding the energy levels that satisfy the time independent Schrödinger equation.

$$\frac{-\hbar^2}{2m^*}\nabla^2\varphi + V\varphi = E\varphi$$

Equation 5.1

where V is the potential energy. For a finite QW structure, the energy levels can be found using a graphical solution method as detailed in [5.9,5.10].

As a check of both the calculation and experiment, the calculation of confined energy levels was first completed for an $In_{0.43}Ga_{0.57}As$ QW with GaAs barriers. Material parameters were taken from [5.1]. The n=1 energy levels were calculated to be 99meV and 14meV for conduction and valence band respectively. The transition energy measured from the absorption data is 1.013eV from Table 4.1. These numbers predict a strained bulk bandgap of 900meV. This is in reasonable agreement with figure 9 of chapter 8 in [5.12] which yields a value of approximately 950meV.

To analyse the specific case of an InGaAsN well with either GaAs of GaAsP barriers, the energy levels were calculated for parameters from two different references [5.1, 5.4]. Two sets of material parameters were chosen because of the variation in offset energies presented in the literature. For each case, the energy levels were found for an InGaAsN QW with GaAs barriers, and the same well with GaAsP barriers. The conduction band offset ratio was assumed to be the same

with GaAs or GaAsP barriers. The material parameters used in the calculations appear in Table 5.1.

	(a)	(a)	(b)	(b)
Reference	5.1	5.1	5.4	5.4
Well material	$In_{0.43}Ga_{0.57}$ $As_{0.9938}N_{0.0062}$	$In_{0.43}Ga_{0.57}$ $As_{0.9938}N_{0.0062}$	$In_{0.3}Ga_{0.7}$ $As_{0.99}N_{0.01}$	$In_{0.3}Ga_{0.7}$ $As_{0.99}N_{0.01}$
Barrier material	GaAs	$Ga_{0.85}P_{0.15}As$	GaAs	$Ga_{0.8}P_{0.2}As$
ΔE_c / meV	451	528	401	495
m^*_c well / m_0	0.069	0.069	0.069	0.069
m^*_c barrier / m_0	0.067	0.095	0.067	0.104
ΔE_v / meV	99	148	123	152
m^*_v well / m_0	0.457	0.457	0.1 [5.11]	0.1 [5.11]
m^*_v barrier / m_0	0.38	0.424	0.38	0.438

Table 5.1 Values used in solving Schrodinger's equation.

For calculations in the conduction (valence) band, zero energy was taken to be at the bottom (top) of the well. Any material parameters not given in the references were interpolated from the values in table 1.1 of [5.9].

The calculated confined energy levels for case (a) are shown on a schematic of the confining potential in Figure 5.6.

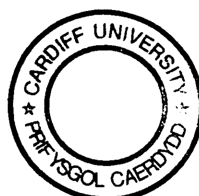
CARDIFF UNIVERSITY ★ PRIFYSGOL CAERDYDD

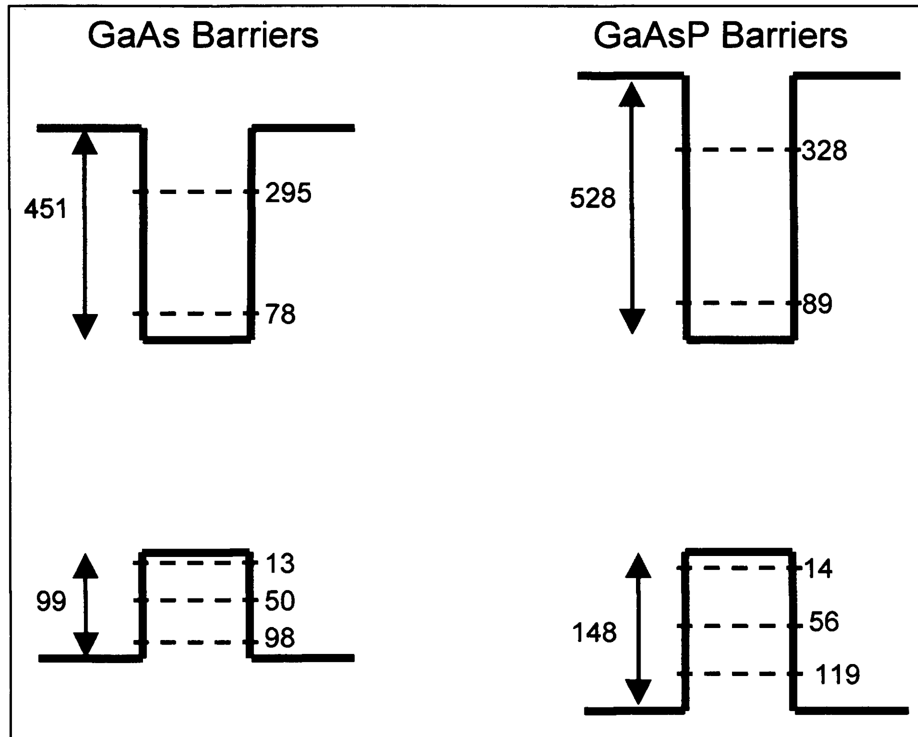

Figure 5.6 Schematic diagram showing well depths and calculated energy levels for material parameters taken from [5.1].

As Figure 5.6 shows, the calculations for case (a) predict that no change in the number of confined levels when the barrier material is changed to GaAsP from GaAs. However, the GaAsP barrier does increase the confinement effect, predicting an increase in e1 to HH1 transition energy of 12meV.

Figure 5.7 shows the confined energy levels for the material parameters of case (b).

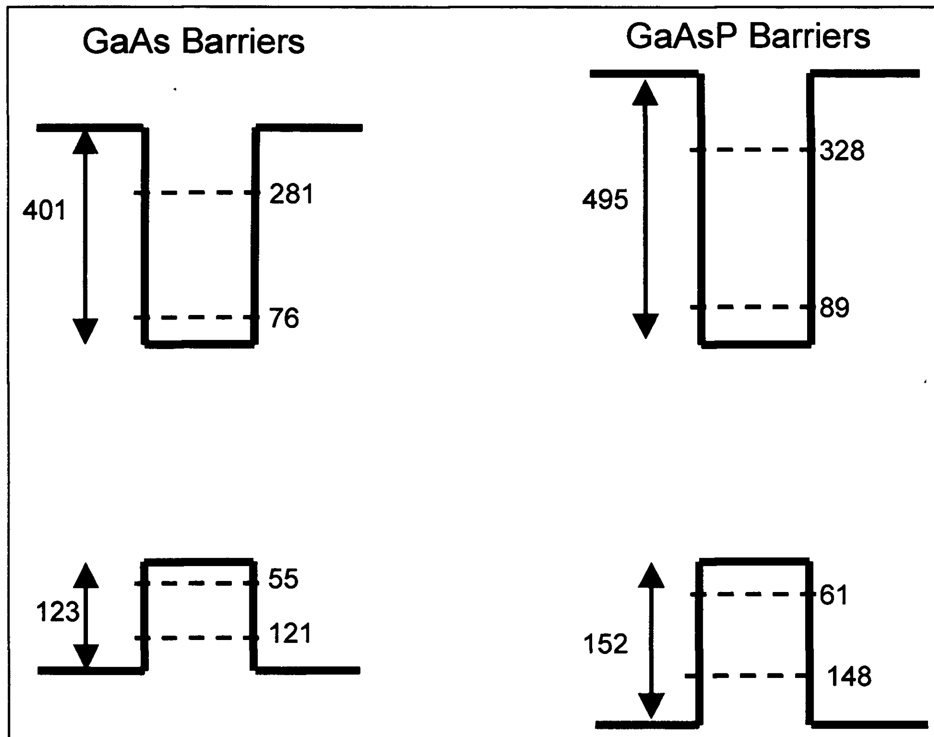

Figure 5.7 Schematic diagram showing well depths and calculated energy levels for material parameters taken from [5.4].

The material parameters of case (b) provide two calculated confined levels in both the conduction and valence band wells. This prediction remains the same whether GaAs or GaAsP barriers are used. For the material compositions described above, the predicted increase in e1 to HH1 transition energy is 19meV.

The calculated values of the increase in transition energy are smaller than the value measured in experiment, particularly for calculation (a) which uses well compositions closest to those studied experimentally. This implies that the shift to higher transition energy cannot be fully explained by the increase in barrier height. It is therefore possible that the compositions of the QWs in the two experimentally measured samples are not the same. A lower nitrogen or lower indium content in the QW with GaAsP barriers could explain the differences between calculation and experiment.

5.5.2 Analysis of observed change in maximum absorption

To try and further understand the cause of the differences in modal absorption spectra between the two structures, the effect of the barrier height on the overlap integral is investigated.

The sample with GaAsP barriers shows an increase in maximum absorption relative to the sample with GaAs barriers. The cause of this can be examined with Equation 4.1 which is repeated here as Equation 5.2 to aid the reader.

$$A(\hbar\omega) = \frac{4\pi\hbar}{nc\varepsilon_0(\hbar\omega)}\left(\frac{e}{2m_0}\right)^2 |M|^2 \left\{\int F_v^*(z)F_c(z)dz\right\}^2 \rho_r(h\nu)\frac{\Gamma}{L_z}$$

Equation 5.2

In Chapter 4, the reduction in absorption observed as the nitrogen content increased was explained by a reduction in the matrix element and an increase in the reduced density of states. In the two samples studied in this chapter, the QW composition is nominally the same, so the matrix element and reduced density of states should be similar in both samples as reported in [5.4]. Therefore a possible explanation for the increase in modal absorption in the sample with GaAsP barriers is an increase in the overlap integral relative to the sample with GaAs barriers.

Having found the confined energy levels in the well, the envelope functions due to the well potential can be calculated. For the n=1 transition and $k^2 = 2m^* E/\hbar^2$, the envelope functions within the well are:

$$F(z) = A\cos(kz)$$

Equation 5.3

Outside the well, the function decays exponentially. The normalising constant, A can be found using

$$\int_{-\infty}^{\infty} F^2(z)dz = 1$$

Equation 5.4

Having calculated the normalised envelope functions, the overlap integral can be calculated for the structures shown in Figure 5.6 and Figure 5.7. For all of the structures presented in these figures, the overlap integral did not change significantly and was typically equal to 0.97. Therefore, it is concluded that changing the barriers from GaAs to GaAsP has negligible effect on the overlap integral. In addition, the assumption of this being equal to one made in chapter 4 was a reasonable one.

Since the overlap integral does not change, this cannot be the reason for the increase in maximum absorption observed in the sample with GaAsP barriers. This supports the conclusion drawn in section 5.5, that the compositions of the QWs in the two samples may be different. As was observed in chapter 4, increasing the nitrogen concentration in the well produces a decrease in the maximum absorption due to a decrease in the matrix element. Therefore a lower nitrogen content in the GaAsP barrier sample would reproduce the result observed in Figure 5.4. From table 4.1 of [5.9], reducing the indium content in an InGaAs well increases the matrix element. This could also reproduce the increased maximum absorption for the GaAsP barrier sample. As mentioned in section 5.5, a reduced indium content in the sample with GaAsP barriers would explain the observed shift to higher photon energy.

5.6 Effect of Barrier Height on Modal Gain and Spontaneous Emission Spectra

Figure 5.8 shows the modal gain spectra for the two samples with different material adjacent to the QW.

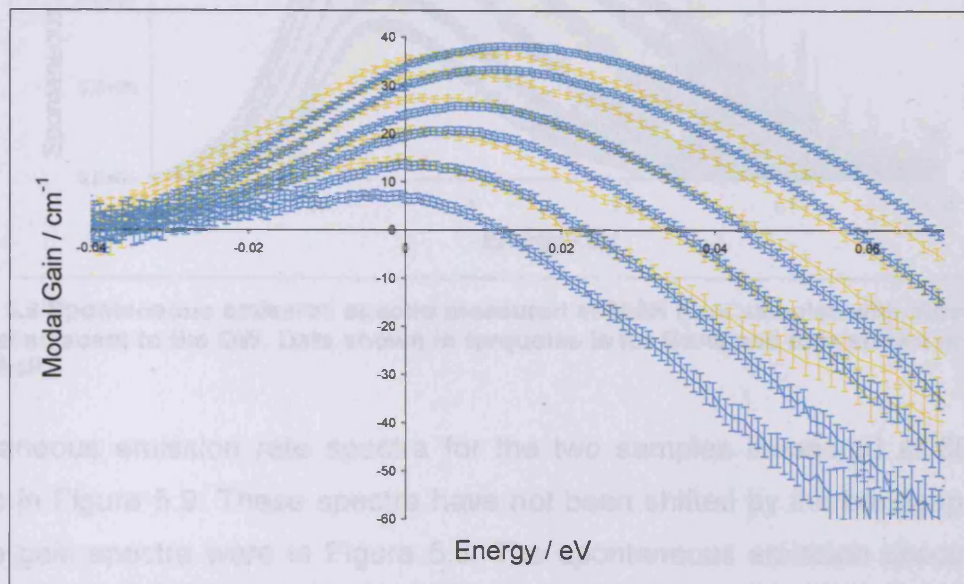

Figure 5.8 Modal gain spectra for samples with a barrier material of GaAs (turquoise) and GaAsP (gold). The spectra were measured at 300K and a range of drive current densities. The spectra have been shifted in energy by the bandgap measured from the absorption spectra from each sample.

The gain spectra for the two samples appear shifted in energy relative to each other. This could indicate reduced broadening of the gain spectra for the sample with GaAsP barriers. However, the shift is small, approximately 4meV between the peaks for the same gain. Aside from this shift, which is within the experimental error present in the determination of the bandgap energy, the gain spectra appear the same for both samples.

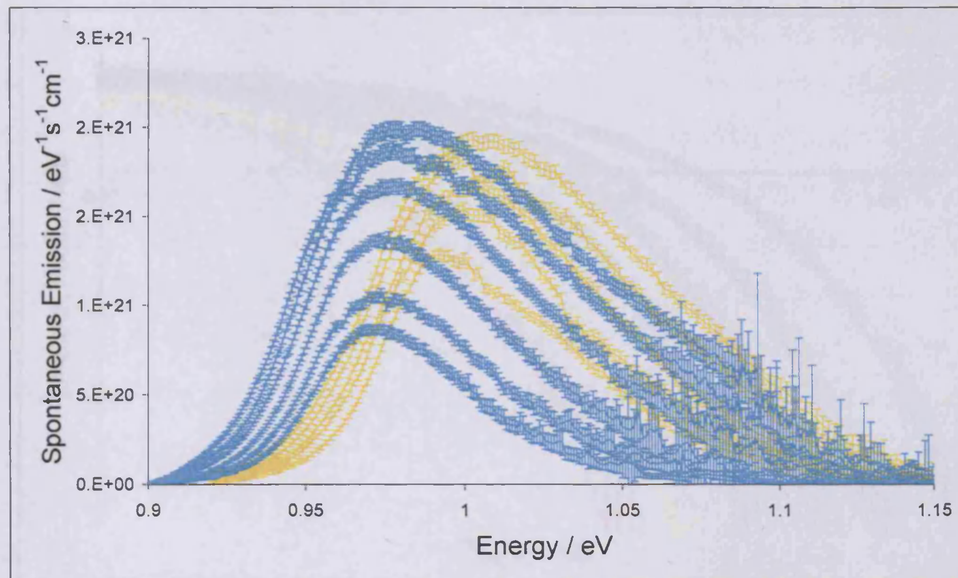

Figure 5.9 Spontaneous emission spectra measured at 300K from samples with different material adjacent to the QW. Data shown in turquoise is for GaAs and data shown in gold is for GaAsP.

Spontaneous emission rate spectra for the two samples measured at 300K are shown in Figure 5.9. These spectra have not been shifted by the bandgap energy as the gain spectra were in Figure 5.8. The spontaneous emission spectra show the blue shift of emission when barrier height and therefore depth of the QW is increased. Aside from the difference in the photon energy of emission, the spectra are very similar. The width of the spectra at a given peak emission are the same. Emission from states other than the n=1 subband is not observed in either sample. As demonstrated in the calculations of section 5.5, the deeper well increases the separation between confined energy states. This reduces the probability of occupation of those states, so strong emission from these states would not be expected. The spectra shown in Figure 5.9 were calibrated in the same way as the spontaneous emission spectra in Chapter 4.

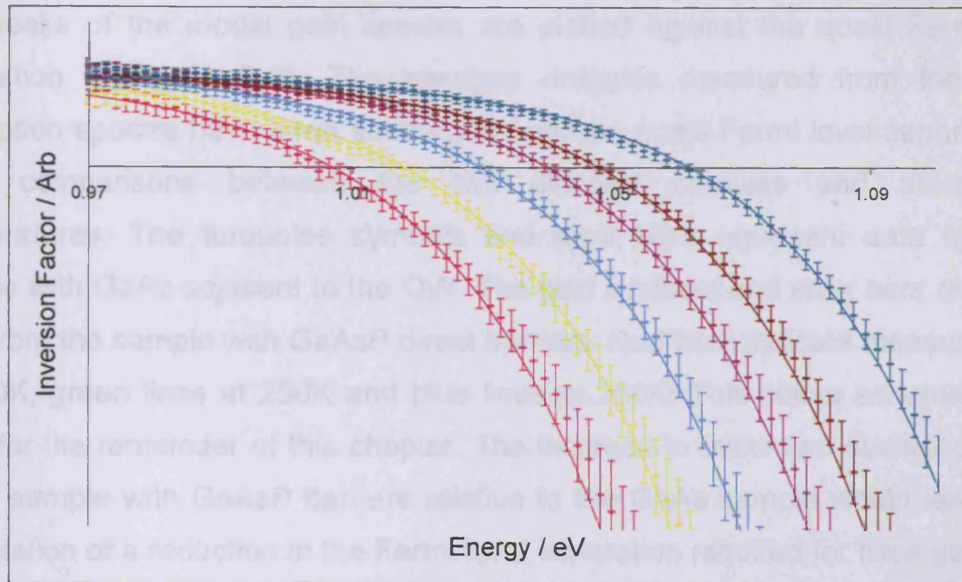

Figure 5.10 Inversion factor for sample with GaAsP adjacent to QW measured at 300K. The symbols and error bars represent the experimental data and the lines are fitted fermi functions.

Figure 5.10 shows the measured P_f (symbols) and corresponding fits (lines) used to determine the calibration constant and hence the true spontaneous emission. The measured Pf spectra at 300K are well described by a thermal distribution.

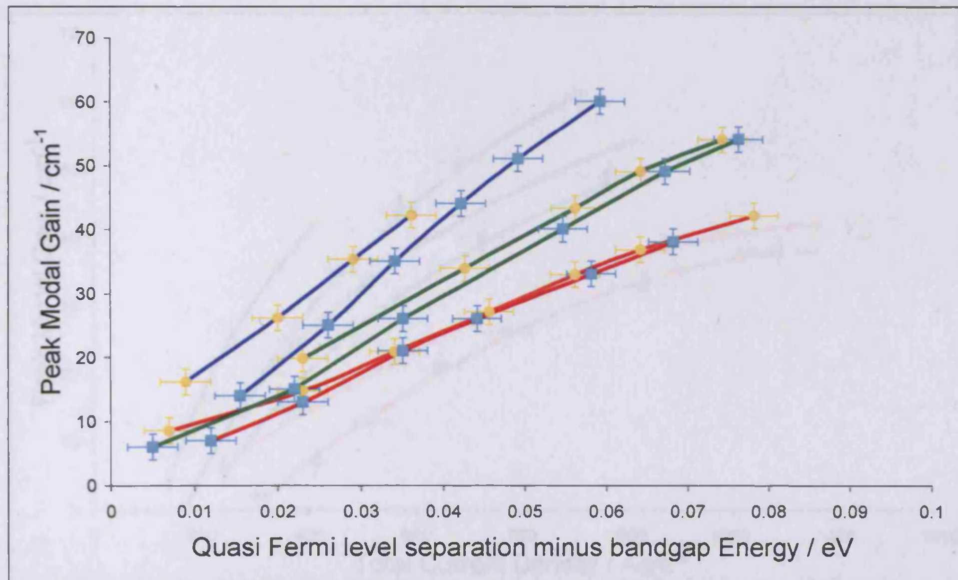

Figure 5.11 Peak modal gain vs. quasi Fermi level separation for samples with GaAs (turquoise symbols) and GaAsP (gold symbols) adjacent to the well. Red lines show data measured at 300K, green at 250K and blue at 200K

The peaks of the modal gain spectra are plotted against the quasi Fermi level separation in Figure 5.11. The bandgap energies measured from the modal absorption spectra have been subtracted form the quasi Fermi level separation to allow comparisons between the two different samples and at different temperatures. The turquoise symbols and error bars represent data from the sample with GaAs adjacent to the QW. The gold symbols and error bars represent data from the sample with GaAsP direct barriers. Red lines indicate measurements at 300K, green lines at 250K and blue lines at 200K. This colour scheme will be used for the remainder of this chapter. The increase in maximum absorption seen in the sample with GaAsP barriers relative to the GaAs sample would lead to an expectation of a reduction in the Fermi level separation required for fixed gain. This effect is observed in the results at 200 and 250K. At 300K, the plots of peak gain vs. quasi Fermi level separation appear to be the same. This seems to be in disagreement with the measured increase in maximum absorption when the GaAs spacer layer is removed. However, the change of a factor 1.28 observed in the maximum absorption falls within the experimental error bars displayed in Figure 5.11.

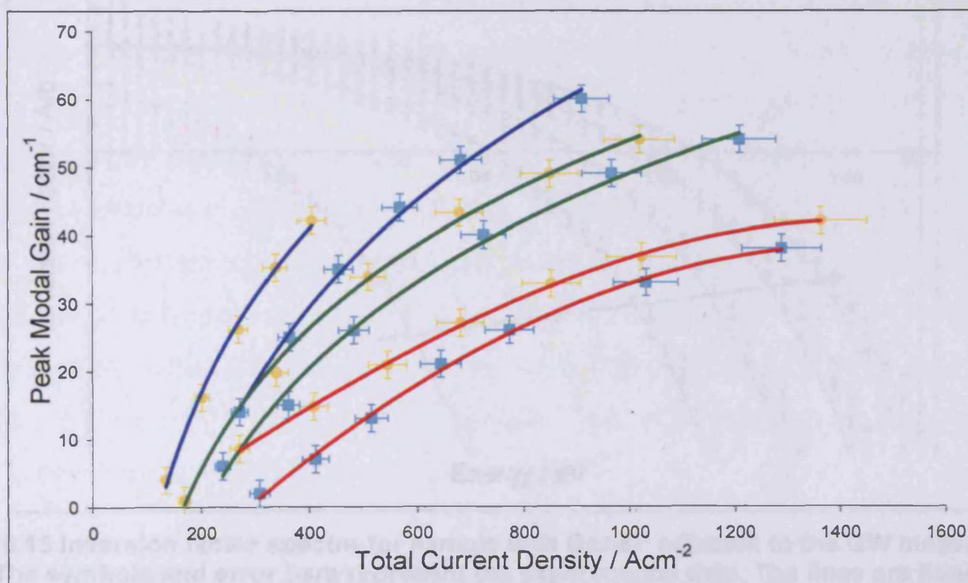

Figure 5.12 Peak modal gain plotted as a function of total current density for samples with a barrier of GaAs (turquoise symbols) and a barrier of GaAsP (gold symbols). Red lines show data measured at 300K, green at 250K and blue at 200K

The peak modal gain values appear plotted against total current density in Figure 5.12. The colour scheme is the same as that used in Figure 5.11. At all temperatures, the total current density needed to achieve a given gain is reduced in the sample with the GaAsP layers directly next to the well relative to the sample with GaAs spacer layers. Whilst this reduction is clearly visible and equal to approximately a factor 1.14 at 300K, it is on the limit of the errors associated with the experiment. As the temperature is reduced the current density required for given gain reduces, with the GaAsP sample appearing to reduce more rapidly. This reduction is up to a factor 3 in the GaAsP structure compared to a factor 2.5 in the GaAs structure. The reduction seen in current density for a fixed gain in the GaAsP sample would enable lasers with lower threshold current densities to be constructed using this structure.

Figure 5.13 shows the inversion factor measured at 200K. The measured data appears as the symbols and error bars. The lines are Fermi functions that have been fitted to the measured data.

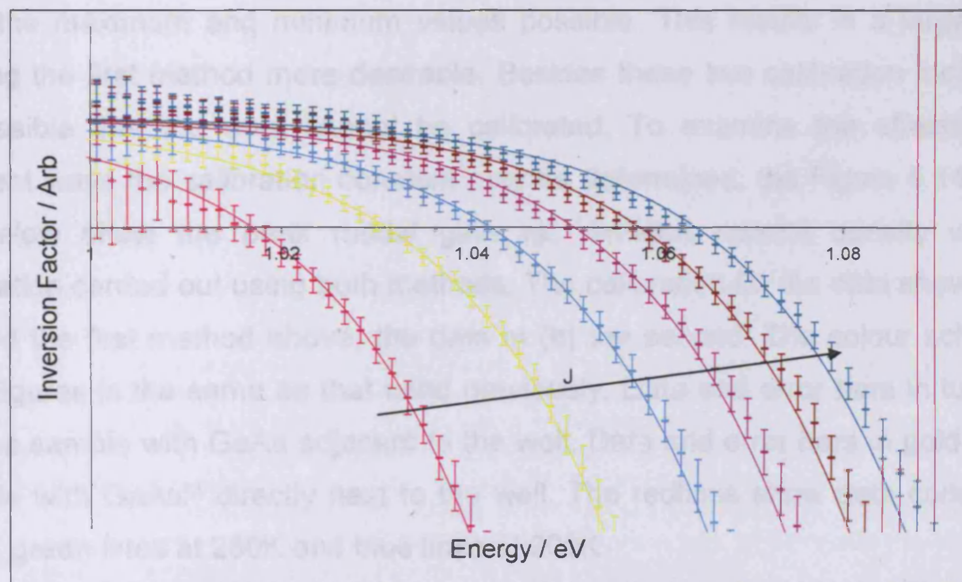

Figure 5.13 Inversion factor spectra for sample with GaAsP adjacent to the QW measured at 200K. The symbols and error bars represent the experimental data. The lines are fitted Fermi functions.

The spectra measured at the lowest three current densities can be described by a thermal distribution of carriers. The calibration constant needed to fit these curves was the same in all three cases. The data measured at higher current densities is not well described by a thermal distribution. The lines shown for this data use the same calibration constant as that used in fitting the low current density data. The procedure used to calibrate the spontaneous emission in this work does not require that the carriers follow a thermal distribution. The requirement is that the inversion factor tends to a constant value. The spectra shown above for higher current densities do tend to a flat value, but this value is not equal to the constant used to fit the low current density plots. These observations give two ways to interpret the calibration constant. The first calibration follows the same method used at 300K and in Chapter 4. Each inversion factor spectrum is fitted with a thermal distribution and any variation in the constant required for fitting provides an estimate of the error involved in the calibration. The second calibration method, which must be applied to the data at high current densities in Figure 5.13, is to choose the value which all the spectra tend towards. For this measurement, the error is estimated from the maximum and minimum values possible. This results in a larger error, making the first method more desirable. Besides these two calibration methods, it is possible that the data cannot be calibrated. To examine the effects of the different ways the calibration constant may be determined, the Figure 5.14(a) and (b) below show the peak modal gain vs. radiative current density with the calibration carried out using both methods. The calibration for the data shown in (a) utilised the first method above, the data in (b) the second. The colour scheme in both figures is the same as that used previously. Data and error bars in turquoise are the sample with GaAs adjacent to the well. Data and error bars in gold are the sample with GaAsP directly next to the well. The redlines show data collected at 300K, green lines at 250K and blue lines at 200K.

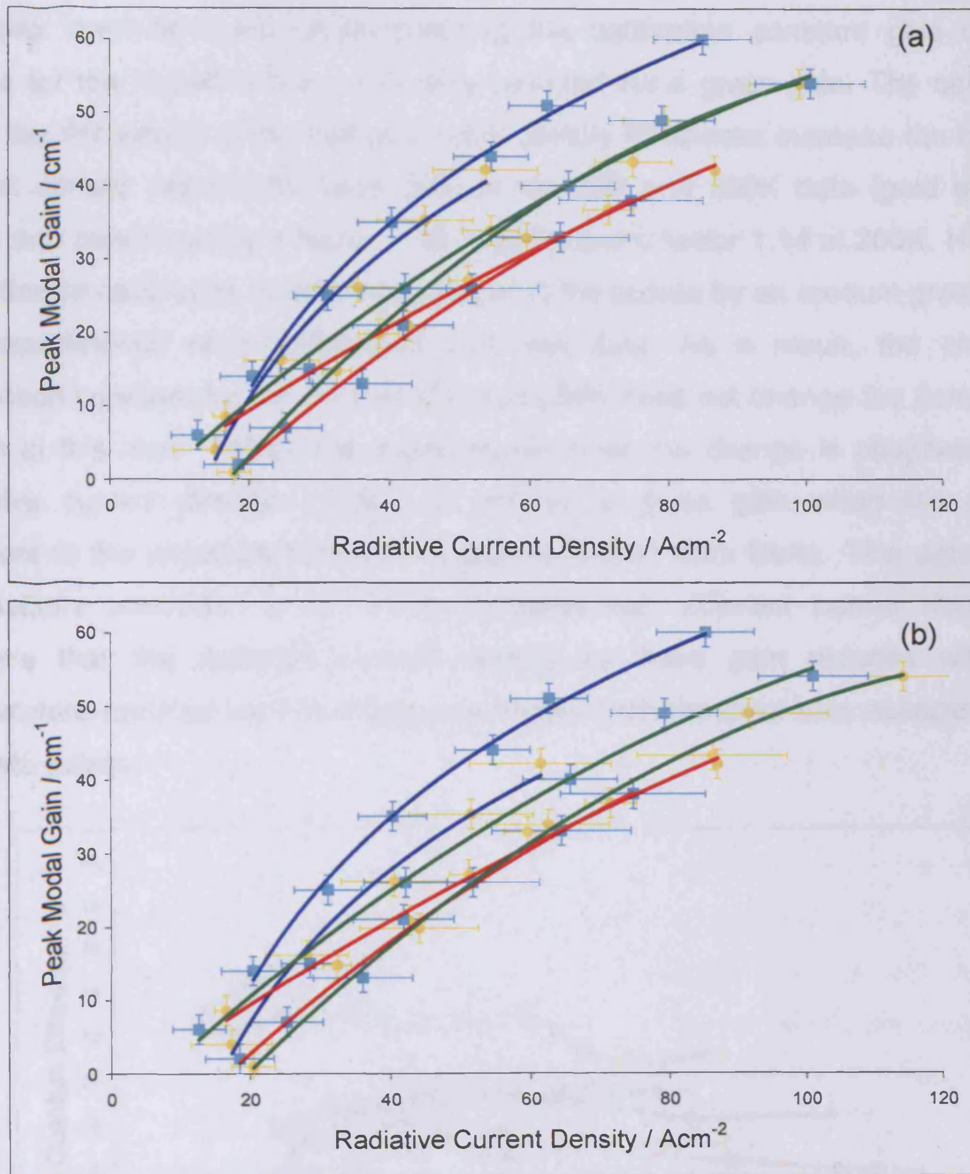

Figure 5.14 Peak modal gain plotted as a function of radiative current density for samples with GaAs (turquoise symbols) and GaAsP (gold symbols) material adjacent to the QW. The lines show the temperature of the measurement, red corresponds to 300K, green to 250K and blue to 200K. In (a) the radiative current densities for data at 200 and 250K were determined from spontaneous emission spectra calibrated by fitting the lower current density data with thermal distribution curves. In (b) they were determined from spontaneous emission spectra calibrated by choosing the calibration constant to be where the high current density inversion factor spectra tended to a constant value.

The two methods used for determining the calibration constant give different results for the radiative current density required for a given gain. The calibration using the flat values of the higher current density Pf spectra increase the radiative current density needed for fixed gain in the 250 and 200K data (gold symbols, green and blue lines) by a factor 1.15 at 250K and a factor 1.14 at 200K. However, the different calibration constants do not shift the curves by an amount greater than the experimental error associated with the data. As a result, the choice of calibration constant for the data at 200 and 250K does not change the conclusions drawn in this work. Within the experimental error, no change is observed in the radiative current density needed to achieve a given gain when the material adjacent to the InGaAsN QW is changed to GaAsP from GaAs. This agrees with calculations presented in [5.13] for samples with different barrier material. It appears that the radiative current density for fixed gain reduces when the temperature reduces but this effect is not larger than the error bars associated with the data points.

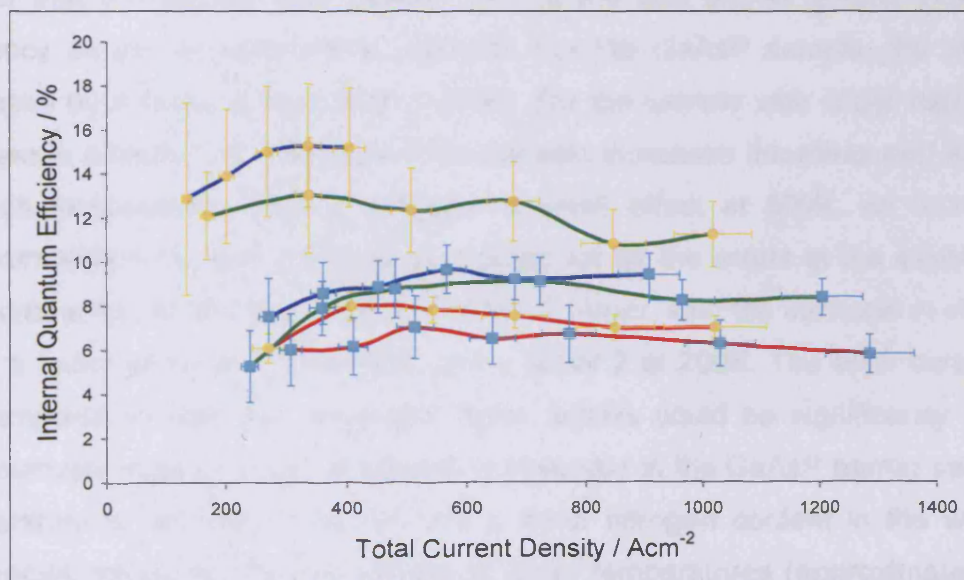

Figure 5.15 Internal quantum efficiency plotted as a function of total current density for samples with barrier material of GaAs (turquoise symbols) and GaAsP (gold symbols). The colour of the lines represents the temperature of the measurements. Red is 300K, green 250K and blue 200K.

Figure 5.15 shows the calculated internal quantum efficiency (radiative current density divided by total current density) plotted as a function of total current density. The data for the sample with GaAsP barriers is calculated from the radiative current densities shown in Figure 5.14(a). As the error bars on this data encompass the points shown in Figure 5.14(b), only one plot of efficiency against total current density is shown here. The colour scheme is the same as that used previously. The trend observed in the comparison between samples of different nitrogen content is observed in the sample with GaAsP direct barriers. As total current density increases, the efficiency increases, reaches a peak and then steadily reduces as the current density increases further. The explanation of this remains the same, at low current density, defect related recombination dominates, then radiative recombination dominates, and finally the curves remain relatively flat with the possibility of a slight decrease as current density increases. For both samples, as the temperature is decreased the internal quantum efficiency increases. Whilst the large error bars make absolute conclusions difficult, it would appear that the sample with GaAsP next to the well shows greater increase in efficiency as the temperature is reduced. For the GaAsP sample, the efficiency increases by a factor 2 from 300 to 200K. For the sample with GaAs barriers this increase is a factor 1.5. The GaAsP barrier also increases the measured efficiency at each temperature. This is however a small effect at 300K, an increase of approximately 1.15, and could be accounted for by the errors in the experimental measurements. At 250 and 200K the effect is larger, with the increase in efficiency being a factor of about 1.5 at 250K and a factor 2 at 200K. The error bars on this low temperature data are large and these factors could be significantly smaller. The relatively large increase in efficiency observed in the GaAsP barrier sample as temperature is reduced could indicate a lower nitrogen content in the well. The efficiencies measured for this sample at lower temperatures (approximately 15%) fall between those for the InGaAs structure studied in chapter 4 (typically 20-23%) and the sample with 5% nitrogen and GaAs barriers (typically 8-9%). The increased efficiency at low temperature supports the theory that the sample with GaAsP barriers contains less nitrogen than the sample with GaAs barriers.

However, the complications in the calibration of the 250 and 200K spontaneous emission rate spectra for the GaAsP barrier sample must be taken into account. Bearing this in mind, it is not possible to draw precise conclusions from this data.

5.7 Occupation of Barrier Layers

Whilst the size of the error bars on the data rule out absolute conclusions, the data suggests an increase in efficiency for the GaAsP sample compared to the GaAs sample at 300K. This means that there is less non radiative recombination or reduced thermal leakage in the sample with GaAsP barriers. To further investigate whether leakage of carriers from the well can explain this increase in efficiency, the number of carriers occupying the barrier layers for the different samples was calculated. These calculations were carried out using the same material parameters as those used for the solutions to Schrödinger's equation.

The number of occupied states per unit area in a single subband for a 2-D semiconductor layer is given by [5.9]:

$$N = \frac{kTm^*}{\pi\hbar^2}\ln\left[1+\exp\left(\frac{(E_F - E_n)}{kT}\right)\right]$$

Equation 5.5

The number of carriers is controlled by the Fermi level, E_f. From the data measured using the segmented contact method, it is possible to determine the Fermi levels within the structure. From Figure 5.11, the quasi Fermi level separation minus bandgap energy is 0.07eV, for a peak gain of approximately 40cm^{-1}. For the structures studied here, both well and barriers are treated as 2-D structures. In addition, only a single subband in the QW is used for calculation. The Fermi levels in conduction and valence bands are calculated by working out the carrier concentrations for the range of Fermi levels possible from the value 0.07eV. The range of values is illustrated in Figure 5.16.To start, the Fermi levels were set so that the conduction band Fermi level, E_{fc}, was 0.07eV higher than the conduction

band confined energy level, E_{nc}. This sets the valence band Fermi level, E_{fv} equal to the valence band confined energy level, E_{nv}. The calculation of n and p was performed for these Fermi levels and repeated with the Fermi levels shifted down in energy in steps of 1meV. This process was repeated until E_{fv} was 0.07eV below E_{nv} shown as 'End' in Figure 5.16 and giving E_{fc} equal to E_{nc}.

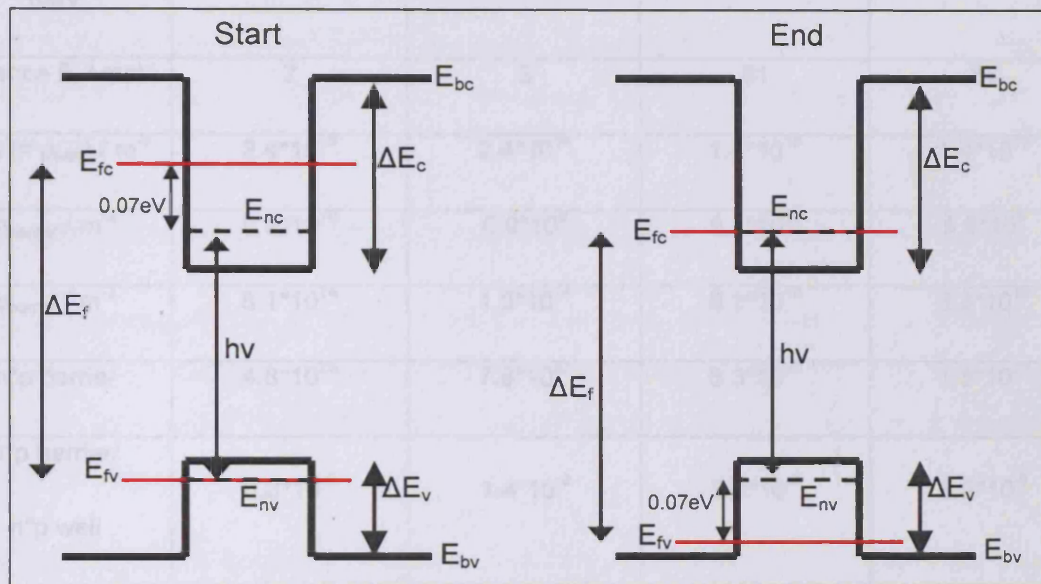

Figure 5.16 Range of Fermi levels used to perform calculation of QW and barrier occupation.

The correct Fermi levels occur when the number of carriers in the conduction and valence bands within the well are equal ($n_{well}=p_{well}$). Assuming the system is in quasi thermal equilibrium, these same Fermi levels are then used to calculate n and p in the barrier layers, using the barrier height as E_n and the barrier effective mass in Equation 5.5. The carrier concentrations calculated for the same cases as in section 5.5.1 at 300K are shown in Table 5.2.

Well	$In_{0.43}Ga_{0.57}As_{0.9938}N_{0.0062}$	$In_{0.43}Ga_{0.57}As_{0.9938}N_{0.0062}$	$In_{0.3}Ga_{0.7}As_{0.99}N_{0.01}$	$In_{0.3}Ga_{0.7}As_{0.99}N_{0.01}$
Barrier	GaAs	$Ga_{0.85}As_{0.15}P$	GaAs	$Ga_{0.8}As_{0.2}P$
Conduction E_f / meV	159	170	120	133
Valence E_f / meV	2	3	81	87
n_{well} (= p_{well}) / m^{-2}	$2.4*10^{16}$	$2.4*10^{16}$	$1.4*10^{16}$	$1.4*10^{16}$
$n_{barrier}$ / m^{-2}	$5.9*10^{10}$	$6.0*10^{9}$	$9.2*10^{10}$	$5.6*10^{9}$
$p_{barrier}$ / m^{-2}	$8.1*10^{14}$	$1.3*10^{14}$	$6.8*10^{15}$	$3.3*10^{15}$
n*p barrier	$4.8*10^{25}$	$7.8*10^{23}$	$6.3*10^{26}$	$1.8*10^{25}$
n*p barrier/ n*p well	$8.3*10^{-8}$	$1.4*10^{-9}$	$3.2*10^{-6}$	$9.2*10^{-8}$
n*p barrier relative to GaAs barrier		1.6%		2.9%
J_{nonrad} barrier / Acm^{-2}	13.0	2.1	108.8	52.8
J_{rad} barrier / Acm^{-2}	$1.5*10^{-5}$	$2.5*10^{-7}$	$2.0*10^{-4}$	$5.8*10^{-6}$

Table 5.2 Calculated occupation of well and barriers for structures described in [5.1,5.4].

The change in barrier material from GaAs to GaAsP brings about a reduction in the number of electrons occupying the barrier of an order of magnitude. The number of holes occupying the barrier is reduced by up to a factor 6.2. The np product in the barrier relative to the well is reduced by greater than an order of magnitude. Also shown in Table 5.2 is the np product within the barriers for the two different barrier

materials. The occupation of the barriers falls to less than 3% of the GaAs value when GaAsP is used. The final two rows show the nonradiative and radiative current densities calculated using a value of 1ns for the nonradiative lifetime and B = $2*10^{-4}$ cm^2s^{-1}. In all cases, the radiative current densities are very small. The nonradiative current densities are relatively high. For the case of 30% Indium, the nonradiative current density in the barrier is of the same order as the radiative current density measured within the well. This suggests that barrier recombination contributes to the low efficiencies measured, but cannot be used to explain them completely.

5.8 Spontaneous Emission collected from the top of samples.

Having calculated the occupation of the barriers, the spontaneous emission rate spectra were measured from the top of the samples to examine whether the large reduction in number of carriers with GaAsP barriers is observable by a reduction in barrier emission.

The spontaneous emission emitted from the top of the structures has travelled through material with a significantly wider bandgap than the QW and waveguide core. Therefore, it will have experienced negligible absorption, allowing the detection of light emitted at photon energies that are heavily absorbed in ASE measurements. This allows observation of any light emitted from the barrier material surrounding the QW. The presence of light at higher photon energies than the main spontaneous emission region would indicate emission of light from the barrier regions. To emit light, these barrier regions must be populated with carriers. If leakage of carriers from the QW to the barriers is not significant, there will be fewer carriers in the barrier region and therefore less light emitted. Conversely, if light is observed, it would confirm the presence of leakage of carriers from the QW to the barrier.

Measurement of emission from the top of the samples was achieved by mounting samples onto TO5 headers in such a way that light from the channel between

sections 1 and 2 could be collected with sections 1 and 2 being driven at the same current density. The same measurement system was used for these experiments as for the multisection measurements. The only differences being the orientation of the sample and the need to collect only one light signal vs. the 2 ASE signals. An extra slit was also used positioned at 90^0 to the monochromator's entrance slit. This was to attempt to block the large amount of light emitted from the facet being reflected into the monochromator by the interior of the cryostat.

The spectra shown in Figure 5.17 were measured at 350K and high current densities. Elevated temperature and high injection should increase the possibility of any thermal leakage effects. Data shown in turquoise are for the sample with GaAs next to the well, data in gold for GaAsP. The energy range of emission for GaAs has been focused on.

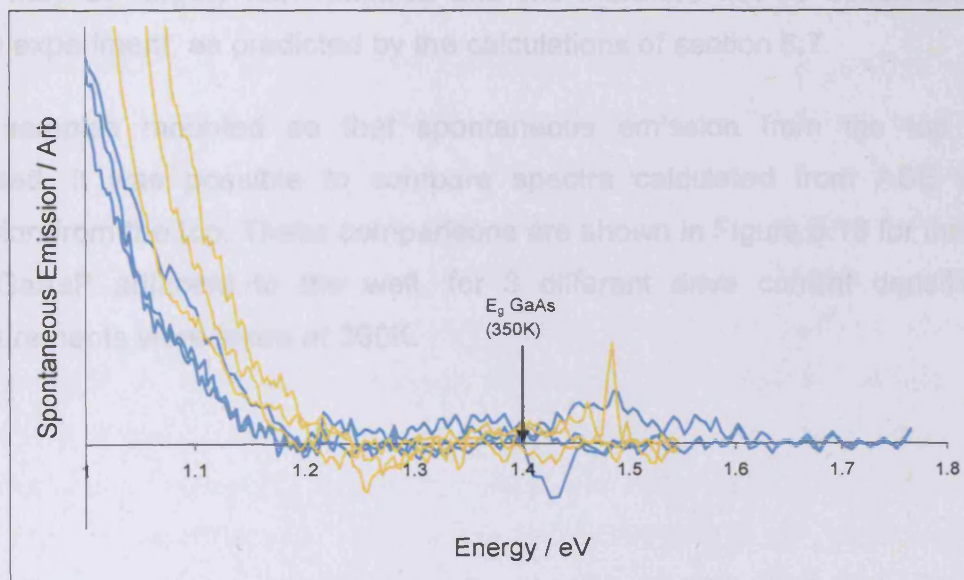

Figure 5.17 Spontaneous emission spectra measured from the channel between sections 1 and 2 of a multisection device. For samples with GaAs barriers (turquoise) and GaAsP barriers (gold) and measured at 350K. The three plots for each device are data measured at 3 different drive current densities.

It is immediately obvious from the curves that the signal levels involved in measurements from the channel between sections are very small compared with ASE data; the noise present on the data above is large. On first inspection there

may be peaks due to emission from the barrier regions. However the noise on the data is very high and these apparent peaks are most likely due to fluctuations in the measurement system. One of the spectra for the GaAs sample appears to show a peak just below 1.5eV but the fluctuations in the measurement system are too great to draw accurate conclusions for the signal levels involved.

Whilst the presence of emission at high photon energies would have confirmed thermal leakage, its absence does not discount it. It is entirely plausible that there is strong leakage of holes from the well, as predicted by calculation of carrier occupations but that other factors prevent light emission. The number of electrons occupying the barriers is small relative to the number of holes, typically by a factor 10^5. Therefore the holes have few electrons to recombine radiatively with. Also, even with electrons and holes leaking to the barriers, any recombination taking place may be largely non radiative and will therefore not be observable in the above experiment, as predicted by the calculations of section 5.7.

With samples mounted so that spontaneous emission from the top can be collected, it was possible to compare spectra calculated from ASE with the emission from the top. These comparisons are shown in Figure 5.18 for the sample with GaAsP adjacent to the well, for 3 different drive current densities. The measurements were taken at 300K.

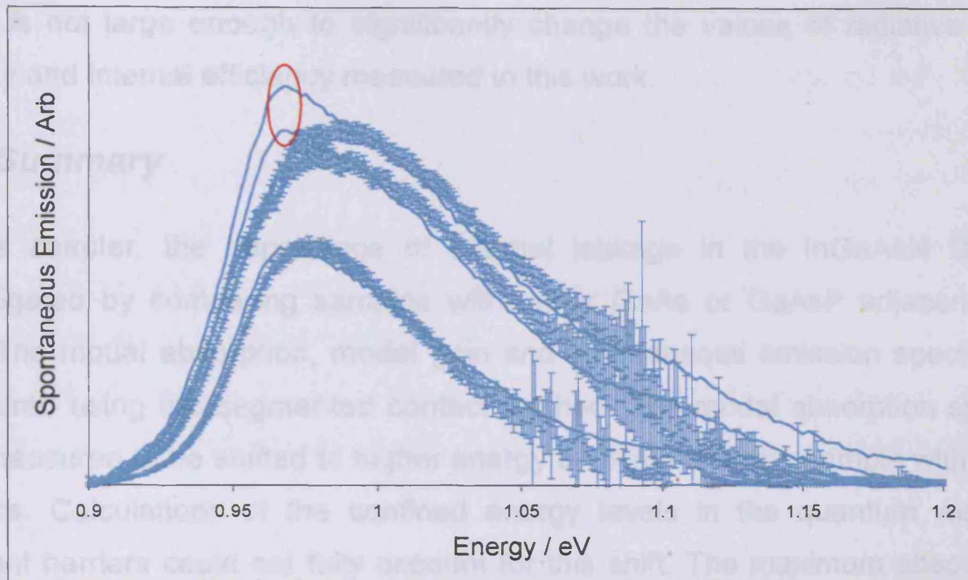

Figure 5.18 Spontaneous emission spectra measured from top of multisection sample (lines) compared to spontaneous emission spectra calculated from ASE spectra. The data are for a sample temperature of 300K.

The lines in Figure 5.18 show data collected from the top, the symbols and error bars data calculated from ASE spectra. The peak present in the two higher current density spectra that is circled in red is due to reflected ASE from the facet being collected in the experiment. Excluding this peak, good agreement is observed between the two techniques, particularly at the lowest current density. The inclusion of a second slit in the measurement system reduced the effect of the reflected light, but could not completely remove it. The agreement between the two techniques at low current density and at other regions of the spectra indicates that the collection of reflected light had a negligible effect apart from this erroneous peak. The largest difference between the two techniques is at high photon energy. This is not a surprise as in this region the error bars on the ASE data become very large. This occurs because the signals used to calculate spontaneous emission are very close to having the same value due to the material being absorbing. As a result of this, a small fluctuation in ASE causes a large effect in the calculated spontaneous emission. In addition, light travelling down the cavity experiences strong absorption and this may reduce the measured spontaneous emission. This

effect is not large enough to significantly change the values of radiative current density and internal efficiency measured in this work.

5.9 Summary

In this chapter, the importance of thermal leakage in the InGaAsN QW was investigated by comparing samples with either GaAs or GaAsP adjacent to the QW. The modal absorption, modal gain and spontaneous emission spectra were measured using the segmented contact method. The modal absorption spectrum was measured to be shifted to higher energy by 24meV for the sample with GaAsP barriers. Calculations of the confined energy levels in the quantum wells with different barriers could not fully account for this shift. The maximum absorption in the sample with GaAsP was found to be higher than that for GaAs. Calculations of the overlap integral showed that this could not be explained by a lower overlap integral in the GaAs sample. These two observations point to the compositions of the two samples being different. The GaAsP sample may have lower nitrogen or indium content than the GaAs sample. The shape of the modal gain and spontaneous emission spectra were very similar for both samples. No decrease in the quasi Fermi level separation needed for a given gain was observed for the sample with GaAsP at 300K. The change expected from the absorption data fell within the error bars. At 250 and 200K the quasi Fermi level separation required for a given gain was observed to reduce in the sample with GaAsP barriers, in agreement with the increased maximum absorption. The total current density needed to achieve a given gain was reduced in the sample with GaAsP. This was true at all temperatures, but the effect was relatively small, approximately a factor 1.14 at 300K. Within the errors of the experiment the gain vs. radiative current density curves for both samples were the same at each temperature and did not change within the error bars as the temperature was decreased. At temperatures of 250 and 200K, a thermal distribution did not describe the carrier distribution accurately at high injection levels, although the effect of this on the calibration of the data was within the error bars calculated in the calibration procedure. The

internal efficiency was found to increase in the sample with GaAsP barriers by a factor 1.15 at 300K and as high as a factor 1.6 as the temperature was reduced. Finally, the presence of light emission from the barriers was investigated by calculating the occupation of the barrier layers and measuring the spontaneous emission from the top of the two samples. The calculations predicted a decrease in barrier occupation when using GaAsP barriers to a value of 3% of the GaAs sample's value. The measurements of spontaneous emission from the top were carried out at 350K and high injection levels. Although no emission from the barriers was observed, the possibility of hole leakage could not be discounted.

5.10 References

5.1 N. Tansu, L. J. Mawst, *J Appl Phys*, **97** (2005) 054502

5.2 M. Galluppi, L. Geelhaar, H. Riechert, *Appl Phys Letts*, **86** (2005) 131925

5.3 M. Hetterich, M. D. Dawson, A. Y. Egorov, D. Bernklau, H. Riechert, *Appl Phys Letts,* **76** (2000) 1030

5.4 H. Carrere, X. Marie, J. Barrau, T. Amand, *Appl Phys Letts,* **86** (2005) 071116

5.5 J. B. Heroux, C. Yang, W. I. Wang, *J Appl Phys*, **92** (2002) 4361

5.6 M. Kondow, T. Kitani, S. Nakatsuka, M. C. Larson, K. Nakahara, Y. Yazawa, M. Okai, *IEEE J. Sel Top Quantum Electron*, **3** (1997) 719

5.7 N. Tansu, J. Y. Yeh, L. J. Mawst, *Appl Phys Letts*, **83** (2003) 2112

5.8 J. Hader, S. W. Koch, J. V. Moloney, *Solid Stat Elec,* **47** (2003) 513-521

5.9 L. A. Coldren, S. W. Corzine, "Diode Lasers and Photonic Integrated Circuits" Wiley, New York (1995)

5.10 R. Eisberg, R. Resnick, "Quantum Physics of Atoms, Molecules, Solids, Nuclei and Particles" Wiley, New York (1985)

5.11 M. S. Wartak, P. Weetman, *J. Appl Phys*, **98** (2005) 113705

5.12 P. Zory, "Quantum Well Lasers" Academic Press, San Diego (1993)

5.13 W. J. Fan, S. T. Hg, S. F. Yoon, M. F. Li, T. C. Chong. *J Appl Phys*, **93** (2003) 5836

Chapter 6 Summary of Achievements and Future Work

6.1 Achievements

The work undertaken in this thesis is split into two sections. In chapter 4 the influence of nitrogen content on the optical properties of InGaAsN QWs is examined. Chapter 5 investigates the possible presence of carrier leakage by comparing InGaAsN QWs with either GaAs or GaAsP barrier material. The achievements of each section are detailed below.

6.1.1 Effect of nitrogen

- The net modal absorption, net modal gain and spontaneous emission rate spectra were measured for structures with 0%, 0.5% and 0.8% nitrogen content in the QW.

- Increasing nitrogen content in the QW shifts the spectra to lower photon energy, reduces the maximum absorption and increases the broadening of the spectra.

- Interpretation of the modal absorption spectra provided information on the effect of nitrogen on the matrix element. Comparing the samples with 0% and 0.5% the observed reduction in absorption of a factor 1.23 can be explained by a decrease in matrix element to a factor 0.63±0.05 of the 0% nitrogen value. The exact value of matrix element reduction depends on the effective mass values used in the analysis.

- The quasi Fermi level separation required for a given peak gain increases with increasing nitrogen content. This is in agreement with the reduction in matrix element found from absorption data.

- The total current density required for a given peak gain was found to be increased by up to a factor 3.9 when the QW nitrogen content was increased form 0% to 0.8%.

- The spontaneous emission rate spectra were calibrated by calculation of the inversion factor. From the spectra in real units, the radiative current densities were calculated. The radiative current density required for a given gain does not change significantly when the QW nitrogen content is increased.

- From the radiative and total current densities the internal quantum efficiency was calculated. Increasing nitrogen content reduces the measured efficiency. For 0% nitrogen the efficiency at 300K was typically 15%, with 0.5% or 0.8% this reduced to approximately 5%.

6.1.2 Effect of barriers

- The net modal absorption, net modal gain and spontaneous emission rate spectra were measured for structures with nominally 0.5% nitrogen in the QW, and either GaAs or GaAsP barrier material.

- The spectra for the sample with GaAsP barriers were shifted to higher photon energy by 24meV relative to the GaAs barrier sample.

- By solving Schrödinger's equation, the shift predicted for the change in barrier height was 12-19meV. The difference between predicted and measured values may be explained by either reduced nitrogen or indium in the GaAsP barrier sample relative to the GaAs barrier sample.

- The maximum modal absorption was increased by a factor 1.28 when the barrier material is changed from GaAs to GaAsP. Calculation of the overlap integral for each structure showed that this increase cannot be explained by an increase in overlap integral.

- The increased maximum absorption may also be explained by a reduced nitrogen or indium content in the GaAsP barrier sample and the increase in matrix element associated with this.

- The total current density required for given peak gain was reduced by a factor 1.14 in the sample with GaAsP barriers relative to the sample with GaAs barriers.

- The spontaneous emission spectra were calibrated and the radiative current densities calculated for both samples.

- The radiative current density required for a given gain was not found to vary significantly when the barrier material is changed from GaAs to GaAsP.

- The measured internal efficiency increased by a factor 1.15 in the GaAsP barrier sample relative to the GaAs barrier sample at 300K.

- The expected occupation of the barriers was calculated for an InGaAsN QW with GaAs or GaAsP barriers. With GaAsP barriers the n.p product in the barriers decreased to less than 3% of its value with GaAs barriers.

- To test the presence of radiative recombination in the barriers, spontaneous emission rate spectra were measured from the top of the samples. No emission was observable but low signal levels may have prevented any emission present from being detected.

6.2 Conclusion

The work presented in this thesis represents the first experimental evidence for the reduction in matrix element with increasing nitrogen content predicted by theory. In addition to this, it is also the first measurement of the overall internal efficiency in InGaAsN QW laser structures. Measurements of the differential efficiency above threshold have been made previously but these two efficiencies are quite different. The overall internal efficiency measures the percentage of carriers injected to a

laser structure that recombine radiatively. The differential efficiency only applies to above threshold conditions in a laser and is the percentage of additional carriers above threshold that contribute to the laser light output.

The overall efficiencies measured in this work are relatively low: less than 20% for InGaAs and falling to approximately 5% for 0.8% nitrogen at 300K. The large reduction in efficiency as nitrogen content increases means that there is still plenty of room to improve on the current InGaAsN devices. From the data presented here and elsewhere, it is likely that the reduction in efficiency with increasing nitrogen content is caused by increased non radiative recombination due to defects in the crystal. This leaves two possibilities for the future of dilute nitride QW lasers. If the defects are directly associated with the nitrogen, increased nitrogen cannot be achieved without increasing defects and the nitrogen content must be minimised. Alternatively the defects may be associated with the growth processes for InGaAsN QW structures. In this case, there is potential to improve the efficiency of dilute nitride structures by improvements in the growth processes used to grow the wafers. If the conditions can be optimised for growth of InGaAsN layers, then the dilute nitride material system is very promising for providing lasers emitting at 1.3μm and grown on GaAs substrates.

6.3 Future Work

Having completed the work presented in this thesis, there are several experiments which would add to the insight into InGaAsN gained here.

For all samples, measurements at higher temperatures would be useful. This data may provide further insight into the recombination mechanisms in InGaAsN. These measurements were not possible during this project due to the higher temperature shifting the emission to lower photon energy, outside the working range of the PMT used as a detector.

For the samples with different barriers, increasing the likelihood of thermal leakage would be useful. This would increase the effect of leakage in the structures and

should make its effects more pronounced and measurable. This could be achieved by measuring at higher temperatures. However, it would also be interesting to examine samples with higher nitrogen content in the QW and either GaAs or GaAsP barriers. The higher nitrogen content should reduce the valance band barrier height, causing the effects of leakage to be increased.

Publications and presentations

"The Effect of nitrogen in InGaAsN Quantum Well Lasers"

D. J. Palmer, P. M. Smowton, P. Blood, J-Y Yeh, L. J. Mawst, N. Tansu.

QEP-16, Glasgow, 2004.

"Effect of nitrogen on gain and efficiency in InGaAsN quantum-well lasers"

D. J. Palmer, P. M. Smowton, P. Blood, J-Y Yeh, L. J. Mawst, N. Tansu,

Appl Phys Letts. **86** (2005) 071121.

"The effect of temperature on the gain and efficiency of InGaAs and InGaAsN quantum well laser structures"

D. J. Palmer, P. M. Smowton, P. Blood, SIOE, Cardiff, 2005.

"The Effect of Temperature on the Efficiency of InGaAs and InGaAsN Quantum Well Laser Structures"

D. J. Palmer, P. M. Smowton, P. Blood, J-Y Yeh, L. J. Mawst, N. Tansu,

CLEO, Baltimore, 2005.